Integrating Analytical and Remote Sensing Techniques to Investigate the

Petrology of Planetary Surfaces

by

Christopher W. Haberle

A Dissertation Presented in Partial Fulfillment
of the Requirements for the Degree
Doctor of Philosophy

Approved April 2018 by the
Graduate Supervisory Committee:

Philip Christensen, Chair
Laurence Garvie
James Bell
Steven Ruff
Richard Hervig

ARIZONA STATE UNIVERSITY

May 2018

ABSTRACT

Interpreting the petrogenesis of materials exposed on the surface of planets and asteroids is fundamental to understanding the origins and evolution of the inner Solar System. Temperature, pressure, fO_2, and bulk composition directly influence the petrogenetic history of planetary surfaces and constraining these variables with remote sensing techniques is challenging. The integration of remote sensing data with analytical investigations of natural samples, lab-based spectroscopy, and thermodynamic modelling improves our ability to interpret the petrogenesis of planetary materials.

A suite of naturally heated carbonaceous chondrite material was studied with lab-based spectroscopic techniques, including visible near-infrared and Fourier transform infrared reflectance spectroscopy. Distinct mineralogic, and thus spectroscopic, trends are observed with increasing degree of thermal metamorphism. Characterization of these spectral trends yields a set of mappable parameters that will be applied to remotely sensed data from the OSIRIS-REx science payload. Information about the thermal history of the surface of the asteroid Bennu will aid in the selection of a sampling site, ensuring OSIRIS-REx collects a pristine regolith sample that has not experienced devolatilization of primitive organics or dehydration of phyllosilicates.

The evolution of mafic magma results in distinct major element chemical trends. Mineral assemblages present in evolved volcanic rocks are indicators of these processes. Using laboratory spectroscopic analyses of a suite of evolved volcanic rocks from the Snake River Plain, Idaho, I show that these evolutionary trends are reflected in the spectral signatures of ferromagenesian and feldspar minerals.

The Athena science package on the Mars Exploration Rover Spirit allows for the *in situ* investigation of bulk chemistry, texture, and mineralogy on the surface of Mars. Using the bulk composition of the Irvine and Backstay volcanic rocks, thermodynamic

i

modeling was performed to further constrain the formation conditions of Martian volcanics. Irvine and Backstay compositions exhibit dramatic variations in modal mineralogy with changing fO_2. Using these results, I show that the observed Mini-TES spectra of Irvine and Backstay can be adequately reproduced, and additional constraints can be placed on their primary fO_2.

DEDICATION

This dissertation is dedicated to Bob. You can retire now.

ACKNOWLEDGMENTS

TABLE OF CONTENTS

Page

LIST OF TABLES

LIST OF FIGURES

Figure	Page

CHAPTER 1

Introduction

The work presented within this dissertation is motivated by the desire to refine our ability to interpret the events that produce the materials exposed on the surfaces of small bodies and planets. Often the geologic events that modify planetary surfaces result in suites of materials that are petrologically related to one another. Detailed laboratory analysis of these related sample suites yields important information on the formation conditions of these rocks. Fluctuations of environmental variables (e.g. temperature, pressure, oxygen fugacity, and the presence and abundance of water) during petrogenesis can lead to different end products that, when paired with their starting materials, can be used to infer the conditions of their formation. On Earth, access to both samples and analytical instruments is straightforward. Similar sample-based investigations of the surfaces of Mars, the Moon, and asteroids are more challenging and rely on spacecraft remote sensing observations, the study of meteorites, landed in situ missions, and sample return missions, each of which have strengths and weaknesses. Remote sensing investigations are expansive and informative with the ability to characterize large portions of a planetary surface in a relatively short period of time; however, these investigations will always lack the detail and precision of sample-based laboratory investigations. Meteorites provide a sample-in-hand and enable us to collect a full battery of analytical measurements but these samples lack geologic context, have experienced degradation or weathering, and it is doubtful that our collections are representative of the objects they come from. Landed in situ missions offer the ability to thoroughly characterize outcrop-scale portions of the surface using remote sensing and miniaturized analytical instruments but are limited in their ability to cover extensive portions of the surface, prepare samples for

analysis, and access hard to reach samples. Sample return missions provide a means to collect samples from a planetary surface and deliver them to terrestrial laboratories while concurrently obtaining the contextual information necessary to gain an understanding about their formation history. Unfortunately, sample return missions still only retrieve samples from small portions of the surface and are prohibitively expensive, complicated and risky. The investigations presented herein apply an integrated approach to the study of planetary surfaces, combining techniques employed by planetary materials scientists and the planetary remote sensing community to investigate meteorites, terrestrial analog volcanic materials, and Mars.

The subject of chapters 2 and 3 is the Sutter's Mill carbonaceous chondrite. This carbonaceous chondrite was observed falling on April 22nd, 2012 in the northern Sierra Nevada foothills. Samples from Sutter's Mill show a chemical affinity to the CM group and contain solar implanted Ne, indicating that Sutter's Mill is a regolith breccia from the surface of carbonaceous asteroid. Preliminary mineralogical investigations showed that Sutter's Mill contained at least two distinct lithologies, phyllosilicate-bearing and olivine-rich. Chapter 2 focuses on sample SM3, which was collected before rain fell over the recovery area and represents one of the least contaminated samples in the collection. Using electron microprobe analysis (EMPA), powder x-ray diffraction (XRD) analysis, thermogravimetric analysis (TGA), and Raman spectroscopy, comparisons are made between SM3, an olivine-rich stone, and SM41, a phyllosilicate-bearing stone. SM3 was found to have experienced temperatures as high as $750°$ C leading to the dehydroxylation and thermal transformation of phyllosilicate minerals to form olivine. In addition, grains of oldhamite (CaS) were observed throughout SM3 and their presence is attributed to the in situ thermal decomposition of calcite in a reducing and S rich environment as opposed to physical mixing with an enstatite chondrite.

Building on the results of chapter 2, chapter 3 examines powdered samples from 11 Sutter's Mill and 5 CM2 meteorites using visible to near-infrared reflectance spectroscopy (VNIR) to investigate the spectral signature of dehydration in carbonaceous regolith. SM3, SM41 and Murchison are examined in greater detail using XRD, TGA, and Fourier transform infrared (FTIR) spectroscopy. FTIR analysis allows for the observation of an extended spectral range (0.35-4.5 μm) including the region most sensitive to water bound in phyllosilicates and overlaps with the measurements that the OSIRIS-REx spacecraft will be able to make. Compared to the spectrum of a typical CM2 chondrite, Sutter's Mill stones are darker, flatter and exhibit weakened absorptions in the UV, 1 μm and 3 μm regions. These results are similar to those observed experimentally by previous researchers and reveal a systematic change, with increasing thermal metamorphism, from a typical CM2 spectrum to a nearly flat and featureless spectrum (SM3). Here I show how determinations of spectral sinuosity, 0.7 μm band depth, and 3 μm integrated band intensities can identify potentially dehydrated carbonaceous regolith. These results will be applied to OVIRS and MapCam observations when the OSIRIS-REx spacecraft arrives at Bennu. If similar spectral signatures are detected on the surface they can be mapped and avoided in order to collect a more pristine sample which has not lost its primitive organics and hydrated minerals.

The work presented in chapter 4 shifts focus to igneous processes on Earth as an analog to Mars and, coincidentally, the Moon. On Earth, greater than 90% of volcanic activity occurs at or near the convergent and divergent margins marking the boundaries of the lithospheric plates. As such, the processes that generate melt at these regions and the melts themselves are unique to Earth. In order to find a more appropriate analog for the volcanic products generated on Mars, this investigation

focuses on Earth's intra-plate volcanic centers. One such intra-plate volcanic center is the continental tholeiitic suite of the Snake River Plain (SRP) located in Southern Idaho. This region is host to a diverse suite of volcanic lava flows whose bulk chemical composition varies due to differences in melt ascent paths and crustal residence times. Using combined VNIR and thermal infrared (TIR) spectral observations of the SRP sample suite, major element evolutionary trends typical of intra-plate basaltic volcanism can be identified. These trends are expressed as variations in major phase composition (e.g. feldspar and olivine) as well as the presence of abundant strongly absorbing opaque minerals due to Fe-enrichment both of which are uniquely identifiable using these spectroscopic techniques. Searching for these spectral trends on the surface of Mars can yield valuable insight to magmatic processes occurring within and on the surface of the planet.

Finally, chapter 5 re-examines the chemical and spectral character of alkaline volcanic rocks observed by the Spirit rover in Gusev Crater. During its ascent of Husband Hill, Spirit encountered several unique classes of rock based upon their signature in miniature thermal emission spectrometer (Mini-TES) data. Upon further investigation with the full suite of contact instruments, these rocks were determined to be alkaline volcanics. This observation of alkaline volcanic rocks on Mars was the first of its kind and indicates a wider diversity of volcanic evolutionary modes than previously thought. At this point in the mission, robust determinations of mineralogy using Mini-TES were hindered by an aeolian event that deposited dust on the Mini-TES pointing and fold mirrors. A robust correction for this thin deposit of dust has since been developed enabling reanalysis of this extensive dataset. The intent of this study is to determine the mineralogy of these alkaline volcanic rocks directly from mirror-dust corrected Mini-TES observations. Additionally, using APXS derived bulk chemistry and the MELTS thermodynamic modeling software, variations in modal mineralogy

with change oxidation state are determined. From these mineralogy determinations synthetic thermal emission spectra are generated for comparison to the Mini-TES observations. This method provides a significant improvement of spectra generated using normative calculations. Moreover, this technique can help constrain the primary fO_2 of volcanic rocks based upon their modal mineralogy.

The combined works presented in this dissertation use modern geochemical and remote sensing analytical techniques together with thermodynamic modelling to aid the interpretation of spectral signatures of natural samples. The ultimate goal of this work is to apply the results of each investigation to the interpretation of the petrology of planetary surfaces. The analysis detailed in chapter 5 is a starting point for achieving this goal, where the use of thermodynamic modelling combined with thermal emission spectroscopy has helped to refine our understanding of samples on the surface of Mars. The outcomes from chapter 4 are intriguing and present a set of spectral signatures that can be mapped on the surface of Mars to potentially make inferences about the regional scale petrological history of the materials exposed on the surface. Similarly, the investigations highlighted in chapters 2 and 3 have focused on samples in a laboratory setting and the results of those studies will be applied to spacecraft data acquired when the OSIRIS-REx spacecraft arrives at Bennu to begin its mapping campaign.

CHAPTER 2
Extraterrestrial Formation of Oldhamite and Portlandite Through Thermal Metamorphism of Calcite in the Sutter's Mill Carbonaceous Chondrite

Haberle, C. W., & Garvie, L. A. (2017). Extraterrestrial formation of oldhamite and portlandite through thermal metamorphism of calcite in the Sutter's Mill carbonaceous chondrite. *American Mineralogist*, *102*(12), 2415-2421.

The CM and CI carbonaceous chondrites are typically dominated by phyllosilicates with variable proportions of tochilinite, anhydrous silicates, carbonates, sulfides, sulfates, oxides and organic compounds. During thermal metamorphism the phyllosilicates dehydrate and decompose yielding water and olivine/enstatite. The thermal transformation of carbonate is less well understood, especially in the presence of volatile decomposition products, such as CO, CO_2, SO_2, H_2S, and H_2O. Here is described the mineralogical transformation of calcite ($CaCO_3$) to oldhamite (CaS) and portlandite ($Ca(OH)_2$) during extraterrestrial thermal metamorphism on the Sutter's Mill parent body. Sutter's Mill is a regolith breccia consisting of at least two lithologic components: phyllosilicate-calcite-bearing and anhydrous olivine-rich. Evidence suggests that the anhydrous stones were derived from extraterrestrial heating of the phyllosilicate-calcite-bearing material. One of only three Sutter's Mill stones (SM3) collected prior to heavy rainfall over the recovery site is the focus of this study. Its powder X-ray diffraction patterns are dominated by olivine, with lesser enstatite, Fe-sulfides, magnetite, and oldhamite. Oldhamite is absent in the rained-on stones reflecting its water sensitivity and the pristine nature of SM3. Optical micrographs show whitish to bluish grains of oldhamite and portlandite embedded in dark, fine-grained matrix. The presence of abundant olivine and absence of phyllosilicates, tochilinite, and carbonate indicates that SM3 underwent heating to ~ 750 °C. At this

temperature, calcite would have decomposed to lime (CaO). Volatilization experiments show that CO, CO_2, SO_2, and H_2S evolve from CM and CI chondrites heated above 600 °C. Lime that formed through calcite decomposition would have reacted with these gases forming oldhamite under reducing conditions. Residual lime not converted to oldhamite, would have readily hydrated to portlandite, possibly through retrograde reactions during cooling on the parent body. These reactions have parallels to those in coal-fired electricity generating plants and provide an analogous system to draw comparison. Furthermore, the identification of these minerals, which are sensitive to terrestrial alteration, and determination of their formation is enabled only by the rapid collection of samples from an observed fall and their subsequent curation.

Introduction

Carbonaceous chondrites represent primitive Solar System materials with chemical similarities to that of the solar photosphere (Anders and Grevesse 1989). Many of the CM and CI carbonaceous chondrites are water-rich and contain a suite of organic compounds making them central to the study of the origins of life. Investigations of the aqueous and thermal evolution of these primitive objects is important to understanding their role in planetary formation and the distribution and composition of volatile species and organic material in the Solar System.

Aqueous alteration of early Solar System materials modifies their mineralogy and petrology through hydration of anhydrous silicates forming phyllosilicates, alteration of Fe-Ni metal, and precipitation of carbonates and sulfates (McSween 1979; Tomeoka and Buseck 1985; Browning et al. 1996; Rubin et al. 2007). Additionally, aqueously altered carbonaceous chondrites can experience thermal metamorphism, acting to dehydrate, decompose, and reduce minerals and organic compounds (Gibson et al. 1972, 1974a, 1974b; Tomeoka et al. 1989a; Nozaki et al. 2006; Court and Sephton 2014; Tonui et al. 2014; Pizzarello and Garvie 2014; Court and Tan 2016).

The energy driving this metamorphism can be generated by a range of processes including decay of short-lived radioisotopes, transient impact-generated thermal pulses, or orbital conditions that draw the parent body close to the Sun.

Thermal metamorphism of the CM and CI carbonaceous chondrites leads to dehydration of phyllosilicates, pyrolysis of organic compounds, and decomposition of tochilinite, carbonates, and sulfates. This heating releases a variety of gases, such as SO_2, H_2S, H_2, H_2O, COS, CS_2, CO_2, CO, and CH_4, which can react with the residual phases (Gibson et al. 1972, 1974a, 1974b; Burgess et al. 1991; Court and Sephton 2014; Court and Tan 2016). Knowledge of these decomposition products and residual phases is important for understanding the processes that alter primitive bodies and is relevant to in situ resource utilization, given the recent interest in asteroidal materials as sources of raw materials (e.g., Lewis et al. 1993; Elvis 2013; Rabade et al. 2016). Several CM carbonaceous chondrites show mineralogies and textures indicative of a thermally metamorphosed phyllosilicate-rich precursor, such as Belgica 7904, Yamato 86720, Dhofar 225, and Dhofar 735 (Tomeoka et al. 1989a; Tomeoka 1990; Ivanova et al. 2010). Only two CI carbonaceous chondrites, Yamato 86029 and Yamato 82162, show mineralogical evidence for post-hydration thermal metamorphism (Tomeoka et al. 1989b; Tonui et al. 2003). These heated meteorites are natural laboratories providing insight into the products and mechanisms of thermal metamorphism on the CM and CI carbonaceous chondrite parent bodies. All previous examples of thermally metamorphosed CM and CI carbonaceous chondrites are finds, and hence have experienced terrestrial weathering. However, Sutter's Mill is a recent fall; this meteorite is mineralogically and isotopically similar to the CM chondrites (Jenniskens et al. 2012), but many of the stones appear to have been extraterrestrially heated following hydration (Garvie 2013). Thus, study of this meteorite provides insight into

9

extraterrestrial thermal metamorphism of CM carbonaceous chondrites sans terrestrial weathering.

Sutter's Mill fell on April 22nd, 2012 over the northern Sierra Nevada foothills (Fries et al. 2014). Approximately 90 stones were recovered, with a cumulative mass of ~1 kg (Jenniskens et al. 2012). Each stone is given an alphanumeric tag beginning with SM (Sutter's Mill) followed by an incremental number. The first three stones (SM1-SM3) were collected on April 24th, 2012, before heavy rain fell across the recovery area. This investigation focuses on pre-rain stone SM3, with comparisons to SM2 (pre-rain) and SM41.

Sutter's Mill is a regolith breccia classified as a carbonaceous chondrite with no additional petrologic type or group association (Jenniskens et al. 2012; Garvie 2013; Zolensky et al. 2014). The $\delta^{18}O$ isotopes partially overlap the CM2 field and the ^{54}Cr excesses overlap that of Murchison (CM2) suggesting a CM-like composition (Ziegler and Garvie 2013; Yamakawa and Yin 2014). Bulk mineralogical observations of seven stones (SM3, 6, 8, 38, 41, 49, and 65) revealed two lithologic components: anhydrous olivine-rich and phyllosilicate-calcite-bearing (Garvie 2013). The phyllosilicate-calcite-bearing stones show broad X-ray reflections indicative of smectite-group minerals, whereas reflections for serpentine are of variable intensity and weak. These clay characteristics differ from the typical serpentine-dominated CM2 meteorites. The mineralogy of the olivine-rich SM stones is similar to that of Belgica 7904 that was heated extraterrestrially to >500 °C (Stage III and IV in Nakamura 2005). Sutter's Mill adds to an increasing number of CM and CI carbonaceous chondrites found to have experienced a range of thermal metamorphic conditions on their parent bodies (Tomeoka, 1990; Nakamura 2005; Ivanova et al. 2010; Tonui et al. 2014).

Sutter's Mill is the only carbonaceous chondrite known to host oldhamite (CaS) (Jenniskens et al 2012; Garvie 2013; Zolensky et al. 2014), a mineral typical of the

enstatite chondrites and aubrites (Rubin 1997). Under reducing conditions oldhamite is predicted to condense from a nebular gas, consistent with its presence in enstatite chondrites (Larimer and Bartholomay 1979, Grossman et al. 2008). It has also been proposed to form from Fe-poor chondrule melts with moderate S concentrations (Piani et al. 2016). Therefore, its occurrence in the more oxidized Fe-rich carbonaceous chondrites is unexpected. Two previous studies have identified oldhamite within SM2 and SM3 (Garvie 2013; Zolensky et al. 2014), with Zolensky et al. (2014) suggesting its presence due to physical mixing with an E-type asteroid on the Sutter's Mill parent body. Physical mixtures of chondritic material are not an undocumented occurrence and there are well-characterized examples e.g., Kaidun and Almahata Sitta (Zolensky and Ivanov 2003; Zolensky et al. 2010). Here we propose a reaction sequence for the *in situ* formation of oldhamite and portlandite from calcite during thermal metamorphism. Meteoritic portlandite has only been previously described as a terrestrial weathering product of oldhamite within the Norton County enstatite achondrite (Okada et al. 1981). We report on the first identification of indigenous meteoritic portlandite.

Materials and Analytical Methods

This investigation focuses on SM3, with comparative observations from SM41 and a fragment of SM2. SM3 is a 5.0 g fusion crusted stone found April 24th, 2012, before heavy rain fell over the fall site. Extensive measures were taken to minimize atmospheric and preparation contamination of the samples. The stone was split with a rock splitter and a ~3- x 5-mm chip was prepared and polished without the use of water. All SM3 pieces have been stored under a nitrogen atmosphere and removed only for analysis. SM2 is a pre-rain stone found April 24th, 2012. This stone was crushed by a car tire in a parking lot: here is studied a 30-mg fragment from the total ~4 g recovered. SM41 is a 9.3 g stone found May 4th, 2012.

The samples were analyzed at the University of Arizona's Michael J. Drake Electron Microprobe lab with a CAMECA SX100 electron microprobe with five Wavelength Dispersive Spectrometers (WDS), and a Princeton Gamma-tech 5000 Energy Dispersive Spectrometer (EDS). Backscattered electron (BSE) imaging, EDS, and WDS analyses were used to determine the elemental compositions of the samples. WDS element maps were acquired for Ca, Fe, Mg, P, Si, Al, Cl, Ni, Na, and S.

Powder X-ray diffraction (XRD) patterns were acquired with a Rigaku MiniFlex 600 diffractometer, with a post-diffraction monochromator, employing Cu Kα radiation. Data were acquired from 2 to 65° at 0.02° steps, and 60 s/step. XRD samples were prepared from ~10 mg chips (~2 mm piece). The chips were crushed and mixed with a few mL of dry methanol. The resulting slurry was pipetted and spread into a thin, smooth film on a low-background single-crystal quartz plate. This slurry was dried rapidly (~ 5 s) under flowing warm air forming a thin film. Selected samples were also prepared as a dry powder deposited directly onto the quartz plate: no differences were seen between patterns from the two preparation methods showing that the methanol did not affect the water-sensitive minerals.

Thermogravimetric (TG) data was acquired under flowing He from 20° to 1000° C, with a heating rate of 10°C/min. Sample sizes were ~40 mg. Data were acquired from three separate chips of SM3, and for comparison from SM41, Murchison (CM2), and Orgueil (CI1).
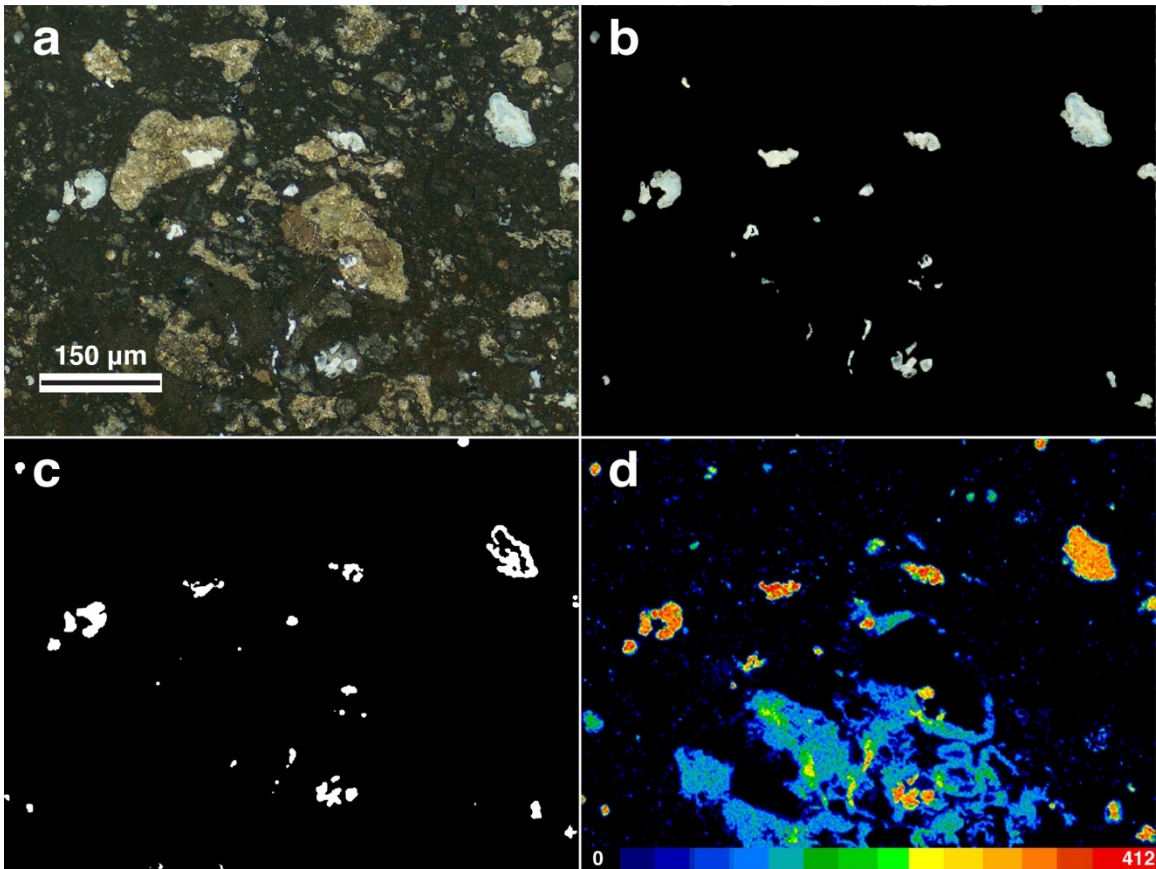
Figure 2.1. Representative section of the SM3 polished mount showing the textural and chemical relationship of clasts set in matrix. (**a**) Optical micrograph showing rounded tan-colored olivine, brown Fe sulfide and whitish-blue grains in dark fine-grained matrix. (**b**) Modified optical image showing the distribution of the whitish-blue grains of oldhamite and portlandite with all other materials cropped. (**c**) Black and white map showing where these grains contain only Ca and S. Pixels where Ca and S are both present above background values are set to 255 and appear white. Pixels where other measured elements are present above background are set to a value of 0, appearing black. This panel highlights the relationship of oldhamite with portlandite. (**d**) Ca element distribution map showing WDS counts per pixel. Note the correlation with grains in (**b**) and (**c**). Observe that the ~75μm whitish-blue grain in the upper right corner of the panel has an even distribution of Ca in (**d**) but has an exterior rim of Ca and S in (**c**), as described in text. Each panel in this figure covers the same area of the mount and the scale in (**a**) applies to all.
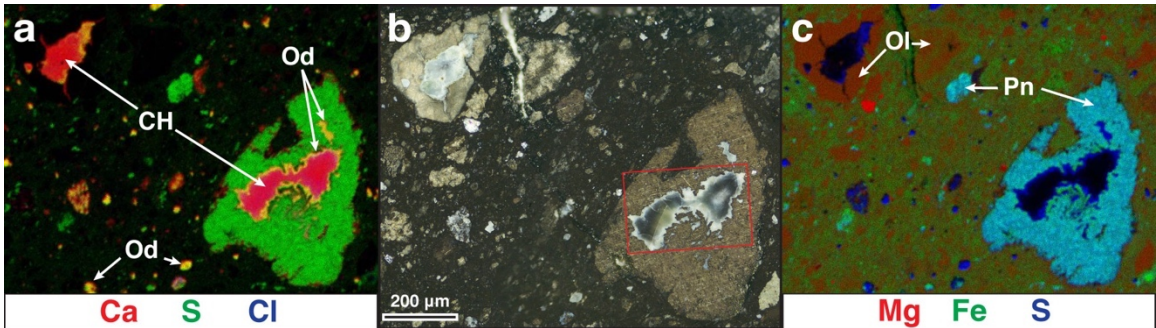
Figure 2.2. (**a** and **c**) False-color composite WDS x-ray element images highlighting petrographic relationships of (**a**) oldhamite (Od) and portlandite (CH) and (**c**) rimming olivine (Ol) and pentlandite (Pn). (**b**) Visible light image showing encased grains of portlandite with oldhamite exteriors. Red box indicates the area mapped in *figure 4* **c** and **d**.

Raman point spectra were acquired over low- (130-2500 cm^{-1}) and high-wavenumber (3400-3800 cm^{-1}) spectral ranges, with exposure times of 1 and 10 s, respectively. A laser power of 3 mW and λ=532 nm excitation was employed in both spectral regions. Micro-Raman mapping was conducted using a HORIBA Jobin Yvon Scientific XploRA dispersive confocal micro-Raman spectrometer with a laser excitation of λ=532 nm. Prior to analysis the sample was ground slightly and polished to expose a fresh surface.

Results

Petrographic observations of SM3 show rounded, light-colored clasts and chondrules (some with fine-grained rims) embedded in dark, fine-grained matrix (Fig. 2.1a). Irregularly shaped 10 to 250 μm bluish-white grains are distributed throughout the matrix (Fig. 2.1a, 2.1b): these grains are Ca-rich (Fig. 2.1d). Many of the Ca-rich grains are also S-rich, with below detectable levels of other metals (Fig. 2.1c). These Ca-S-rich grains are uniformly distributed across much of the polished mount (area ~1 cm^2). Some grains are embedded in the light-colored olivine-rich clasts, whereas many are in the matrix. Larger Ca-rich grains often have S-rich exteriors and S-free cores (Fig. 2.1c, 2.2). In addition to Ca, WDS and element mapping show that the S-free cores are O-rich, with minor Cl (Ca:O ratio near 0.44 and ~2 wt.% Cl). The Ca-O-rich cores are exceedingly electron-beam sensitive. The two largest grains (~200 μm across) are rimmed: one with olivine and the other Fe-Ni sulfide (Fig. 2.2). These grains are the only ones observed with this petrographic relationship and are also observed through computed tomography scans (Ebel and Hill 2012; Jenniskens et al. 2012). The WDS maps show that Cl is largely associated with the Ca-O-rich cores at the ~2 wt.% level, with a few grains displaying higher concentrations (bright blue grain arrowed in Fig. S1). Chlorine correlates with Ca, and is not associated with higher concentrations of other metals such as Na, K, or Mg.
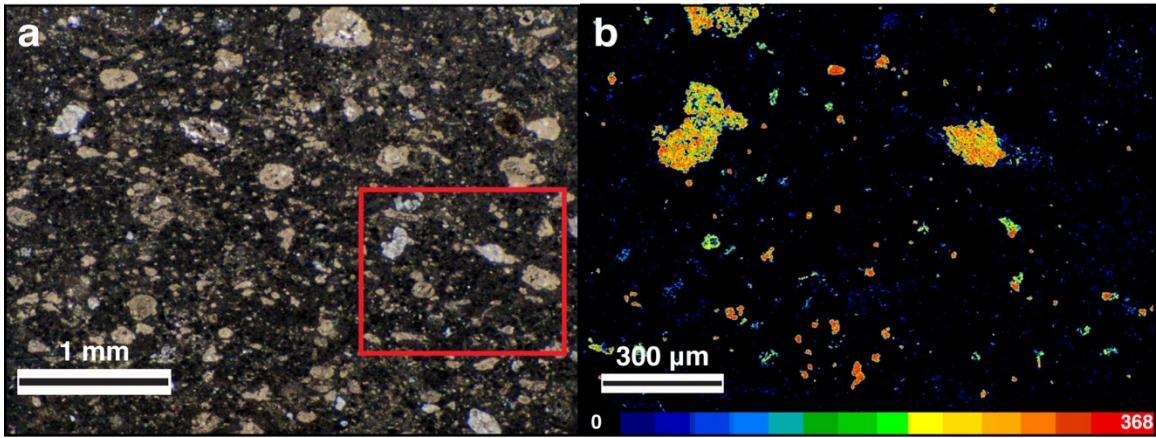
Figure 2.3. **a**) Optical micrograph of a representative polished area of SM41 showing rounded tan-colored olivine similar to SM3 and white grains of calcite in dark fine-grained matrix. (**b**) Calcium map of the area enclosed by the red box shown in (**a**).

SM41 is similar in appearance to SM3 (Fig. 2.3), with rounded, light-colored clasts and chondrules embedded in dark fine-grained matrix. Irregularly shaped white grains of calcite 10-300 μm in size are distributed uniformly across the sample. Calcium and S element distributions are not correlated, revealing the absence of Ca-S-bearing grains.

The SM3 powder XRD patterns are dominated by intense, broad reflections from olivine, with less-intense reflections from Fe-sulfides (pentlandite, troilite), magnetite, oldhamite, and traces of enstatite. Absent are the 13.5 Å and 7.3 Å 001 basal reflections characteristic of smectite and serpentine clays, respectively. A large (150 μm), altered Fe-Ni metal grain was also identified through petrographic and electron microprobe analysis (Haberle et al. 2014). Relative to the dominant olivine phase, the XRD patterns from five separate ~2-mm-sized SM3 chips are similar, with minor intensity differences reflecting small variations in the non-olivine components. The powder pattern from SM2 is similar to that from SM3, showing oldhamite reflections and higher intensity reflections for enstatite. In comparison, SM41 is dominated by reflections from phyllosilicates and a large amorphous contribution, with lesser Fe-sulfides, calcite, magnetite, olivine, and enstatite. No oldhamite or Ca sulfate was detected by XRD. Also absent from SM41 are reflections from tochilinite, a common mineral in CM2 chondrites.

Heated to 1000 °C, the TG data from SM3 show mass loss of 2.5 wt%, whereas SM41 has mass loss of 11.4 wt%. The SM stones exhibit low mass losses compared to CM and CI carbonaceous chondrites, for instance, Murchison (CM2) and Orgueil (CI1) experienced losses of 15 wt% and 22 wt%, respectively.

Raman spectra from the large Ca-rich grain in Figure 2.2b show bands at 356, 1080, 1331, 1583, and 3620 cm^{-1} (Fig. 2.4). The sharp bands at 356 and 3620 cm^{-1} correspond to the v2 bending and v1 OH stretching of $Ca(OH)_2$, respectively (Schmid
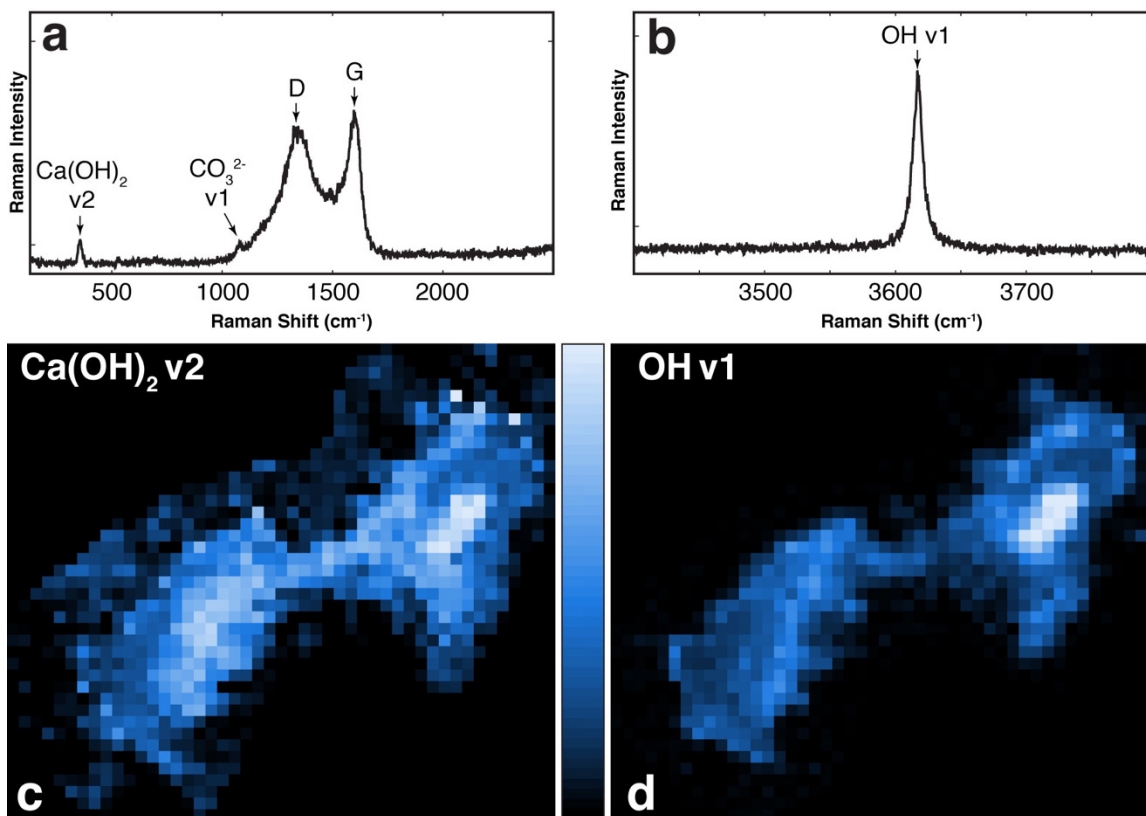
Figure 2.4. Raman spectra collected from the grain highlighted with a red box in *figure 2.2***b**. Spectra from the low- (**a**) and high- (**b**) wavenumber spectral regions are labeled with band assignments discussed in text: v1 OH stretching, v2 Ca(OH)$_2$ bending, v1 C-O stretching of calcite, and disordered carbon (D) and graphite (G). Raman peak amplitude maps (**c** and **d**) highlight two strong portlandite Raman peaks and show its distribution is concentrated within the center of the grain, consistent with elemental distribution maps.

and Dariz 2015). The weak Raman mode at 1080 cm^{-1} corresponds to the v1 C-O stretching mode of calcite (Schmid and Dariz 2015; Ševčík et al. 2016). The broad modes at 1350 and 1580 cm^{-1} match those of the disordered carbon (D) and graphite (G) Raman active modes present in a variety of carbonaceous materials (Bonal et al. 2006; Quirico et al. 2009).

The powder XRD data show that SM3 contains abundant oldhamite. WDS data show multiple dispersed Ca-S-rich grains consistent with oldhamite. The largest grains have S-free, Ca-O-rich cores, with Raman data consistent with portlandite.

Discussion

Evidence for indigenous oldhamite and portlandite. The XRD, Raman, and elemental data show the presence of oldhamite and portlandite; both are moisture sensitive. The occurrence of oldhamite in the olivine-rich pre-rain stones (SM2 and 3) and absence in the olivine-rich rained-on stones (Garvie 2013; Zolensky et al., 2014) shows the ease with which this mineral is altered by water and speaks to the minimal terrestrial contamination of SM3. The presence of portlandite can be explained as either terrestrial alteration or as indigenous to SM3. In the former case, portlandite would have formed through terrestrial hydration of extraterrestrial lime (CaO). We consider this unlikely, as SM3 was not exposed to rain. In addition, the olivine-rich pre-rain stones (SM2 and 3) are unlike other CM-like carbonaceous chondrites in being very hard and sintered (also noted by Zolensky et al. 2014), thus limiting the exposure of interior surfaces to atmospheric moisture. Also, hydration of lime would have led to volume expansion as portlandite has a molar volume (33.08 cm^3/mol) twice that of lime (16.79 cm^3/mol) (Kudłacz and Rodriguez-Navarro 2014). Evidence of this expansion would be apparent on a cut surface and has not been observed on the prepared specimens. These lines of evidence are consistent with the portlandite being indigenous to SM3.

Sutter's Mill lithologies. The Sutter's Mill fall is unusual in that it consists of stones with olivine-rich and phyllosilicate/amorphous-rich mineralogies. Only one of the stones previously studied, SM8, is olivine-rich and shows weak phyllosilicate reflections (Garvie 2013). The bulk $\delta^{18}O$ value of the phyllosilicate-rich stones is 13-18‰ and overlaps that of the olivine-rich stones, which span 11-27‰ (Ziegler and Garvie 2013). These data overlap with the CM field but are also ^{16}O-poor extending to values of the metamorphosed CM-like chondrites (Ivanova et al. 2010). Given the petrographic, though not mineralogical, similarities between the hydrated and anhydrous stones (Figs. 2.1 and 2.3), and the oxygen isotopic data, we suggest that they are genetically related. In this scenario, the anhydrous SM3 derives from SM41-like material through in-situ thermal metamorphism on the Sutter's Mill parent body.

Evidence for thermal metamorphism of SM3. SM3 shows low mass loss during TG analysis (2.5 wt%), with its mineralogy dominated by olivine, with an absence of phyllosilicates. Thermally metamorphosed CM carbonaceous chondrites, such as Belgica 7904 (Tomeoka 1990), Yamato 86720 (Tomeoka et al. 1989a), Dhofar 225 and Dhofar 735 (Ivanova et al. 2010), are also olivine-rich with low water contents. It has been posited (Tomeoka et al. 1989a; Tomeoka 1990; Ivanova et al. 2010) that these stones experienced extraterrestrial thermal metamorphism that dehydrated phyllosilicates leading to recrystallization of olivine and minor enstatite (Brindley and Hiyami 1965; Akai 1992). The XRD profiles of recrystallized secondary olivine exhibit broad diffraction peaks that are distinct from the sharp reflections of primary olivine (Nakamura 2005). The olivine diffraction peaks in SM3 are similarly broad consistent with secondary olivine that recrystallized from matrix phyllosilicates. The temperature required to initiate this reaction is ~400° C, with complete dehydroxylation and recrystallization to olivine occurring at ~750° C (Brindley and

20

Hiyami 1965; Akai 1990,1992; Nakamura 2005; Ivanova et al. 2010; Tonui et al. 2014).

Thermal metamorphism of calcite to oldhamite and portlandite. Calcite is common in CM chondrites and is also present in SM41 (Johnson and Prinz 1993; Garvie 2013). We propose that calcite originally present in SM3 was calcined to lime. The calcination reaction is endothermic and decomposition typically initiates above 600° C (Rodriguez-Navarro et al. 2009; Galan et al. 2013), though can begin ~400 °C (Wang and Thomson 1995). Various factors, related to the physical properties of the material and partial pressure of CO_2, influence the initiation temperature and rate of reaction but, in general, higher temperature favors the forward reaction (Stanmore and Gilot 2005). The kinetics of the calcination reaction is thoroughly studied, as it is a reaction frequently utilized in a number of industrial processes.

Lime is commonly employed as a sorbent to capture sulfur emissions from coal-fired electricity-generating plants and this can lead to the formation of oldhamite under reducing conditions (Hansen et al. 1993; Agnihotri et al. 1999). There are two similar reactions that induce oldhamite formation, both utilize lime to react with S-bearing gases (SO_2 and H_2S; Hansen et al. 1993; Agnihotri et al. 1999); these gases are also common volatile products of heated CM and CI carbonaceous chondrites (Gibson et al. 1972, 1974a, 1974b; Court and Sephton 2014; Court and Tan 2016). For example, upon heating to 1000°C, Murray (CM2), Murchison (CM2), and Orgueil (CI1) release SO_2, with a trimodal release pattern with peaks located at ~250°C, 400-500 °C, and 600-800 °C. Murray and Orgueil also exhibit release of H_2S at ~450°C, with Murray showing additional release >800°C (Gibson et a. 1972, 1974a, 1974b).
 At high temperature lime reacts with SO_2 to form CaS or $CaSO_4$ depending upon the reducing potential P_{CO}/P_{CO_2} of the system (Oh and Wheelock 1990; Hansen et al. 1993).

When the reducing potential is elevated (>0.2), the formation of oldhamite is favored through:

$$CaO + SO_2 + 3CO \rightarrow CaS + 3CO_2 \tag{1}$$
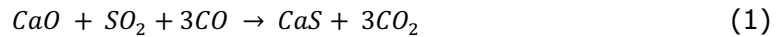
Alternatively, above 700°C with > 2000 ppm H_2S, oxide sulfidation of CaO will occur through:

$$CaO + H_2S \rightarrow CaS + H_2O \tag{2}$$

Both reactions form oldhamite along the exterior of the grain with a reaction front propagating inward. In SM3, grains smaller than ~50 μm have been completely converted to oldhamite, while larger grains retain a core of lime (Fig. 2.1, 2.2).

The residual interior lime is extremely hygroscopic and readily forms portlandite when exposed to water vapor (Dubina et al. 2011, 2013). Following the event that heated SM3, cooling could have resulted in retrograde hydration of lime to portlandite. Furthermore, in the presence of steam and CO_2, evidence suggests that portlandite can be stable well above its dehydration temperature (~450 °C) as a transient or intermediate phase during calcination and sulfidation (Wang et al. 2010; Materić et al. 2015). This high temperature stability suggests that any lime formed, which was not converted to oldhamite, could persist as portlandite.

The two largest oldhamite-portlandite grains have rims of olivine and Fe-Ni sulfide (Fig. 2.2). The CM chondrites, and several SM stones, contain calcite grains with rims, such as Mg-rich serpentine, serpentine-tochilinite, cronstedtite, Fe sulfides, and an unidentified O-S-Fe mineral (de Leuw et al. 2010; Lee et al. 2014; Zolensky et al. 2014; Fujiya et al. 2015). The rims surrounding type 1a calcite in CM chondrites (Fig. 8 in Lee et al. 2014) show textural similarities to the rims we observe in Figure 2.2c. We suggest that the rims we observe are the thermally metamorphosed equivalent to rims surrounding calcite grains in CM chondrites. In SM3, these rimmed grains are rare but they provide additional supporting evidence that the abundant

oldhamite grains were calcite prior to thermal metamorphism and are not xenocrysts from an enstatite chondrite or aubrite.

Implications

Formation of oldhamite and portlandite through thermal processing of CM carbonaceous chondrites presents a new understanding of the mineralogical transformations occurring on carbonaceous chondrite parent bodies. The formation of oldhamite is commonly observed in fluidized bed combustion (FBC) reactors, where crushed limestone is added to coal-fired reactors to reduce sulfur emissions. In addition to oldhamite, FBC ash typically contains large quantities of lime and portlandite revealing that it is a common end-product in high temperature combustion processes involving calcite and carbonaceous materials, such as coal. Gas-solid reactions used industrially for power generation and emission reduction have a parallel with heated CM carbonaceous chondrites and allow for the presence of portlandite and the reduced phase oldhamite without the need to invoke physical mixing of reduced enstatite chondrites or aubrites on the parent body. In addition, this study introduces portlandite as an indigenous meteoritic mineral.

Moreover, these results underline the importance of studying fresh meteorite falls and the need for their appropriate long-term curation. Oldhamite has not been reported from mineralogically similar chondrites e.g., Belgica 7904 (Tomeoka, 1990; Nakamura 2005). This absence could be the result of its water sensitivity and rapid decomposition. This sensitivity is illustrated by the presence of oldhamite in the two studied pre-rain, olivine-rich stones, SM2 and SM3, but not in the post-rain, olivine-rich stones.

Mineral assemblages of thermally metamorphosed CM carbonaceous chondrites are unique and can shed light into the processes that acted to modify primitive meteorite parent bodies. Oldhamite generated within a carbonaceous chondrite can be

a sensitive indicator of the redox conditions asteroidal material was exposed to during thermal metamorphism. Lime, portlandite, oldhamite, dehydrated phyllosilicates, and olivine each have characteristic spectral features that could be identified by the payload suites of the two sample collecting spacecraft currently travelling to suspected carbonaceous chondrites (OSIRIS-REx and Hayabusa II). As such, the identification and spatial distribution of these minerals on the surface of B- and C-type asteroids would be valuable for interpreting the thermal history of the materials exposed at the surface.

References

Agnihotri, R., Chauk, S.S., Mahuli, S.K., and Fan, L.S. (1999) Mechanism of CaO reaction with H_2S: Diffusion through CaS product layer. Chemical Engineering Science, 54, 3443-3453.

Akai, J. (1992) TTT diagram of serpentine and saponite, and estimation of metamorphic heating degree of Antarctic carbonaceous chondrites. Antarctic Meteorite Research, 5, 120.

Akai, J. (1990) Mineralogical evidence of heating events in Antarctic carbonaceous chondrites, Y-86720 and Y-82162. Antarctic Meteorite Research, 3, 55.

Anders, E. and Grevesse, N. (1989) Abundances of the elements: Meteoritic and solar. Geochimica et Cosmochimica Acta, 53, 197-214.

Bonal, L., Quirico, E., Bourot-Denise, M., and Montagnac, G. (2006) Determination of the petrologic type of CV3 chondrites by Raman spectroscopy of included organic matter. Geochimica et Cosmochimica Acta, 70, 1849-1863.

Brindley, G.W. and Hayami, R. (1965) Mechanism of formation of forsterite and enstatite from serpentine. Mineralogy Magazine, 35, 189-195

Browning, L.B., McSween, H.Y., and Zolensky, M.E. (1996) Correlated alteration effects in CM carbonaceous chondrites. Geochimica et Cosmochimica Acta, 60, 2621-2633.

Burgess, R., Wright, I.P., and Pillinger, C.T. (1991) Determination of sulphur‐bearing components in C1 and C2 carbonaceous chondrites by stepped combustion. Meteoritics, 26, 55-64.

Court, R.W. and Sephton, M.A. (2014) New estimates of the production of volatile gases from ablating carbonaceous micrometeoroids at Earth and Mars during an E-belt-type Late Heavy Bombardment. Geochimica et Cosmochimica Acta, 145, 175-205.

Court, R.W. and Tan, J. (2016) Insights into secondary reactions occurring during atmospheric ablation of micrometeoroids. Meteoritics and Planetary Science, 51, 1163-1183.

de Leuw, S., Rubin, A.E., and Wasson, J.T. (2010) Carbonates in CM chondrites: Complex formational histories and comparison to carbonates in CI chondrites. Meteoritics and Planetary Science, 45, 513-530.

Dubina, E., Wadsö, L., and Plank, J. (2011) A sorption balance study of water vapour sorption on anhydrous cement minerals and cement constituents. Cement and Concrete Research, 41, 1196-1204.

Dubina, E., Korat, L., Black, L., Strupi-Šuput, J., and Plank, J. (2013) Influence of water vapour and carbon dioxide on free lime during storage at 80 C, studied by Raman spectroscopy. Spectrochimica Acta Part A: Molecular and Biomolecular Spectroscopy, 111, 299-303.

Ebel, D.S. and Hill, M. (2012) Computed Tomography (CT) of five samples of the Sutter's Mill CM2 chondrite. (Online). Available: http://digitallibrary.amnh.org/handle/2246/6408 (accessed July 7, 2016). American Museum of Natural History, New York, New York.

Elvis, M. (2013) Prospecting asteroid resources. In Asteroids: Prospective energy and material resources. P. 81-129 Springer Berlin Heidelberg.

Fries, M., Le Corre, L., Hankey, M., Fries, J., Matson, R., Schaefer, J., and Reddy, V. (2014) Detection and rapid recovery of the Sutter's Mill meteorite fall as a model for future recoveries worldwide. Meteoritics and Planetary Science, 49, 1989-1996.

Fujiya, W., Sugiura, N., Marrocchi, Y., Takahata, N., Hoppe, P., Shirai, K., Sano, Y., and Hiyagon, H. (2015) Comprehensive study of carbon and oxygen isotopic compositions, trace element abundances, and cathodoluminescence intensities of calcite in the Murchison CM chondrite. Geochimica et Cosmochimica Acta 161, 101-117.

Galan, I., Glasser, F.P., and Andrade, C. (2013) Calcium carbonate decomposition. Journal of Thermal Analysis and Calorimetry, 111, 1197-1202.

Garvie, L.A.J. (2013) Mineralogy of the Sutter's Mill Carbonaceous Chondrite. 44th Lunar and Planetary Science Conference, Abstract #2148.

Gibson, E.K. Jr. and Johnson, S.M. (1972) Thermogravimetric-quadrupole mass-spectrometric analysis of geochemical samples. Thermochimica Acta, 4, 49-56.

Gibson, E.K. Jr. (1974a) Inorganic gas release studies and thermal analysis investigations on carbonaceous chondrites. Meteoritics, 9, 343-344.

Gibson, E.K., Moore, G.W., and Johnson, S.M. (1974b) Summary of analytical data from gas release investigations, volatilization experiments, elemental

abundance measurements on lunar samples, meteorites, minerals, volcanic ashes and basalts. NASA L.B. Johnson Space Center, Houston, Tex.

Grossman, L., Beckett, J.R., Fedkin, A.V., Simon, S.B. and Ciesla, F.J. (2008) Redox conditions in the solar nebula: Observational, experimental, and theoretical constraints. Reviews in Mineralogy and Geochemistry, 68, 93-140.

Haberle, C.W., Garvie, L.A.J, Domanick, K., and Christensen, P.R. (2014) Mineralogical complexity of altered kamacite in Sutter's Mill (SM3, pre-rain): insights into asteroidal dehydration. 45th Lunar and Planetary Science Conference, Abstract #2818

Hansen, P., Dam-Johansen, K., and Østergaard, K. (1993) High-temperature reaction between sulphur dioxide and limestone—V. The effect of periodically changing oxidizing and reducing conditions. Chemical Engineering Science, 48, 1325-1341.

Ivanova, M.A., Lorenz, C.A., Nazarov, M.A., Brandstaetter, F., Franchi, I.A., Moroz, L.V., Clayton, R.N., and Bychkov, A.Y. (2010) Dhofar 225 and Dhofar 735: Relationship to CM2 chondrites and metamorphosed carbonaceous chondrites, Belgica-7904 and Yamato-86720. Meteoritics and Planetary Science, 45, 1108-1123.

Jenniskens, P., Fries, M.D., Yin, Q.Z., Zolensky, M., Krot, A.N., Sandford, S.A., Sears, D., Beauford, R., Ebel, D.S., Friedrich, J.M., and Nagashima, K. (2012) Radar-enabled recovery of the Sutter's Mill meteorite, a carbonaceous chondrite regolith breccia. Science, 338, 1583-1587.

Johnson, C.A. and Prinz, M. (1993) Carbonate compositions in CM and CI chondrites and implications for aqueous alteration. Geochimica et Cosmochimica Acta, 57, 2843-2852.

Kudłacz, K. and Rodriguez-Navarro, C. (2014) The mechanism of vapor phase hydration of calcium oxide: implications for CO_2 capture. Environmental Science and Technology, 48, 12411-12418.

Larimer, J.W. and Bartholomay, M. (1979) The role of carbon and oxygen in cosmic gases: Some applications to the chemistry and mineralogy of enstatite chondrites. Geochimica et Cosmochimica Acta, 43, 1455-1466.

Lee, M.R., Lindgren, P., and Sofe, M.R. (2014) Aragonite, breunnerite, calcite and dolomite in the CM carbonaceous chondrites: High fidelity recorders of progressive parent body aqueous alteration. Geochimica et Cosmochimica Acta, 144, 126-156.

Lewis, J.S., McKay, D.S., and Clark, B.C. (1993) Using resources from near-Earth space. In Lewis J., Matthews M.S., Guerrieri M.L., Eds. Resources of Near-Earth Space, p.3-14, The University of Arizona Press, Tucson&London

Materić, V., Ingham, B., and Holt, R. (2015) In situ synchrotron XRD investigation of the dehydration and high temperature carbonation of $Ca(OH)_2$. CrystEngComm, 17, 7306-7315.

McSween, H.Y. (1979) Alteration in CM carbonaceous chondrites inferred from modal and chemical variations in matrix. Geochimica et Cosmochimica Acta, 43, 1761-1770.

Nakamura, T. (2005) Post-hydration thermal metamorphism of carbonaceous chondrites. Journal of the Mineralogical and Petrological Sciences, 100, 260-272.

Nozaki, W., Nakamura, T. and Noguchi, T. (2006) Bulk mineralogical changes of hydrous micrometeorites during heating in the upper atmosphere at temperatures below 1000 C. Meteoritics and Planetary Science, 41, 1095-1114.

Oh, J.S., and Wheelock, T.D. (1990) Reductive decomposition of calcium sulfate with carbon monoxide: reaction mechanism. Industrial and Engineering Chemistry Research, 29, 544-550.

Okada, A., Keil, K., and Taylor, G.J. (1981) Unusual weathering products of oldhamite parentage in the Norton County enstatite achondrite. Meteoritics, 16, 141-152.

Piani, L., Marrocchi, Y., Libourel, G., and Tissandier, L. (2016) Magmatic sulfides in the porphyritic chondrules of EH enstatite chondrites. Geochimica et Cosmochimica Acta, 195, 84-99.

Pizzarello, S. and Garvie, L.A.J. (2014) Sutter's Mill dicarboxylic acids as possible tracers of parent-body alteration processes. Meteoritics and Planetary Science, 49, 2087-2094.

Quirico, E., Montagnac, G., Rouzaud, J.N., Bonal, L., Bourot-Denise, M., Duber, S., and Reynard, B. (2009) Precursor and metamorphic condition effects on Raman spectra of poorly ordered carbonaceous matter in chondrites and coals. Earth and Planetary Science Letters, 287, 185-193.

Rabade, S., Barba, N., Garvie, L.A.J., and Thangavelautham, J. (2016) The case for solar thermal steam propulsion system for interplanetary travel: Enabling simplified ISRU utilizing NEOs and small bodies. 67th International Astronautical Congress, Abstract Code: IAC-16,D4,5,7,x34659

Rodriguez-Navarro, C., Ruiz-Agudo, E., Luque, A., Rodriguez-Navarro, A.B., and Ortega-Huertas, M. (2009) Thermal decomposition of calcite: Mechanisms of formation and textural evolution of CaO nanocrystals. American Mineralogist, 94, 578-593.

Rubin, A.E. (1997) Mineralogy of meteorite groups. Meteoritics and Planetary Science, 32, 231-247

Rubin, A.E., Trigo-Rodríguez, J.M., Huber, H., and Wasson, J.T. (2007) Progressive aqueous alteration of CM carbonaceous chondrites. Geochimica et Cosmochimica Acta, 71, 2361-2382

Schmid, T. and Dariz, P. (2015) Shedding light onto the spectra of lime: Raman and luminescence bands of CaO, $Ca(OH)_2$ and $CaCO_2$. Journal of Raman Spectroscopy, 46, 141-146.

Ševčík, R., Mácová, P., Sotiriadis, K., Pérez-Estébanez, M., Viani, A., and Šašek, P. (2016) Micro-Raman spectroscopy investigation of the carbonation reaction in a lime paste produced with a traditional technology. Journal of Raman Spectroscopy, 47, 1452-1457.

Stanmore, B.R. and Gilot, P. (2005) Review—calcination and carbonation of limestone during thermal cycling for CO 2 sequestration. Fuel Processing Technology, 86, 1707-1743

Tomeoka, K. and Buseck, P.R. (1985) Indicators of aqueous alteration in CM carbonaceous chondrites: Microtextures of a layered mineral containing Fe, S, O and Ni. Geochimica et Cosmochimica Acta, 49, 2149-2163.

Tomeoka, K., Kojima, H., and Yanai, K. (1989a) Yamato-86720: A CM carbonaceous chondrite having experienced extensive aqueous alteration and thermal metamorphism. In Proceedings of the NIPR Symposium on Antarctic Meteorites, 2, 55-74.

Tomeoka, K., Kojima, H., and Yanai, K. (1989b) Yamato-82162: A new kind of CI carbonaceous chondrite found in Antarctica. In Proceedings of the NIPR Symposium on Antarctic Meteorites, 2, 36-54.

Tomeoka, K. (1990) Mineralogy and petrology of Belgica-7904: A new kind of carbonaceous chondrite from Antarctica. Antarctic Meteorite Research, 3, 40.

Tonui, E., Zolensky, M., Lipschutz, M., Wang, M., and Nakamura, T. (2003) Yamato 86029: Aqueously altered and thermally metamorphosed CI-like chondrite with unusual textures. Meteoritics and Planetary Science, 38, 269-292

Tonui, E., Zolensky, M., Hiroi, T., Nakamura, T., Lipschutz, M.E., Wang, M.S., and Okudaira, K. (2014) Petrographic, chemical and spectroscopic evidence for thermal metamorphism in carbonaceous chondrites I: CI and CM chondrites. Geochimica et Cosmochimica Acta, 126, 284-306.

Wang, Y. and Thomson, W.J. (1995) The effects of steam and carbon dioxide on calcite decomposition using dynamic X-ray diffraction. Chemical Engineering Science, 50, 1373-1382.

Wang, C., Jia, L., Tan, Y., and Anthony, E.J. (2010) The effect of water on the sulphation of limestone. Fuel, 89, 2628-2632.

Yamakawa, A. and Yin, Q.Z. (2014) Chromium isotopic systematics of the Sutter's Mill carbonaceous chondrite: implications for isotopic heterogeneities of the early Solar System. Meteoritics and Planetary Science, 49, 2118-2127.

Ziegler, K. and Garvie, L.A.J. (2013) Bulk oxygen-isotope compositions of different lithologies in Sutter's Mill. 76th Annual Meteoritical Society Meeting, Abstract #5225.

Zolensky, M. and Ivanov, A. (2003) The Kaidun microbreccia meteorite: A harvest from the inner and outer asteroid belt. Chemie der Erde-Geochemistry, 63, 185-246.

Zolensky, M., Herrin, J., Mikouchi, T., Ohsumi, K., Friedrich, J., Steele, A., Rumble, D., Fries, M., Sandford, S., Milam, S. and Hagiya, K. (2010) Mineralogy and petrography of the Almahata Sitta ureilite. Meteoritics and Planetary Science, 45, 1618-1637.

Zolensky, M., Mikouchi, T., Fries, M., Bodnar, R., Jenniskens, P., Yin, Q.Z., Hagiya, K., Ohsumi, K., Komatsu, M., Colbert, M., and Hanna, R. (2014) Mineralogy and petrography of C asteroid regolith: The Sutter's Mill CM meteorite. Meteoritics and Planetary Science, 49, 1997-2016.

CHAPTER 3

Remote Identification of Dehydrated Carbonaceous Regolith: Insights for

Asteroid Sample Return Missions

Introduction

Chondrites are aggregates of primitive Solar System components, some of which are the oldest solids known to have formed in our nebular disc (Tatsumoto et al., 1973; Bouvier and Wadhwa, 2010). Consequently, chondritic meteorites and their asteroid counterparts are interpreted to be the primitive remnants of planetary formation and are integral to understanding early Solar System evolution. The carbonaceous class of chondrites generates increased scientific interest owing to the presence of abundant extraterrestrial organic carbon. The most carbon-rich members of this class, the CI and CM groups, are also hydrated; containing as much as 22 wt. % OH/H_2O (Brearly and Jones, 1998; Weisburg et al., 2006). These three characteristics (primordial age, carbon-rich, and hydrous) make the carbonaceous chondrites, and the asteroids that potentially host them, critical to understanding the origin of water and life on Earth and also drive the level 1 science objectives of the OSIRIS-REx asteroid sample return mission (Lauretta et al., 2017). Earth-based spectroscopic investigations of asteroid Bennu, the target object for OSIRIS-REx, suggest that Bennu has a meteoritic analog in the CI and CM chondritic meteorites (Clark et al., 2011). Herein we focus our investigation on CM and CM-like materials.

The CM chondrites are composed of varying proportions of matrix, chondrules, refractory inclusions (calcium aluminum inclusions and amoeboid olivine aggregates), and Fe-Ni metal. Of these components, matrix is dominant accounting for roughly 75 % of CM materials by volume (McSween, 1979; Howard et al., 2009, 2011). Matrix is a fine-grained (nm scale), optically opaque mixture of silicates, oxides, sulfides, and Fe-Ni metal (Buseck and Hua, 1993; Scott and Krot, 2014). Within the CM chondrite

matrices, phyllosilicates are the most abundant minerals, thought to be formed through prolonged low temperature aqueous alteration on the CM chondrite parent body (McSween, 1979; Tomeoka and Busek, 1985; Browning et al., 1996; Rubin et al., 2007). While compositional diversity exists, the majority of the observed phyllosilicates are Fe^{3+}-rich cronstedtite and ferroan Mg-serpentine (Barber, 1981; Zolensky et al., 1993; Howard, 2009, 2011). Transmission Electron Microscopy (TEM) investigations of matrix phyllosilicates show that Fe^{3+}-rich cronstedtite commonly occurs as relatively coarse (1-10 μm) platy laths whereas ferroan Mg-serpentine is observed as fine-grained, poorly crystalline, fibrous crystals (Barber, 1981). This complicated mineral mixture contains many phases that have characteristic spectral signatures across the visible and near infrared (VNIR) portion of the electromagnetic spectrum, where the OSIRIS-REx Visible Infrared Spectrometer (OVIRS) and Camera Suite (OCAMS) are sensitive (Reuter et al., 2018; Rizk et al., 2018).

Reflectance spectroscopy studies of low albedo asteroids, like Bennu, and CM chondrites show characteristic absorption features consistent with Fe-bearing serpentine minerals (Vilas and Gaffey, 1989; King and Clark, 1989; Hiroi et al., 1994; Hiroi et al., 1996; Calvin and King, 1997; Cloutis et al., 2011a). Serpentine group phyllosilicates have characteristic spectral features originating from two types of absorption processes: electronic transition absorptions arising from the presence of $Fe^{2+/3+}$ and vibrational absorptions resulting from the bending and stretching modes of OH/H_2O (Clark et al., 1990; Burns, 1993). In the serpentine group, absorption processes lead to a steep ultraviolet (UV) drop-off at $\sim$ 0.6 μm and absorption features between 0.6 – 1.2 μm. The strong UV drop-off is due to intense oxygen-metal charge transfer (OMCT) absorptions centered in the far-UV; the most common of which are owing to Fe^{2+} and Fe^{3+} (Loeffler et al., 1974; Burns, 1993). Compared to Fe^{2+}, the Fe^{3+} OMCT absorption is approximately two orders of magnitude more intense and the

absorption edge can extend from the UV well into the visible portion of the spectrum. Serpentine absorption features located between $0.6 - 1.2$ μm are generally an assemblage of three absorption bands with band centers located near 0.7, 0.9, and 1.0 μm, herein referred to as the serpentine bands. The band near 0.7 μm is assigned to a Fe^{2+} - Fe^{3+} intervalence charge transfer (IVCT) absorption due to the presence of ferric iron in the octahedral or tetrahedral (in the case of cronstedtite) crystallographic site. The 0.9 and 1.0 μm bands are attributed to crystal field (CF) absorptions of Fe^{2+} in the octahedral site.

In serpentines, the vibrational modes of $^-OH/H_2O$ are located near 1.4 ($2\nu1$ ^-OH), 1.9 ($\nu2$ H_2O + $\nu1$ ^-OH), 2.3 ($\nu2$ metal-OH + $\nu1$ ^-OH), and 2.8 μm ($\nu1$ ^-OH). Previous studies have shown that the presence of fine-grained, strongly absorbing, opaque phases (e.g. magnetite, Fe-sulfides, organic material, Fe-Ni metal) within CM chondrite matrices can suppress or completely mask the absorption features of many minerals (Johnson and Fanale, 1973; Clark, 1983; Cloutis et al., 1990; Milliken and Mustard, 2007). In the case of CM phyllosilicate minerals, the 1.4 μm overtone and 1.9 μm combination features are effectively obscured. From this point on we focus on fundamental OH features. The strong absorption near 2.7 - 2.8 μm is due to the fundamental O-H stretching mode of structurally bound OH while the broad absorption centered at 2.9 μm is associated with overlapping O-H stretching modes of free water (Aines and Rossman, 1984; Salisbury, 1987). The hydroxyl absorption position in CM chondrite spectra is related to the composition of the phyllosilicates: positioned near 2.72 μm in Mg-serpentines (e.g. lizardite and antigorite) and 2.8 μm in cronstedtite (King and Clark, 1989; Calvin and King, 1997; Takir et al., 2013).

In addition to aqueous alteration, the CM chondrites can experience varying degrees of post-hydration thermal metamorphism with peak temperatures ranging from ~250 °C for weakly heated to >750 °C for strongly heated stones (Ikeda et al.,

33

1992; Nakamura, 2005; Tonui et al., 2014; Haberle and Garvie, 2017). Thermal metamorphism of CM chondrites drives off volatile elements, destroys aliphatic organic compounds, and dehydrates phyllosilicate minerals ultimately leading to depletions in bulk carbon and water contents (Brindley and Hiyami, 1965; Gibson et al., 1972; Tomeoka et al., 1989a, 1989b; Tonui et al., 2014). Mineralogically, the most significant change is the progressive breakdown of phyllosilicates as these constitute approximately ~60 – 85% of the bulk mineralogy (McSween, 1979; Howard et al., 2009, 2011). Phyllosilicate breakdown begins with dehydration followed shortly thereafter by amorphization then ultimately recrystallization. Crystallization of anhydrous olivine and minor enstatite occur at peak thermal metamorphic conditions (>750 °C) (Brindley and Zussman, 1957; Brindley and Hiyami, 1965; Akai et al., 1992; Nakamura, 2005; Tonui et al., 2014). Thermal metamorphism is well documented in CM chondrites and is distinctively expressed through changes in matrix mineralogy (Akai, 1992; Ikeda et al., 1992; Nakamura, 2005; Tonui et al., 2014).

Mineralogical changes due to thermal metamorphism have been observed in the visible to near-infrared (VNIR) reflectance spectra of experimentally and naturally heated CM chondrites (Matza and Lipschutz, 1977; Hiroi et al., 1994; Hiroi et al., 1996; Cloutis et al., 2012; Tonui et al., 2014). Heating of CM materials, in general, leads to a reduction in UV absorption, diminished intensity of the serpentine bands, disappearance of the 0.7 μm IVCT feature, and progressive weakening of the fundamental OH band. In addition, aliphatic compounds in CM chondrites exhibit a C-H stretching absorption near 3.4 μm that is diminished as hydrogen is lost during heating and graphitization (French, 1964; Ito et al., 1987; Cloutis et al., 1994; Clark et al., 2009). Graphitization of CM organics leads to darkening and a progressively reduced spectral slope across the spectrum (Cloutis et al., 1994; Cloutis et al., 2012).

Stones collected from the recent Sutter's Mill fall (April 22, 2012) are classified as carbonaceous with no further group association. Chemically, Sutter's Mill exhibits bulk geochemical and isotopic similarities to the CM group (Jenniskens et al., 2012; Zolensky et al., 2014). These observations and the petrographic similarities of Sutter's Mill and CM group chondrites has led researchers to strongly recommend an amendment to the official classification of Sutter's Mill from C class to CM group (Zolensky et al., 2014). Excess solar implanted Ne and the angular to rounded appearance of lithic clasts and mineral fragments indicate Sutter's Mill is a regolith breccia composed of surface materials from a carbonaceous asteroid (Jenniskens et al., 2012; Zolensky et al., 2014). Mineralogically, Sutter's Mill hosts at least two lithologic components: phyllosilicate-bearing (similar to CM2) and olivine-rich (similar to CM2 heated to >750 °C). The presence of both hydrous and thermally metamorphosed CM-like lithologies within Sutter's Mill shows that these materials existed together mixed within the regolith of the Sutter's Mill parent asteroid. All other specimens of thermally metamorphosed CM materials are finds (most notably the Antarctic finds) and lack the context provided by the Sutter's Mill suite where a witnessed and rapidly collected fall hosts variably heated materials within the same parent body. These characteristics make Sutter's Mill a fortuitous and unique analog to C-complex asteroid regolith, like that which may exist on asteroid Bennu, the target for the OSIRIS-REx asteroid sample return mission.

Here we provide new observations of hydrous carbonaceous chondrite samples that have been naturally heated at a range of temperatures. In addition, we provide observations of the most recent CM2 chondrite fall (June 6, 2017), Mukundpura (Ray and Shukla, 2018). Each of these samples were collected rapidly after an observed fall, minimizing their time spent exposed to the terrestrial atmosphere. Sample SM3 is especially fresh, having been collected before rain fell over the recovery site. Our

investigation characterizes the hydration state and mineralogy of individual samples and relates these properties to the spectral features displayed by each.

Methods and Materials:

The samples analyzed in this study are CM2 chondrites (Cold Bokkeveld, Mighei, Mukundpura, Murchison, Nogoya, and Santa Cruz) and individual stones from the Sutter's Mill C chondrite regolith breccia (SM2, SM3, 2 splits of SM6, three splits of SM8, SM12, SM38, SM41, SM49, two splits of SM53, two splits of SM65 and SM 71). All samples were obtained from Arizona State University's Center for Meteorite Studies where the Sutter's Mill samples have been stored under dry nitrogen, with limited exposure to atmospheric moisture.

Samples of Murchison, SM41, and SM3 were prepared for X-ray diffraction (XRD) from ~10 mg of material. The samples were crushed in a mortar pestle and mixed with a few mL of dry methanol. The resulting slurry was spread to form a thin, smooth film on a low-background single-crystal quartz plate and then dried rapidly under flowing warm air. A Rigaku MiniFlex 600 diffractometer, with a post-diffraction monochromator, employing Cu Kα radiation was utilized to collect powder XRD profiles. Profiles were acquired at 0.02° steps from 2 to 65°, with a 60 s/step integration time. XRD data from Sutter' Mill stones have also been described in prior publications (Garvie, 2013; Pizzarello and Garvie, 2104; Haberle and Garvie, 2017).

Thermogravimetric analysis (TGA) data were acquired for Murchison, Mukundpura, SM41, and SM3. Data were acquired from ~40 mg samples heated under flowing He from 20 to 1000 °C, with a heating rate of 10 °C/min.

VNIR reflectance data were collected for each sample listed above from 0.35 - 2.5 μm using an ASD FieldSpec 3 spectroradiometer. All VNIR observations were made using a fiber optic cable attached to a goniometer at a 0° emergence angle with a 50 W quartz-tungsten-halogen source at a 30° incidence angle. Absolute reflectance was

calculated relative to a Spectralon® 20% diffuse reflectance target from Labsphere. Each spectrum is the average of ten observations each consisting of 100 co-added scans for a total of 1000 scans averaged per spectrum. The standard deviation for each set of ten observations was calculated to characterize and minimize the observational errors within and between measurements.

The modified Gaussian model (MGM) was employed to determine the shape and number of electronic transition absorption bands located near 1 micron (Sunshine et al., 1990). MGM modeling was performed on spectra from 0.35 - 1.8 μm using a three-component continuum similar to that used for analysis of lunar soil samples (Hiroi et al., 2000; Noble et al., 2006). Starting values for band center, width (FWHM) and strength were determined based on the results of Cloutis et al., (2011a, 2011b) and refined until the starting parameters gave reproducible, realistic results. These starting conditions were then used to model every spectrum collected. An additional set of starting values was assembled for the olivine-rich Sutter's Mill stones based upon the olivine band positions presented in Sunshine and Pieters, (1998). The threshold to cease the RMS minimization is determined from the standard deviation calculated to characterize the observational error.

In order to evaluate the spectral variability that can be observed with the OSIRIS-REx Camera Suite (OCAMS), VNIR data were converted to the expected relative reflectance (I/F) values for each science filter used by the OCAMS MapCam instrument. Profiles for filter transmission, detector quantum efficiency (QE), and relative solar output were used to calculate the expected response for each filter and convolve the VNIR spectra to I/F resulting in a single value for the panchromatic filter and a 4-point MapCam spectrum (Rizk et al., 2017). Using the 4-point spectrum, 0.7 μm band depth, UV absorption strength, UV slope and sinuosity were calculated.
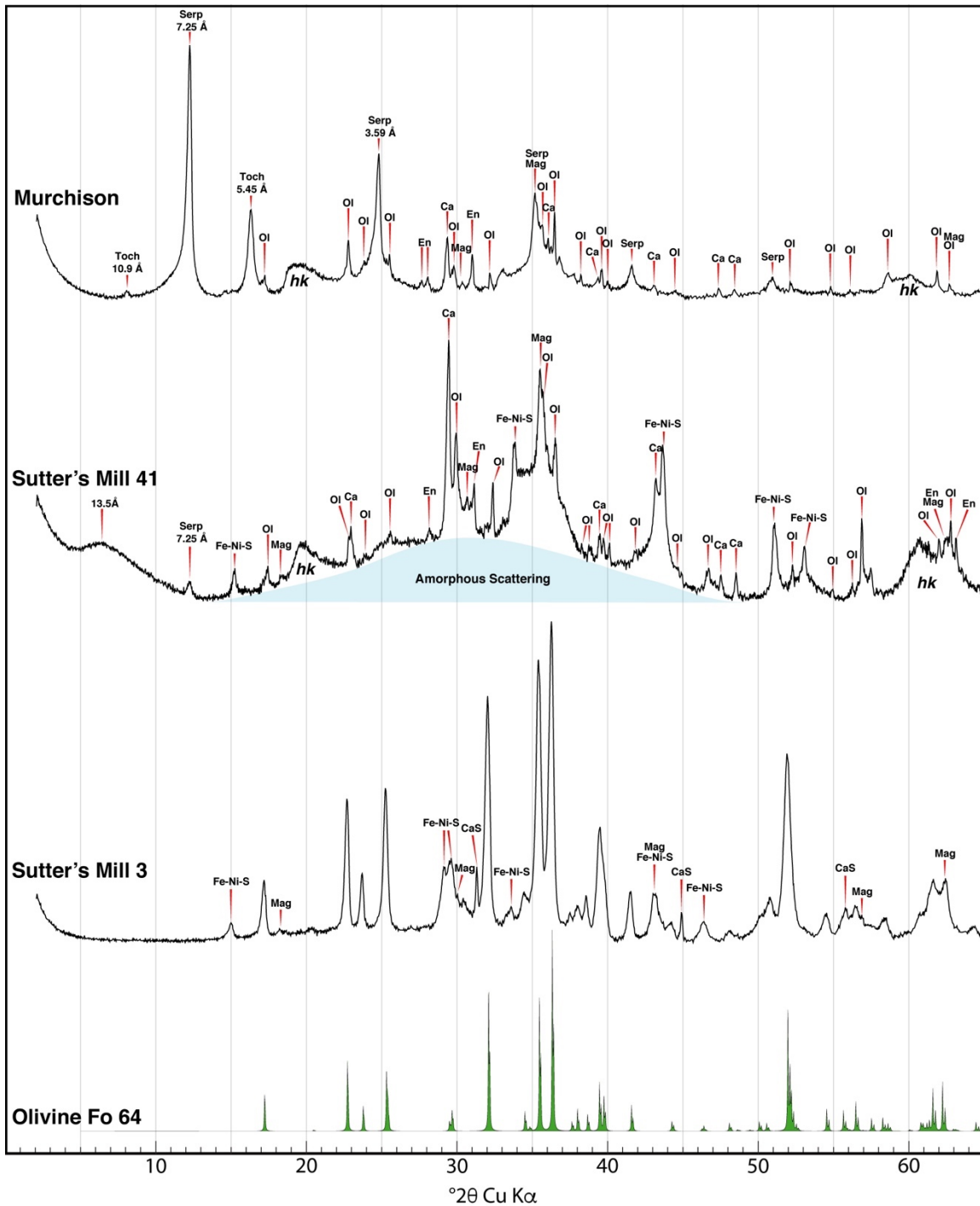
Figure 3.1. Powder XRD profiles for Murchison, SM41, and SM3 in descending order. Labels correspond to the following minerals: Toch=tochilinite, Serp=serpentine, Ol=olivine, En=enstatite, Ca=calcite, Mag=magnetitie, Fe-Ni-S=Fe-Ni sulfides (e.g. troilite, pentlandite, pyrrhotite), CaS=oldhamite. D-spacing is reported for tochilinite and serpentine. **hk** refers to the **hk** bands discussed in text. Olivine Fo 64 pattern is from Wenk et al.,1973 obtained from the ICDD database.

Middle infrared diffuse reflectance data were collected from ~1.8 - 25.0 μm using a Thermo Fisher Nicolet 6700 FTIR with a KBr beamsplitter and a deuterated triglycine sulfate (DTGS) detector. The spectrometer and diffuse reflectance sample chamber were constantly purged with dry (-73 °C dew point) CO_2 scrubbed (< 1 ppm) air. Four samples were examined with this spectrometer: SM3, SM41, Mukundpura, and Murchison. Additional powders of these samples were prepared to <125 μm in a mortar and pestle and kept dry and free of methanol to ensure that absorption bands from organic molecules near ~3.4 μm were not the result of contamination from organic solvents. Powdered samples were heated to 125 °C for 1 hour prior to analysis to remove weakly bound adsorbed H_2O. Higher temperatures were not used because it is unknown at what temperature mineralogical changes begin to occur in carbonaceous chondrites. In the heating experiments of described in Hiroi et al., (1996), the authors note that between the range of unheated and 400 °C the mineralogically important 0.7 μm phyllosilicate band is lost. Additionally, tochilinite is a thermally sensitive mineral with a decomposition temperature near ~245-300 °C, further restricting our pre-heating temperature (Fuchs et al., 1973; Tonui et al., 2014). An aluminum mirror was used to collect background measurements for calculating reflectance, following closely the procedures of Salisbury, (1987). To achieve sufficient signal to noise on these strongly absorbing samples, a "turbo" IR source was employed, and the velocity of the moving mirror was set to 0.1581 cm/sec with an aperture value of 50 (~0.25 cm^2). For each sample, the resulting spectrum was scaled to the reflectance spectrum collected using the ASD at 2.4 μm and joined to generate a diffuse reflectance spectrum from 0.35 - 4.5 μm.

Effects of heating on mineralogy

The primary objective of the OSIRIS-REx mission is to obtain a pristine sample of carbonaceous regolith from asteroid Bennu (Lauretta et al., 2017). Pristine, while

not explicitly defined, likely refers to carbonaceous asteroidal materials that retain their diverse organic compounds and hydrous mineralogy, unmodified by thermal metamorphism. For the purpose of this study the Murchison CM2 chondrite will represent our pristine endmember against which we will compare results for the CM-like Sutter's Mill samples. The Murchison fireball was an observed fall with >100 kg of recovered organic-rich CM meteorite material (Meteoritical Bulletin no. 48). The abundance of sample and presence of extraterrestrial organic compounds have led to this meteorite being one of the most thoroughly studied geologic materials in the Solar System and makes it an excellent benchmark for the CM group. As noted above, Sutter's Mill contains at least two distinct lithologies, phyllosilicate-bearing and olivine-rich, which will be represented by SM41 and SM3, respectively.

Murchison. The powder diffraction profile of Murchison is typified by sharp, intense peaks near 12° and 25° (2θ Cu Kα) and weak, broad peaks near 19° and 61° corresponding, respectively, to *00l* basal reflections and *hk* bands characteristic of the serpentine subgroup of phyllosilicates (Fig 3.1). Very low and moderate intensity reflections near 8° and 16° are due to the presence of tochilinite, a hydrous interstratified alteration product consisting of alternating layers of hydroxide (brucite-like) and iron sulfide (mackinawite-like) minerals. Multiple sharp, low intensity reflections consistent with low-Fe olivine are evident in the diffraction pattern and are likely due to forsteritic chondrule olivine. Additional minor reflections for calcite, magnetite, enstatite and Fe-Ni sulfide are also present. All of these reflections are consistent with the modal mineralogy observed in CM chondrites (Howard et al., 2009).

The reflectance spectrum of Murchison is red sloped with a steep UV drop-off shortward of a visible reflectance peak at 0.59 μm with prominent serpentine bands and a large, broad absorption at 2.8 μm (Fig 3.2). The serpentine bands are fit well (RMS 1.35%) by the MGM with band centers located at 0.72, 0.91, and 1.02 μm. The
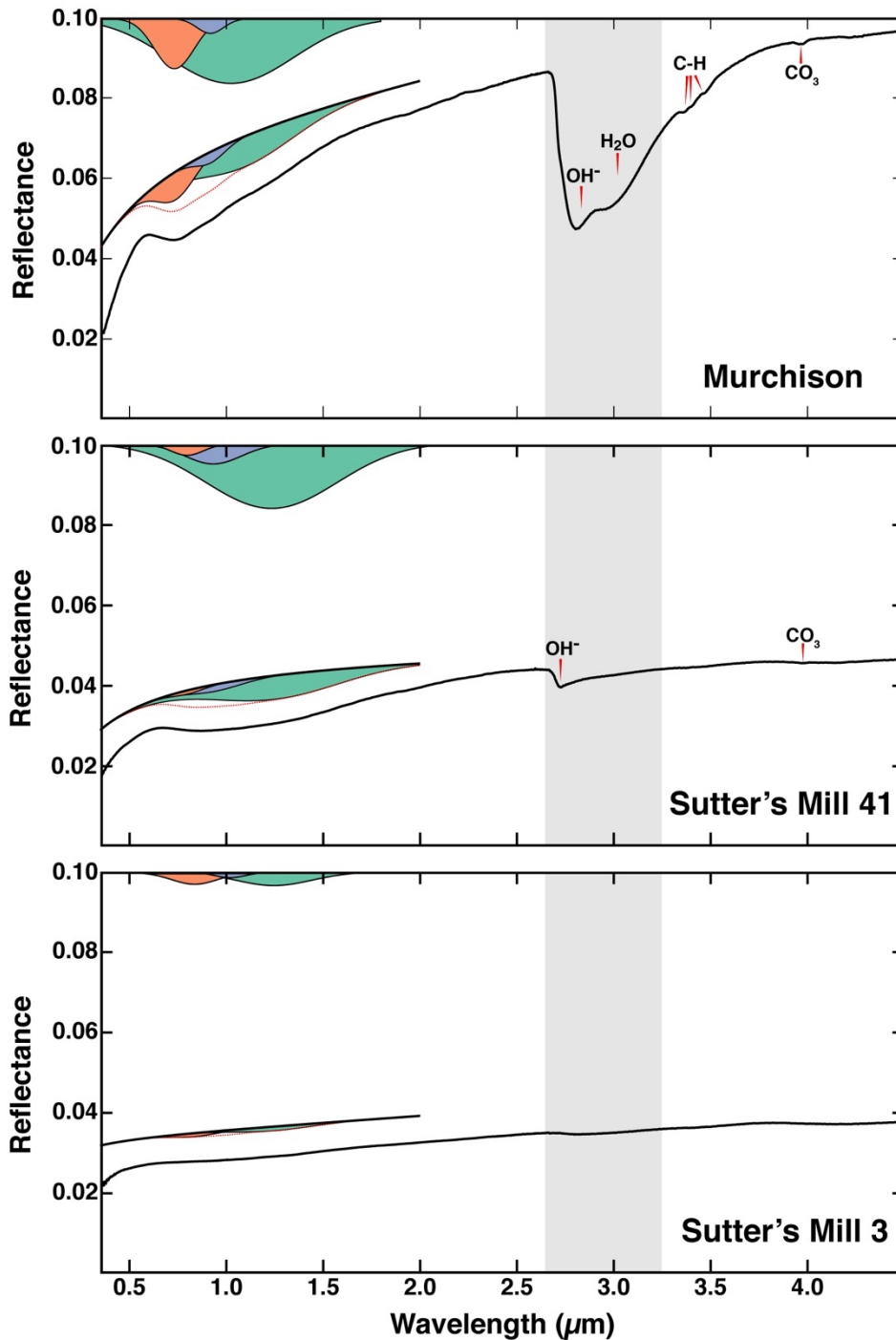
Figure 3.2. Reflectance spectra from Murchison, SM41, and SM3 in descending order. The Gaussian curves in the upper left corner of each subplot depict the relative band intensities of the modeled serpentine bands for each spectrum. Modeled bands convolved with the modeled continuum are offset above each spectrum to show the combined fit of the modeled bands. Absorptions are labeled for hydroxyl (OH), water (H_2O), aliphatics (C-H) and carbonate (CO_3). The grey bar highlights the 3μm region.

modeled positions of the serpentine bands in the CM chondrites analyzed are uniform and consistent with previous spectroscopic investigations of CM chondrites (Fig 3.3; Vilas and Gaffey, 1989, Hiroi et al., 1994 Cloutis, et al., 2011a, 2011b). Variability in the relative band strengths between these samples is minor and restricted to the 0.7 μm Fe^{2+} - Fe^{3+} IVCT absorption and the 1.0 μm CF absorption and likely due to slight changes in oxidation state. The steep UV drop-off and prominent 0.7 μm Fe^{2+} - Fe^{3+} IVCT are consistent with the presence of abundant Fe^{3+}-rich cronstedtite in Murchison (Blazey, 1977; Barber, 1981; Burns, 1993; Cloutis et al., 2008; Howard et al., 2009, 2011). At longer wavelengths, Murchison has a strong absorption with a band minimum of 2.8 μm with a slight shoulder near 2.72 μm likely indicating that both cronstedtite (2.8 μm) and mg-serpentine (2.72 μm) are contributing to this feature, consistent with bulk modal mineralogy determinations showing 50.3 vol. % cronstedtite and 22.2 vol. % Mg-serpentine (Howard et al., 2011; Takir, et al., 2013). Intense absorptions due to the presence of hydrated minerals are consistent with Murchison TGA data that show a mass loss of ~14.5 wt.% upon heating to 1000 °C. The three small absorptions near 3.5 μm, superimposed on the $^-$OH/H_2O absorption, are due to C-H stretching modes owing to the presence of aliphatic organic compounds (Clark et al., 2009; Takir et al., 2013). The weak absorption near 4.0 μm is due to the presence of minor calcite.

Sutter's Mill (SM41). The Sutter's Mill 41 powder diffraction profile shows a weak *00l* basal reflection at 12° and no reflection at 25° indicating that only a minor amount of well crystalline serpentine is present while the existence of broadened *hk* bands near 19° and 61° indicate that extremely fine-grained or highly disordered serpentine is still present. In determining the modal mineralogy of CM chondrites, Howard et al., (2011) use the intense *00l* reflections at 12° and 25° to indicate the presence of Fe-rich serpentine (cronstedtite) and the broadened *hk* bands near 19°

and 61° to indicate the presence of Mg-rich serpentine. The rational for this assignment is based upon numerous TEM studies which show that Fe-rich serpentines exist as larger, more ordered crystals, which provide strong basal reflections, whereas Mg-rich serpentines have few structural layers along [001] (Barber, 1981; Brearly and Jones, 1998; Howard et al., 2009). Using this interpretation, SM41 contains a minor amount of crystalline Fe-rich serpentine (cronstedtite) yet still contains abundant fine-grained Mg-rich serpentine. A broad low-angle reflection near ~7° 2θ and a diffuse intensity distribution centered near ~30° are consistent with the appearance of similar features observed during the thermal transformation of serpentine to form olivine (Brindley and Zussman, 1957; Gualtieri et al., 2009). These investigations propose that the low angle reflection arises due to generation of transitional metastable phases as the structure of serpentine undergoes considerable disruption and re-organization upon dehydration (Brindley and Zussman, 1957). The wide, diffuse intensity distribution spanning ~15-45° is commonly attributed to X-ray amorphous materials such as amorphous silica, volcanic glass and highly disordered minerals (Rowe et al., 2012; Wall et al., 2014; Morris et al., 2015). The profile shows no evidence of the 8° and 16° reflections of tochilinite, however, multiple moderate intensity reflections for Fe-Ni sulfide are present and may represent the breakdown products of tochilinite. Strong reflections for calcite and forsteritic chondrule olivine are present. Minor reflections from enstatite and magnetite are also observed. The mineralogy indicated by XRD can be explained by a moderate amount of heating causing the decomposition of tochilinite, increased disorder in phyllosilicate minerals, and the formation of amorphous materials and metastable phases. The absence of tochilinite indicates a temperature in excess of 250 °C and the presence of calcite indicates that the temperature did not exceed ~600 °C.
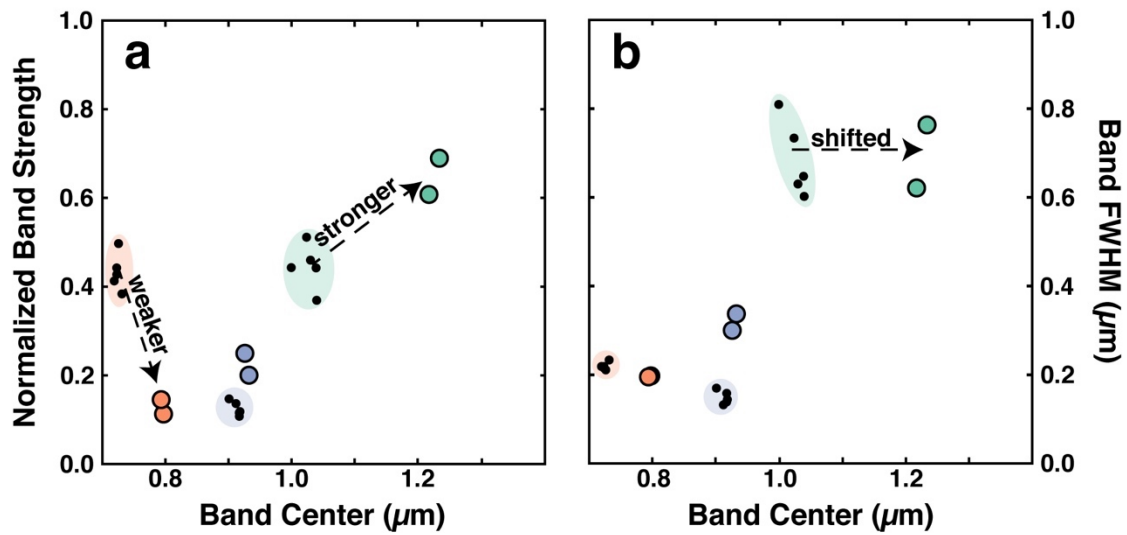
Figure 3.3. Modeled band parameters comparing CM chondrites with phyllosilicate-bearing Sutter's Mill stones. **a)** Normalized band strength vs. band center. **b)** Band width (FWHM) vs. band center. Colors correspond to the Gaussian bands displayed in figure 3.2: red=0.7 μm , blue = 0.9 μm and green = 1.0 μm. Black points in color-shaded ovals are the results for the 5 CM chondrites. Colored points represent SM41 and SM65.

The reflectance spectrum of SM41 is darker and less red-sloped than that of Murchison, exhibiting a gradual UV drop-off occurring shortward of the visible reflectance peak at 0.67 μm. A broad absorption occurs between 0.8 - 1.2 μm and a small but sharp absorption occurs near 2.7 μm. The spectral darkening and reduced slope observed in SM41 can be caused by the heating of organic matter leading to graphitization (French, 1964; Ito et al., 1987; Cloutis et al., 1994). The absence of diagnostic aliphatic C-H bands near 3.4 μm, like those in Murchison, provides additional evidence that graphitization has taken place within SM41, consistent with the results of Pizzarello and Garvie (2014). The starting parameters for the serpentine bands used to fit the CM spectra were used to fit two similar phyllosilicate-bearing SM stones, SM41 and SM65. The band positions, widths and intensities were not constrained and allowed to vary in order to achieve the best fit. In both SM41 and SM65, the intensity of the 0.7 μm Fe^{2+} - Fe^{3+} IVCT absorption is dramatically reduced and the relative strength of the 1.0 μm CF absorption is increased with its band center shifted to 1.2 μm, both tied to changes in oxidation state (Fig 3.3). The wavelength position of CF absorptions are related to the coordination environment of the transition metal causing the absorption. That environment can be modified by changes in valence state (e.g. Fe^{2+} vs. Fe^{3+}), ligand type (e.g. OH^- vs. non-bridging Si-O-), and the interatomic distance between the two (Burns, 1993). In SM41, reduction of ferric iron, dehydroxylation, and increasing disorder in phyllosilicates is likely to significantly modify the coordination environment of Fe resulting in a shifted 1.0 μm band. The intensity of the structural OH feature is diminished and the position of the band minimum is shifted to 2.72 μm. This indicates that a significant amount of hydroxyl has been lost and nearly all of the hydroxyl contributing to the 2.80 μm cronstedtite absorption has been driven off. SM41's TGA profile shows a mass loss of ~9.5 wt.%, 5% less than Murchison. Collectively, the difference in spectral features compared to

the spectrum of CM2 chondrites (weakened UV drop-off, absent 0.7 μm IVCT absorption and a 2.72 μm OH feature) indicate that the Fe^{3+}-bearing cronstedtite mineral has either decomposed or reduced leaving only Mg-rich serpentine.

Sutter's Mill (SM3). The powder diffraction profile for SM3 has a very low background and the majority of the prominent reflections can be attributed to olivine (Fig 3.1). In SM3, the olivine reflections present are consistent with an intermediate composition, but the features are broadened indicating a fine-grained or poorly crystalline intermediate olivine is present (Yoder and Sahama, 1957; Nakamura, 2005). Other features are attributable to minor magnetite, enstatite, oldhamite and Fe-Ni sulfides. The oldhamite present in SM3 has been interpreted to be a product of calcite decomposition in the presence of sulfur at high temperature (>750 °C) under reducing conditions (Haberle and Garvie, 2017). The disappearance of the serpentine pattern and dominance of olivine in SM3 has a remarkable parallel with the powder profiles presented by Brindley and Zussman (1957) showing the thermal transformation of serpentine to form olivine.

The reflectance spectrum of SM3 is nearly flat with a shallow UV drop-off shortward of 0.5 μm and no prominent absorption features. The shallow UV absorption at shorter wavelengths is consistent with the finding that SM3 equilibrated under reducing conditions (Haberle and Garvie, 2017). Modeled band positions in the 1.0 μm region show the presence of very low intensity bands with positions and widths consistent with olivine (Sunshine and Pieters, 1998). The presence of these bands is consistent with the bulk XRD mineralogy but the very low intensities indicate that these features are being suppressed by the presence of fine-grained opaques (Cloutis et al., 1990). A broadened, particularly weak absorption at 2.9 μm is in line with the TGA data indicating ~2.5 wt. % mass loss to 1000 °C (Fig 3.5). Similar to SM41, SM3 shows

no evidence of aliphatic C-H absorptions indicating that the organic compounds have been destroyed though heating.

Identifying dehydrated carbonaceous regolith on asteroid surfaces

In this detailed mineralogical and spectral study, we are able to directly relate mineralogy to spectral signatures through XRD and TGA. However, these spectral interpretations become more difficult when using observations from spacecraft observing natural surfaces. Differences in phase angle (Clark et al., 2002; Bell et al., 2002), grain size distribution (Binzel et al., 2015), temperature (Moroz et al., 2000), and degree of space weathering (Lantz et al., 2018) can impact the reflectance properties of asteroid surfaces imparting spectral slopes, diminishing band intensities and modifying albedo. These factors have little to do with the mineralogical and geochemical properties of the surface yet can greatly impede the extraction of this information from spectral data. In order to mitigate the impact of these non-compositional spectral effects and apply the knowledge gained from this investigation to observations of carbonaceous asteroid surfaces we utilize spectral parameters that minimize the effect of slope (continuum removal) and do not rely upon absolute reflectance values (relative band depth and area).

Heating of CM chondrites leads to diminished UV absorption with the absorption edge occurring at progressively shorter wavelengths, behavior consistent with a reduction of Fe^{3+}. Reducing conditions are also evident in the weakening and disappearance of the 0.7 μm Fe^{2+} - Fe^{3+} IVCT absorption. The combination of these spectral modifications yields a spectrum that is nearly flat and featureless between ~0.4-1.0 μm upon heating to >750 °C. For this reason, a parameter describing the sinuosity of the visible reflectance spectrum is particularly effective at identifying dehydrated CM materials:

$$Sinuosity = \frac{\sum_{i=1}^{n} \sqrt{(X_{i+1} - X_i)^2 + (R_{i+1} - R_i)^2}}{\sqrt{(X_n - X_i)^2 + (R_n - R_i)^2}} \tag{1}$$

47

where, X_i is wavelength (μm) at channel i and R_i is reflectance (scaled 0-100) at channel i. This expression calculates the total length of the spectrum from channel 1 through n then divides by the straight-line length between channels 1 and n. A value of 1 indicates a flat spectrum whereas values > 1 have more curvature (sinuosity). When coupled with the continuum-removed 0.7 μm band depth, discrimination between pristine, moderately heated and highly heated CM materials can be readily made. In the case of the OCAMS MapCam, the continuum-removed 0.7 μm band depth can be calculated from filters v (0.55 μm), w (0.70 μm), and x (0.85 μm):

$$CR_w = \left(\frac{(R_x - R_v)}{(X_x - X_v)}\right) X_w + \left(R_x - X_x \left(\frac{(R_x - R_v)}{(X_x - X_v)}\right)\right) \qquad (2)$$

$$0.7\ \mu m\ depth = \ 100 \left(\frac{CR_w - R_w}{CR_w}\right) \qquad (3)$$

where, CR_w is the continuum reflectance at filter w, R is the reflectance value of the subscripted filter and X is the wavelength position (μm) of the subscripted filter. Both sinuosity and 0.7 μm band depth can be derived from the OVIRS and OCAMS MapCam observations: here we focus our attention on MapCam because of its ability to map these features at higher resolution.

Figure 3.4a depicts the MapCam bandpasses and resampled spectra of Murchison (CM2), Mukundpura (CM2), SM41, and SM3. For both Murchison and Mukundpura a 0.7μm absorption is discernable in the resampled spectra whereas the spectra for SM41 and SM3 do not show this feature. Further, the difference in sinuosity among the four plotted spectra can be observed, with SM3 exhibiting the lowest sinuosity and Mukundpura exhibiting the highest. Using the full dataset (6 CM2 and 16 SM samples), calculated values for sinuosity and 0.7 μm band depth are shown in Figure 3.4b. The horizontal line at y=0 separates spectra with a 0.7 μm absorption
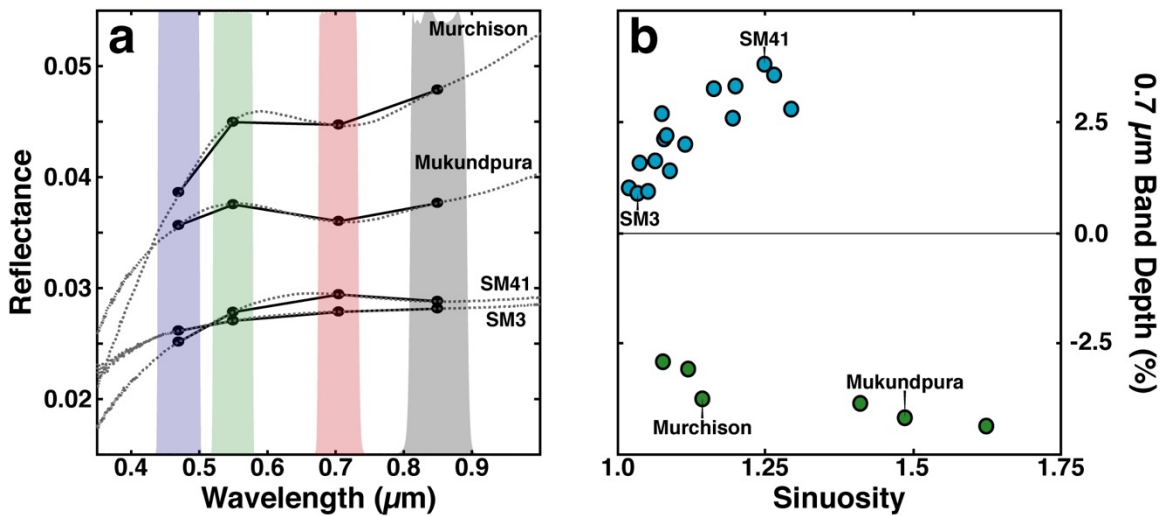
Figure 3.4. **a)** Full resolution spectra for Murchison, Mukundpura, SM41, and SM3 in dashed grey lines overlain by their MapCam resampled 4-point spectra in black. MapCam filter transmission profiles are shown in shaded colors where b-filter=blue, v-filter=green, w-filter=red, and x-filter=grey. **b)** 0.7 μm band depth vs. Sinuosity showing two clear trends for 5 CM chondrites in green and 16 Sutter's Mill stones in blue. The line at y=0 is the dividing line for the presence of either a 0.7μm absorption (negative) or peak (positive). Values of x=1 are flat spectra with sinuosity increasing to the right.
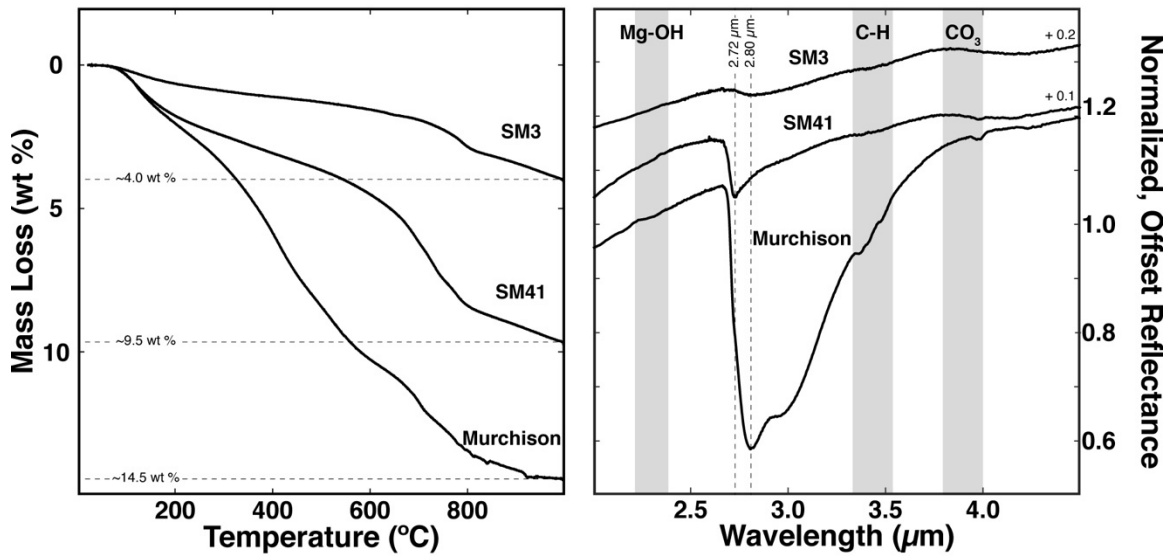
Figure 3.5. TGA mass loss profiles showing the mass losses for SM3, SM41 and Murchison. Dashed lines approximate the total mass loss value for each sample. Right panel shows the normalized and offset 3 μm region with grey bars highlighting the regions of Mg-OH, C-H and CO_3 absorptions. Vertical dashed lines at 2.72 and 2.80 μm indicate where absorption minima for mg-serpentine and cronstedtite are located, respectively. This figure is incomplete. SM41 pattern is actually SM65. They are very similar but not the same.

(negative values) or peak (positive values). Samples that plot to the far left of the diagram are nearly flat with sinuosity increasing to the right. When plotted in this space, the 22 CM-like meteorites observed in this study form two clear trends. The CM chondrites display a positive trend (increasing in the order; Santa Cruz, Cold Bokkeveld, Murchison, Mighei, Mukundpura, Nogoya) where sinuosity is correlated with increasing 0.7 μm band strength. The 16 unique Sutter's Mill samples show a gradational trend, where the phyllosilicate-bearing stones (SM41, SM65, SM12) exhibit moderate sinuosity and a reflectance peak near 0.7 μm, compared to the continuum. The olivine-rich stones (SM3, SM2, SM71) have a minor peak at 0.7 μm and display very low sinuosity. The gradational trend between the hydrated and dehydrated endmembers selected for this study suggest that Sutter's Mill is composed of materials exposed to a range of temperatures from 250-750 °C. This trend also highlights the utility of these two parameters for identifying variably dehydrated CM-like meteorites.

In the reflectance spectra of hydrated carbonaceous meteorites, the integrated intensity of the 3 μm water band is correlated with bulk H content and the minimum position of this feature is used to distinguish between serpentine minerals (Miyamoto and Zolenskey, 1994; Sato et al., 1997; Takir, et al., 2013). To investigate the variability in the 3.0 μm band, a straightline continuum was calculated and removed between reflectance maxima at 2.63-2.65 μm and 3.07-3.85 μm, following the methods of Takir et al., (2013). Observations of band depth relative to the continuum were calculated at 2.72 μm, 2.8 μm, and the maximum band depth position (Table 1). The 3.0 μm integrated intensities of Murchison, SM41, and SM3 show a systematic decrease shown in Figure 3.5. Upon heating to 1000 °C, Murchison exhibits a 14.5 wt. % mass loss and the unheated reflectance spectrum has a 3.0 μm integrated intensity of 0.243 (the unit of integrated intensity is normalized reflectance x μm). SM41 displays a mass loss of ~9.5 wt. % with a substantially lower 3.0 μm integrated

intensity of 0.034. SM3 is the least hydrated sample with ~4.0 wt. % mass loss and a 3.0 μm integrated intensity of 0.014. These three values show an exponential decrease in band strength with decreasing mass loss; in contrast to a linear relationship observed in previous studies of 3.0 μm integrated intensity and H/Si content (Figure 3.5; Miyamoto and Zolensky, 1994). Two possibilities can be considered for this difference: 1) an increase in the abundance of strongly absorbing phases is significantly impacting the apparent band strength (Milliken and Mustard, 2007) and 2) the TGA mass loss data are not representative of OH/H_2O alone and decomposition of organics, carbonates, sulfates, or other phases are significantly contributing to the observed mass loss.

Conclusions

Sutter's Mill is a suite of CM2 meteorites that have been heated to a range of temperatures, altering their mineralogy and VNIR spectral character. The XRD profile of SM41, the least heated Sutter's Mill sample examined here, suggests that it is in the early stages of thermal transformation of serpentine to olivine. The reflectance spectrum of SM41 does not exhibit the characteristic 0.7 μm IVCT band typical of CMs, the UV drop-off is weakened and shifted to shorter wavelengths, and the intensity of the 3.0 μm band is dramatically reduced and centered at 2.72 μm. These spectral attributes collectively indicate that heating of SM41 has caused a reduction of Fe^{3+} and/or a destruction of cronstedtite. The XRD profile of SM3 is dominated by broadened intermediate olivine reflections with a complete disappearance of the serpentine pattern indicating that serpentine that was present has been completely transformed to olivine. The reflectance spectrum of SM3 is nearly flat and featureless with the exception of a UV drop-off short of 0.45 μm. The progressive change in VNIR spectral characteristics, from prominent serpentine and water bands in the Murchison spectrum to the distinct lack of pronounced spectral features in the SM3 reflectance

spectrum, enables the implementation of a parameter describing spectral sinuosity across the visible region of the spectrum. This parameter, coupled with a 0.7 μm IVCT band strength parameter clearly delineates the CM chondrites from the heated Sutter's Mill stones and reveals a gradational trend in the Sutter's Mill suite that is related to the degree of thermal metamorphism. These parameters paired with the observed exponential decrease in the integrated intensity of the 3.0 μm band provide a means to remotely identify dehydrated regolith on carbonaceous asteroids and can help guide the selection of a sample site that contains pristine CM-like materials.

Table 1

Full Range Spectral Parameters

			Murchison	Mukundpura	SM41	SM3
MapCam		Panchromatic	0.045	0.036	0.028	0.027
		b-filter (0.47 µm)	0.038	0.035	0.025	0.026
		v-filter (0.55 µm)	0.044	0.037	0.027	0.027
		w-filter (0.70 µm)	0.044	0.036	0.029	0.027
		x-filter (0.85 µm)	0.047	0.037	0.028	0.028
		0.7 µm depth	-0.037	-0.041	0.001	0.000
		Sinuosity	3.004	1.678	1.733	1.166
Serpentine Bands (MGM)	0.7 µm	Center (µm)	0.729	0.718	0.797	0.701
		Width (µm)	0.229	0.220	0.225	0.308
		Strength	-0.136	-0.093	-0.042	-0.037
	0.9 µm	Center (µm)	0.913	0.901	0.952	0.909
		Width (µm)	0.165	0.169	0.327	0.310
		Strength	-0.040	-0.032	-0.050	-0.034
	1.0 µm	Center (µm)	1.005	0.967	1.230	1.196
		Width (µm)	0.783	0.904	0.776	0.650
		Strength	-0.211	-0.132	-0.190	-0.074
		RMS error (%)	0.14	0.13	0.15	0.17
3.0 µm Band		Band Depth (2.72 µm)	0.236	0.256	0.098	0.006
		Band Depth (2.80 µm)	0.455	0.256	0.075	0.021
		Band Depth (Max)	0.459	0.267	0.103	0.024
		Position of Max Depth	2.807	2.765	2.727	2.910
		Band Depth Ratio (2.72/2.80)	0.52	1.00	1.31	0.29
		Area	0.243	0.116	0.034	0.014

54

CHAPTER 4

Chemical, Mineralogical and Spectral Variability of Intra-Plate Igneous

Suites: The Snake River Plain

Introduction

Over the past two decades orbital, surface and meteoritic investigations of Mars have revealed that the composition of volcanic rocks exposed at the surface, though dominantly basaltic, display greater diversity than previously realized (Mustard and Sunshine, 1995; Christensen et al., 2005; McSween et al., 2006; Nekvasil et al., 2009; Rogers and Nekvasil, 2015; Santos et al., 2015; Sautter et al., 2015; Morris et al., 2016). Many of these studies indicate that Mars exhibits numerous occurrences of volcanic rocks with alkalic compositions (McSween et al., 2006; Nekvasil et al., 2009; Santos et al., 2015). The distinction between alkalic and subalkalic is made on the basis of chemistry where alkalic compositions are enriched in Na_2O and K_2O (Irvine and Baragar, 1971; Le Maitre et al., 2005). On Earth, volcanic rocks with alkalic composition can give insight into their mantle source region and the secondary processes that acted upon them during their ascent to the surface (Wilson, 1989; Nekvasil et al., 2004)

Greater than 90% of Earth's volcanic activity occurs at the convergent and divergent margins marking the boundaries of the lithospheric plates (Wilson, 1989). As such, the processes that generate melt at these regions and the melts themselves are unique to Earth. More appropriate analogs for the volcanic products generated on Mars are found at Earth's intra-plate volcanic centers. One such intra-plate volcanic center is the continental tholeiitic suite of the eastern Snake River Plain (Stout and Nicholls, 1977; Kuntz et al., 1982; Nekvasil, 2000; Whitaker et al., 2007). Southern Idaho is marked by the track of the Yellowstone hot-spot, bordered to the north by the Idaho batholith and to the south by fault bound ranges. This prominent topographic

depression spans the width of the state and is host to the Snake River Plain (SRP) (Pierce and Morgan, 1992; Smith and Braile, 1994). The eastern portion of the SRP is host to extensive volcanism typified by a bi-modal distribution of tholeiitic basalt and potassic rhyolite (Spear, 1979; Pierce and Morgan, 1992; Nekvasil et al., 2000; McCurry et al. 2008). Volcanic products compositionally intermediate to these are rare but occur within the Craters of the Moon National Monument (COTM). The volcanic pile at COTM consists of a suite of lava flows spanning a compositional range from ferrobasalt – basaltic trachyandesite – trachyandesite - trachyte (Leeman et al., 1976; Kuntz et al., 1982; Kuntz et al., 1992; Stout et al., 1994; Putirka et al., 2009). These various rock types represent derivative liquids of a parental magma evolved to varying degrees through crystal fractionation and assimilation (Putirka et al., 2009).

Volcanism on the SRP has extensive heritage as a planetary analog (Greeley and King, 1977). The SRP is the type locality for basaltic plains-style volcanism; essentially a morphology intermediate to the large shields of Hawaii and the extensive flood basalts of the Columbia river (Greeley, 1982; Hughes et al., 1999). Numerous morphological studies indicate that plains-style volcanism has occurred on Mars (Plescia, 1981; Hauber et al., 2009; Henderson et al., 2015). In addition to morphological similarities, the SRP is thought to represent a compositional analog to Martian volcanics with the intermediate rocks of COTM bearing chemical similarities to volcanic rocks in Gusev crater as well as individual clasts in Martian meteorite NWA 7034 (Usui et al., 2008; Adcock et al. 2018).

In this study we examine a suite of petrogenetically related volcanic rocks from the SRP using lab-based spectroscopic techniques relevant to remote sensing investigations of Mars. Emphasis is placed on identifying trends in spectral features that are correlated to the well characterized trends in major element chemistry that exist in these igneous suites.

Methods

The samples examined in this study were collected with the intent of sampling the broad chemical diversity observed within the young lava flows of the Eastern Snake River plain. Care was taken to collect minimally altered samples from below the upper glassy margin of each lava flow, where possible. Sample WA003 is the only sample from outside of COTM and was collected from the summit region of Wapi, a large tholeiitic basalt shield erupted approximately coeval with the COTM eruptive phase A volcanic rocks (Kuntz et al., 1982). Each sample was cut, crushed, pulverized and sieved so that the products available for study were; one thin section, one ~5-10 cm hand sample, >1000 μm chips, and 1000-500 μm, <500 μm, and <61 μm size fraction separates. For each sample, major and trace elements were analyzed by X-ray fluorescence (XRF) at the Washington State University GeoAnalytical Laboratory (Johnson et al., 1999).

A split of bulk rock chips from each sample was pulverized using a tungsten carbide ring and puck mill. A spilt of this pulverized material was then hand ground with an agate mortar and pestle and prepared for XRD analysis. The powder mount was prepared following closely the methods of USGS open file report 01-041. X-ray diffraction (XRD) profiles were collected over a 2θ Cu Kα range of 2° to 65° at a step width of 0.02° using a Rigaku MiniFlex600 diffractometer at Arizona State University.

Sample crystallinity was determined from powder diffraction profiles (10° to 50° 2θ Cu Kα) using the MDI JADE 8 software. For each profile, a 35-pt Savitzky-Golay smoothing filter was applied and integrated counts above cubic and linear backgrounds were recorded. The ratio of integrated counts above a cubic background to integrated counts above a linear background represents the relative crystallinity (RC; Wall et al., 2014). Using the empirical calibration of Wall et al., (2014) values of RC were converted to values of calibrated crystallinity through:

$$C(\%) = -\sqrt{\frac{-RC(\%)}{0.003} + 42500} + 198$$

A JEOL JXA-8530F Electron Probe Microanalyzer (EPMA) located at Arizona State University's LeRoy Eyring Center for Solid State Science (LE-CSSS) was used to determine the major element composition of feldspar, olivine, pyroxene and oxides through wavelength dispersive spectroscopy (WDS). The analytical conditions for WDS were 15 keV accelerating voltage, 15 nA beam current with a beam diameter of 1 μm. For analysis of feldspar minerals, a broadened beam diameter of 5 μm was used to avoid loss of Na. Synthetic and natural standards were used for calibration. EPMA was also used to collect backscatter electron (BSE) images and elemental maps via energy dispersive spectroscopy (EDS).

Visible to near infrared (VNIR; 0.35–2.5 μm) reflectance spectroscopy was performed on <61 μm powders of each sample. Spectra were acquired at room temperature and ambient atmosphere at Arizona State University's S.C.O.R.P.I.U.N. lab using a FieldSpec 3 spectroradiometer (Analytical Spectral Devices, Inc.; ASD). For each observation, a goniometer with mounted fiber optic cable and external 50 W quartz-tungsten-halogen light source was configured with an observation geometry of 30° incidence and 0° emergence. Observations of a Spectralon® 20% diffuse reflectance standard were used as a calibrated reference. This reflectance standard was selected because its reflectance is similar to the samples being analyzed. In addition, the 20% target exhibits a smooth spectrum with a slightly red slope and does not contain distinct spectral features like the 99% Spectralon® target. The ASD ViewSpec software was employed to process the spectral data to units of absolute reflectance. Each spectrum collected consists of 100 co-added scans. For each sample examined, 10 spectra were collected in order to determine and monitor instrumental

noise and observational errors. The final spectrum for each sample is an average of 1000 scans.

The modified Gaussian model was employed to examine the nature of the electronic absorption bands expressed in each spectrum (Sunshine et al., 1990). A three-component continuum was used to approximate the spectral continuum within the MGM (Hiroi et al. 2000; Noble et al. 2006). Starting conditions for each spectrum were based upon previously determined parameters for olivine and pyroxene and modified to compensate for the presence of ilmenite in some samples (Sunshine and Pieters, 1998; Sunshine and Pieters, 1993; Klima et al., 2011). The threshold to end the root mean square (RMS) minimization was determined from the 1σ variance of the ten spectra collected from each sample.

Whole-rock thermal infrared (TIR) emission spectra (2000–200 cm^{-1}; 5–50 µm) were acquired at Arizona State University's Mars Space Flight Facility using a ThermoFisher nicolet 670 Fourier transform infrared spectrometer (FTIR) modified to measure emitted radiance (Ruff et al., 1997). Samples were placed in an oven and heated to 80 °C for >12 hours prior to measurement and a sample stage heater was employed to keep the sample heated to ~80 °C throughout the measurement. The 1000-500 µm size fraction sample was used for this measurement. Observations of warm (70 °C) and hot (100 °C) blackbodies were used to calculate the instrument response function and determine calibrated sample radiance that was then converted to emissivity. To determine mineralogy from the emissivity spectrum a modified non-negative linear least squares algorithm and a library of spectra representing common primary igneous phases were used (Ramsey and Christensen, 1998; Christensen et al., 2000; Rogers and Aharonson, 2008). Minerals modeled to the sample spectrum are reported as grouped abundances where the groups consist of feldspar, glass, olivine, clinopyroxene, orthopyroxene, apatite, and Fe-Ti-Cr oxides. While constructing

59

Table 1

Snake River Plain Igneous Spectral library

Feldspar	Olivine	Pyroxene		Glass	Oxides	Other
Anorthite (BUR-340)	Forsterite (BUR-3720A)	Diopside (BUR-1820)	Enstatite (DSM-ENS01)	Andesite Interstital (MEM-5)	Magnetite (WAR-0384)	Apatite (P1)
Bytownite (WAR-1384)	Forsterite (AZ-01)	Diopside (WAR-6474)	Enstatite (NMNH-38833)	Dacite Interstitial (MEM-4)	Titanomagnetite	Quartz (BUR-4120)
Labradorite (WAR-4524)	Fo 10 (KI 3008)	Diopside (NMNH-107497)	Enstatite (NMNH-R14440)	Synthetic K-rich	Ilmenite (WAR-4119)	
Labradorite (BUR-3080A)	Fo18 (KI 3354)	Diopside (NMNH-80819)	Enstatite (NMNH-34669)	North Crater Float (COTM019)		
Andesine (BUR-240)	Fo 25 (KI 3352)	Diopside (R15161)	Enstatite (NMNH-82436)			
Andesine (WAR-0024)	Fo 35 (3373)	Diopside (R17421)	Bronzite (BUR-1920)			
Oligoclase (WAR-0234)	Fo39 (KI 4143)	Diopside (WAR-5780)	Bronzite (NMNH-119793)			
Oligoclase (BUR-3680)	Fo54 (KI 3372)	Diopside (WAR-6454)	Bronzite (NMNH-C2368)			
Oligoclase (BUR-060)	Fo 60 (KI 3362)	Augite (BUR-620)	Bronzite (93527)			
Oligoclase (WAR-5804)	Fo65 (KI 3115)	Augite (NMNH-119793)				
Albite (WAR-0244)	Fayalite (WAR-RGFAY01)	Augite (DSM-AUG01)				
Albite (WAR-0612)		Jadeite (WAR-9909)				
Albite (WAR-0235)		Hedenbergite (NMNH-16168)				
Mircocline (BUR-3460)		Hedenburgite (DSM-HED01)				
Mircocline (3460A)		Hedenburgite (NMNH-R11524)				

Source data: Christensen et al., (2000); Wyatt et al., (2001); Hamilton, (2000); Koeppen and Hamilton, (2008); Hamilton (2010);

the library, emphasis was placed on selecting high-quality, well characterized spectra that span a broad compositional range in order to allow for the estimation of mineral compositions (Table 1: Ruff, 1998; Hamilton, 2010; Hamilton and Ruff, 2012). Estimates of mineral composition are made by calculating the weighted average of the modeled mineral components (e.g. weighted average of Fo# for olivine and anorthite (An), albite (Ab), orthoclase (Or) values for feldspar). In the event where one library spectrum is included in the model, the composition of that library spectrum is reported. Compositions are only estimated for minerals whose abundance is above the 5 vol % detection limits (Feeley and Christensen, 1999). Individual mineral spectra whose modeled error is greater than half of their abundance are excluded from compositional calculations.

The weighted absorption center of the main reststrahlen Si-O stretching band (700 – 1400 cm^{-1}) is calculated by identifying the edges of the absorption, integrating the spectral area across this region, and locating the wavenumber position where the cumulative integrated area is equal to half of the total integrated area. The absorptions edges are generally located at ~1200-1400 cm^{-1} (the Christiansen frequency) and ~790-820 cm^{-1}.

Results

Hand sample and Thin Section petrography.

Olivine tholeiite. The most primitive member of this suite is WA-003, a sample of olivine tholeiite from the Holocene aged Wapi shield volcano. In hand sample, WA-003 is minimally weathered vesicular basalt with visible grains of plagioclase and olivine. Some vesicles are stained red with oxide alteration. In thin section, the texture of WA-003 varies across section from intersertal to intergranular to glomeroporphyritic with large laths of randomly oriented plagioclase as the dominant phase with subordinate anhedral olivine and pyroxene. Spinel occurs as

dispersed acicular ilmenite, anhedral grains composed of titanomagnetite-ilmenite exsolution lamellae and small symplectite textured spinel in dispersed pockets of glass.

Ferrobasalt. Samples COTM-016 (Broken Top), COTM-012 (North Crater), and COTM-017 (Blue Dragon) have similar chemical, mineralogical and petrographic properties and as such will be grouped for descriptive purposes. These flows are extensive surface and tube-fed pahoehoe flows. In hand sample, the ferrobasalts are vesicular and aphanitic with a dark cobalt blue hue. Flows will often have a thin bright blue secondary coating on their glassy exterior which inspired the naming of the Blue Dragon flow. In thin section, the microscopic texture of these samples is hyalopilitic with rare large phenocrysts. Microphenocrysts are set in an opaque glassy groundmass and are dominated by subparallel, euhedral plagioclase laths with lesser amounts of euhedral olivine and titanomagnetite clusters. At the micron scale, the glassy groundmass is composed of microlites of skeletal olivine exhibiting dendritic chain-and-lantern morphology, feathery and cruciform Fe-Ti oxide, and acicular euhedral crystals of apatite. Olivine microphenocrysts commonly have inclusions of Fe-Ti oxide and/or apatite.

Basaltic trachyandesite. COTM-014 (Campground) is a slabby surface fed pahoehoe flow outcropping near the COTM information center and campground. In hand sample it is dark, aphanitic and vesicular with minimal evidence for weathering. In thin section the texture is intersertal to hyalopilitic. Large phenocrysts are rare and are always euhedral feldspar. Microphenocrysts are dominantly euhedral plagioclase laths with subordinate euhedral olivine and titanomagnetite clusters. Groundmass is translucent brown composed almost entirely of glass.

Trachyandesite. COTM-015 (Devil's Orchard) is an 'A'a flow and as such the hand sample texture varies between more massive interior and rugged vesicular exterior. The color of the fresh interior section is distinctly brown compared to the

previously described samples. In thin section, Devil's Orchard exhibits hyalopilitic texture with occasional trachytic texture. No large phenocrysts are present although rare deteriorated xenocrysts of anorthoclase occurs. Microphenocrysts of euhedral subparallel feldspar are abundant as well as numerous cluster of micron-sized titanomagnetite. Microphenocrysts of euhedral olivine and tabular clinopyroxene are minor. The groundmass is dominated by light brown translucent glass.

Trachyte. COTM-009 (Serrate) and COTM-013 (Highway) are jagged 'A'a to block flows with thick flow fronts and extremely rugged surfaces. In hand sample COTM-009 resembles COTM-015 but is less massive and more vesicular overall. COTM-013 is a massive piece collected on the western flow front where access to interior blocks was straightforward. In thin section these flows exhibit hyalopilitic to trachytic texture. Large deteriorated xenocrysts of anorthoclase with well-defined reaction rims are common in both samples. Occasional tabular phenocrysts of clinopyroxene are present in both samples though olivine appears to be absent. Microphenocrysts are dominated by euhedral feldspar with small evenly dispersed grains of titanomagnetite. The matrix consists of abundant turbid to translucent light brown glass. Small, unidentifiable minerals with high birefringence are occasionally observed set in the glass.

Elemental Analysis. SRP volcanic rocks belong to the potassic silica-saturated alkalic series (Whitaker et al., 2007). This series is found exclusively in continental regimes and is commonly associated with olivine tholeiites, representing the least-evolved member of the series (Nekvasil et al., 2000). Beginning with the tholeiitic composition (Wapi), the series displays strong enrichment in alkalis ($Na_2O + K_2O$) with a slight increase in silica moving from the basalt to the trachybasalt class (Fig 4.1a). This initial alkali enrichment causes the composition to cross the boundary separating the sub-alkalic and alkalic fields (shown as a dashed line in figure 4.1a). The three
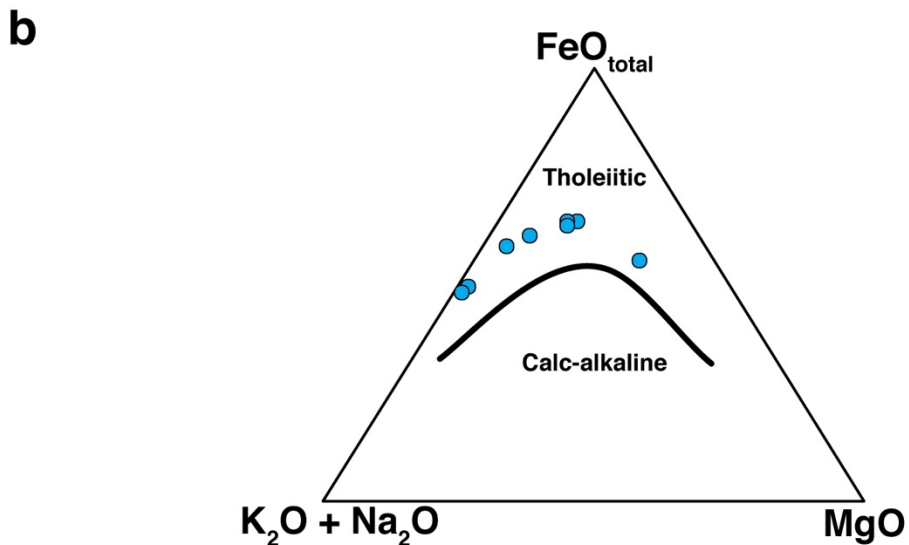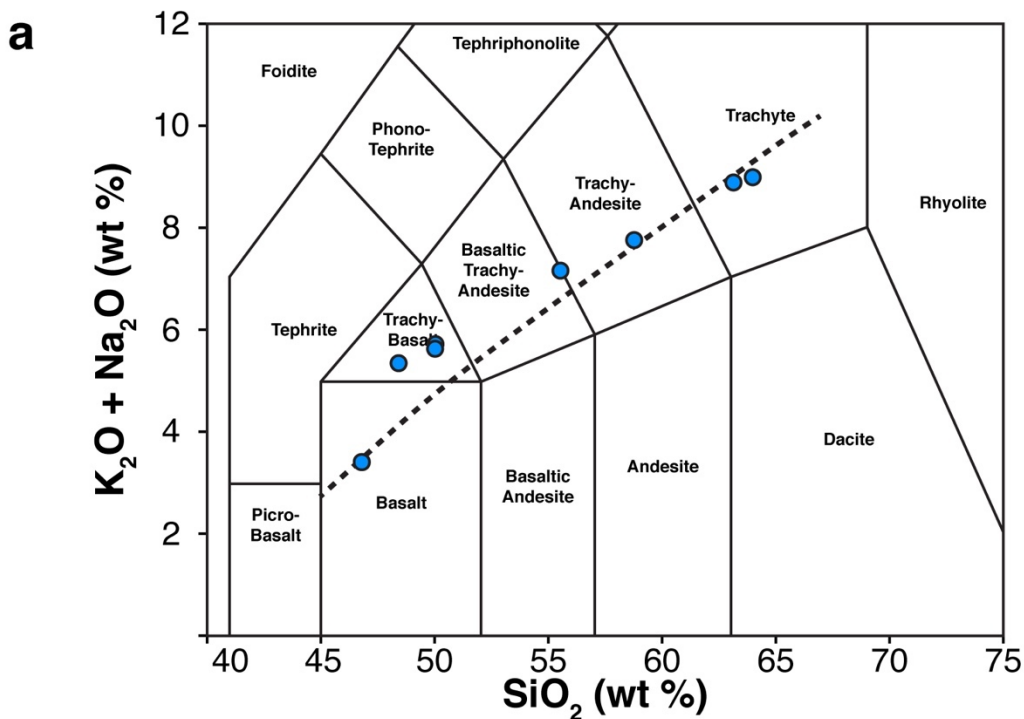
Figure 4.1. **a)** Total Alkalis vs. Silica (LeBas et al. 1985) diagram showing the COTM suite as blue dots. Dashed line shows the separation between the subalkalic and alkalic fields (Irvine and Baragar, 1971). **b)** Alkali-Iron-Magnesium (AFM) plot showing the Fe-enrichment trend of the COTM suite. Black line denotes a separation between calc-alkaline trends (below line) and tholeiitic trends (above line).

ferrobasalt samples examined in this study (Broken Top, North Crater, and Blue Dragon) fall in this trachybasaltic class (Le Bas et al., 1985). Members of this differentiation series can show initial enrichment in alkalis accompanied by a depletion in silica moving into the tephrite class, similar to the Martian composition Wishstone (McSween et al., 2006), though that behavior is not observed in this sample suite (Whitaker et al., 2007). With continued evolution this series sees a modest increase in alkalis with strong enrichment in silica nearly following the Irvine and Baragar (I&B) boundary through the basaltic-trachyandesite (Campground) and trachyandesite (Devil's Orchard) classes. The final samples in the series are the trachyte class rocks Serrate and Highway that are strongly enriched in K_2O and fall below the I&B boundary in the subalkalic field (Fig 4.1a; Table 4.2).

When plotted on an alkali-iron-magnesium (AFM) diagram, these samples show a tholeiitic differentiation trend (Fig 4.1b). Starting with a tholeiitic composition with low alkali and near equal proportions of iron and magnesium the trend shows an enrichment in Fe resulting in the ferrobasalts (Fig. 4.1b). Titanium parallels the Fe-enrichment trend with a peak value of 3.2 wt.% in Broken Top (Table 2). At this point Fe-enrichment ends with the onset of Fe-Ti oxide crystallization and the residual liquids are progressively enriched in alkalis resulting in the remaining members of the series.

Microprobe Major Phase analyses.

Feldspar*.* Feldspar is the most abundant mineral in each of the samples examined in this study. With increasing degree of evolution, the feldspar population exhibits a compositional change that follows the trend observed in the total alkali versus silica diagram (Fig 4.1). The feldspar minerals within the Wapi olivine tholeiite are the least evolved and lie in the labradorite compositional field (Fig 4.2). The ferrobasalts contain the more sodic andesine feldspar and show a slight increase in their potassic component (Or). Feldspars within the Campground basaltic-

65
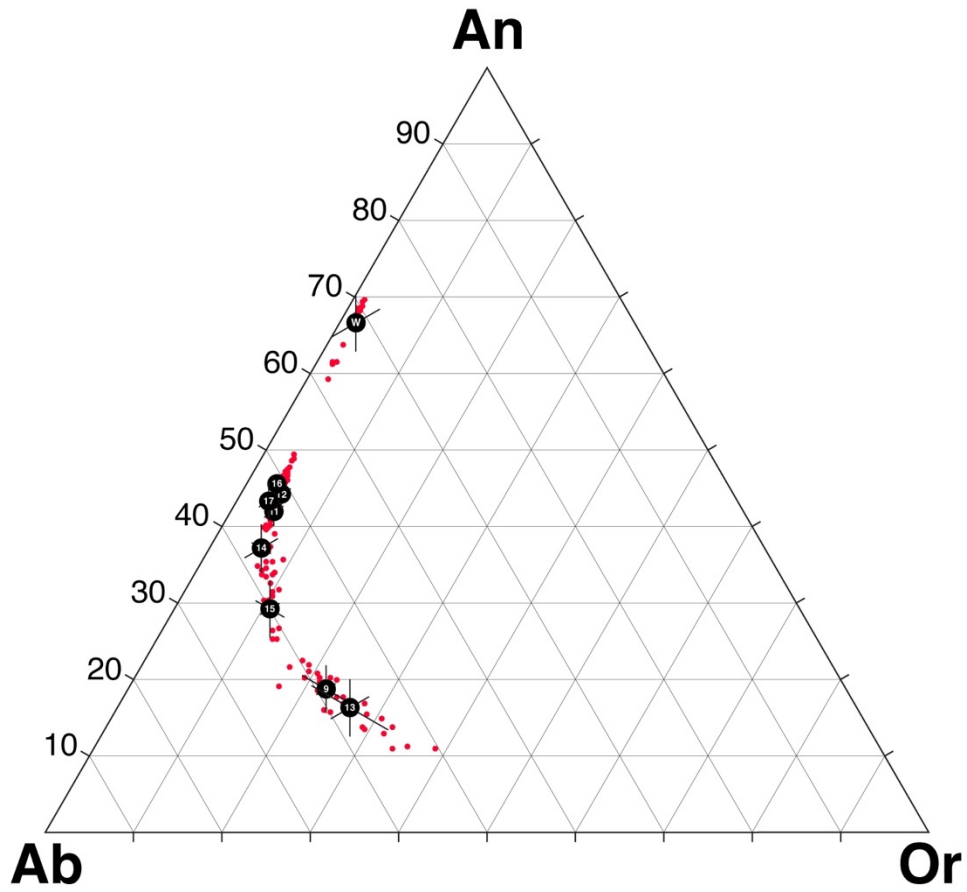
Figure 4.2. Feldspar compositions determined from EPMA. Red dots are individual analyses and black numbered dots correspond to average values for the samples examined in this study.
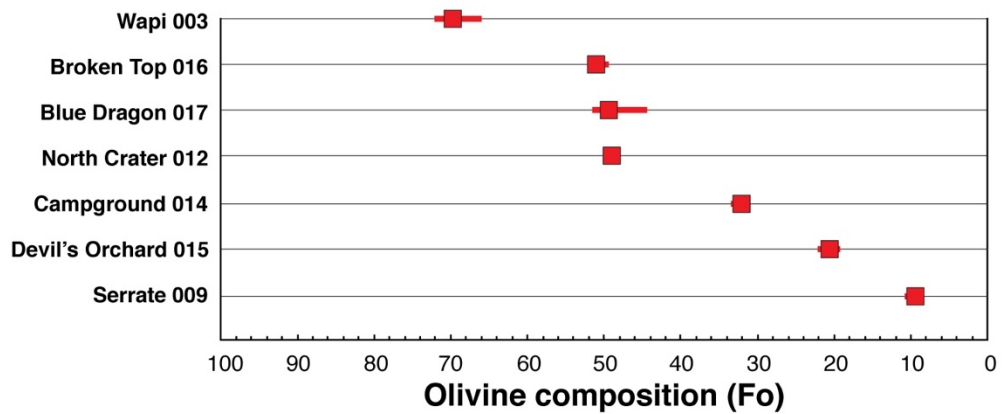
Figure 4.3. Olivine compositions determined from EPMA from samples with identifiable olivine. Sample COTM013 Highway did to contain olivine.

trachyandesite are also andesine composition with a slight increase in their albite (Ab) and Or components. The Devil's Orchard trachyandesite contains feldspars of oligoclase composition. With increasing evolution, the feldspar compositions of the trachytes become highly ternary. This compositional trend is very similar to that observed by Nekvasil et al., (2000) and is a clear indicator of magmatic evolution.

   Olivine. Olivine is the dominant ferromagnesian phase present in all members of this suite except the Highway trachyte. In the most primitive member of the suite, Wapi, olivine is fairly Mg-rich with a forsterite content (fo#) of 69 ± 2.5 (Fig 4.3). With increasing degree of evolution, the fo# of olivine progressively decreases with values of ~50 for the ferrobasalts, 32 for the basaltic trachyte, 21 for the trachyandesite and 10 for the Serrate trachyte. The Highway trachyte contained no observable olivine in the section examined. The gradation observed in the composition of olivine tracks the coupled Fe-enrichment and Mg-depletion trends observed within this series, resulting in increasingly Fe-rich olivine that approaches a fayalitic composition.

   Pyroxene. Pyroxene compositions are similarly Fe-rich with Fe-rich augite that approaches a hedenbergite composition with increasing evolution. The first member of the series possessing pyroxene is the Devil's Orchard trachyandesite with a ternary composition of $Wo_{40}En_{22}Fs_{37}$, followed by the Serrate trachyte $Wo_{40}En_{12}Fs_{46}$, and the Highway trachyte with $Wo_{41}En_8Fs_{51}$.

   VNIR MGM analysis. Spectral analysis of the VNIR reflectance spectra reveals four distinct groups with the following mineral signatures; ilmenite+olivine+Ca-pyroxene, ilmenite+olivine, olivine+Ca-pyroxene, Ca-pyroxene. Reasonable fits for the Wapi olivine tholeiite and ferrobasalts are only produced when a very broad absorption band centered near 1600 nm and a band near 600 nm are included in the starting parameters to account for ilmenite absorption features (Table 3). In Wapi, the ilmenite bands are located at 670 and 1650 nm, the latter of which has a full width at

half maximum (FWHM) of 1200 nm. Also present are three bands located near 920, 1030, and 1350 nm consistent with the presence of olivine (Sunshine and Pieters, 1998). However, the position of the 1350 nm band is slightly longer and the intensity of the 1030 band is slightly stronger than expected for olivine. This can be explained by the presence of overlapping bands attributable to augite. A broad absorption at 2300 nm indicates the presence of a high-Ca pyroxene which has additional bands near 1050 and 1200 nm all of which are observed in the spectrum of Wapi. Although they are present, the absorption bands attributable to pyroxene and olivine are weak likely due to the presence of opaque minerals (ilmenite and magnetite) which act to decrease overall reflectance and mafic silicate band intensities (Cloutis et al., 1998).

Ilmenite provides a stronger contribution to the reflectance spectra of the ferrobasalts and each spectrum exhibits bands near 600 and 1600 nm which dominate the spectrum and effectively mask the absorption features near 1000 nm (Table 3). Extremely weak bands consistent with olivine are fit near 900, 1070, and 1320 nm. No other absorption features are apparent.

The Campground basaltic-trachyandesite, Devil's Orchard trachyandesite and Serrate trachyte each exhibit absorptions attributable to the presence of both olivine and high-Ca pyroxene. Absorptions near 900, 1030, and 1320 nm are consistent with the presence of olivine (Table 4). High-Ca pyroxene contributes slightly overlapping but distinguishable bands near 1010, 1150, and 2050 nm. No apparent contribution from opaque minerals is present and the bands observed in these samples are easily identifiable and significantly stronger.

The Highway trachyte is well fit using only the bands attributable to High-Ca pyroxene. These bands are located near 1020, 1170, and 2300 nm (Table 4). The Highway flow also exhibits a small 1900 nm absorption due to the presence of H_2O. It is not clear which phase this is associated with.
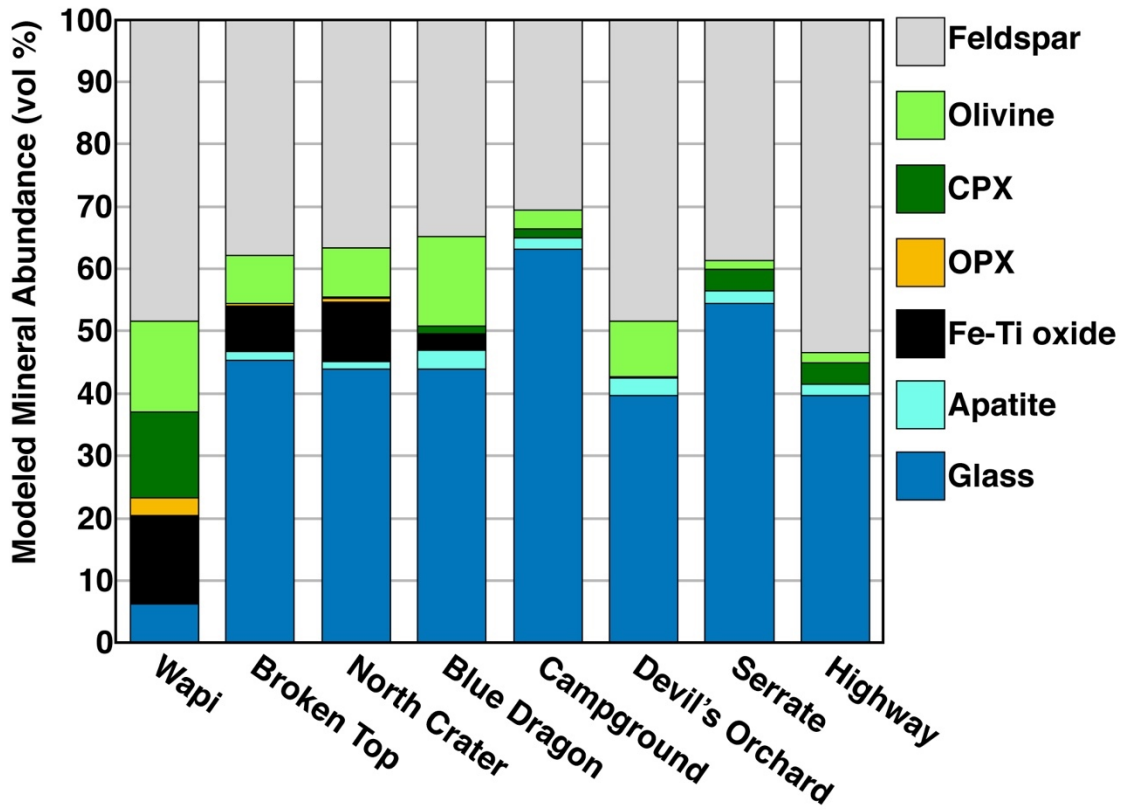
Figure 4.4. TIR modeled mineralogy for the COTM suite.

TIR modal mineralogy. Linear least squares modelling of the infrared emission spectrum of Wapi (Fig 4.4) indicates a mineralogy dominated by feldspar (48 vol %) with approximately equal proportions of olivine (14 vol %) and high-Ca pyroxene (14 vol %), abundant Fe-Ti -Cr oxide (14 vol %), glass (6 vol %) and minor orthopyroxene (3 vol %). Based on petrographic and microprobe observations, the minor orthopyroxene modeled is likely not a real component of the sample and its abundance is below the ~5% detection limit for thermal emission spectroscopy (Feeley and Christensen, 1999).

Modeling of the Ferrobasalts (Broken Top, North Crater, and Blue Dragon) indicates a similar modal mineralogy dominated by glass (~45 vol %) and feldspar (~35 vol %) with lesser olivine (8-14 vol %) and Fe-Ti-Cr oxides (3-9 vol %). Apatite is modeled as a minor phase (1-3 vol %) below the detection limit, though its spectrum has a characteristic absorption feature near ~600 cm^{-1} which may allow it to be detected at relatively low abundances. Petrographic and microprobe observations indicate that apatite is abundant in the microlite-rich ground mass and occasionally as inclusions in olivine microphenocrysts.

The model results of the Campground basaltic-trachyandesite, Devil's Orchard trachyandesite, and the Serrate and Highway trachytes are similar with slight variations. As a group these samples show modal mineralogies consisting mostly of glass (39-63 vol %) and feldspar (30-53 vol %) with minor olivine (3-9 vol %), high-Ca pyroxene (2-3 vol %) and apatite (2-3 vol %). No Fe-Ti-Cr oxides were included in the model solutions. Consistent with petrographic observations, the modal mineralogy of Campground consists mostly of glass (63 vol %) and represents the glassiest sample in the suite.
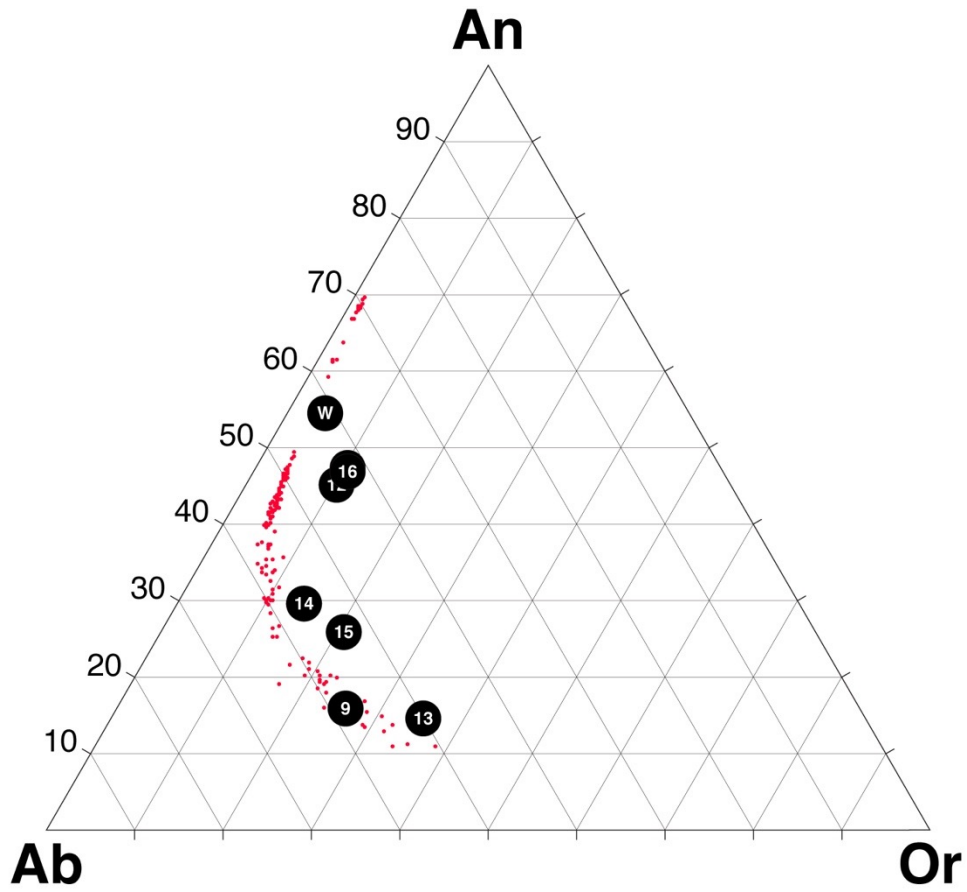
Figure 4.5. Mineral compositions derived from thermal infrared spectra in black. Red dots correspond to the EPMA measured values.

TIR mineral compositions.

Feldspar. The Wapi olivine tholeiite is best fit by a combination of two feldspars; labradorite (29 ± 5 vol %) and bytownite (18 ± 3 vol %). The weighted average composition is $An_{54}Ab_{41}Or_5$ which falls in the labradorite field. Microprobe data from feldspar within Wapi are more calcic ($An_{64-70}Ab_{29-35}Or_1$) than this modeled composition though both plot within the labradorite field (Fig. 4.5).

The modeled fit of the Broken top spectrum includes bytownite (18 ± 4 vol %) and anorthoclase (10 ± 2 vol %) with a weighted average composition of $An_{47}Ab_{42}Or_{11}$. The 1σ range of microprobe feldspar compositions in Broken Top is $An_{46-48}Ab_{49-51}Or_{3-4}$ and falls within the andesine compositional field. The model derived composition of Broken Top is more potassic than measured though the An and Ab compositions are similar to the measured values.

The feldspar component of North Crater is modeled as a mixture of anorthoclase (11 ± 2 vol %), labradorite (11 ± 5 vol %), and bytownite (9 ± 4 vol %) with an average composition of $An_{44}Ab_{45}Or_{11}$. Microprobe data show a narrow feldspar compositional range within North Crater, $An_{42-46}Ab_{50-54}Or_{3-4}$, plotting in the andesine field. The inclusion of anorthoclase in the model fit results in a Or value that is too high compared to measured values. Both the model derived composition and the microprobe data indicate that andesine is the feldspar mineral present.

Blue dragon feldspars are labradorite (12 ± 6 vol %), anorthoclase (10 ± 3 vol %), and oligoclase (9 ± 4 vol %) with a weighted average of $An_{47}Ab_{43}Or_{10}$. The range in feldspar compositions observed in the microprobe data is $An_{40-44}Ab_{52-56}Or_{3-4}$ consistent with an andesine composition. The Or component is, again, higher than the measured value due to the inclusion of anorthoclase. Andesine is identified as the feldspar mineral present through both techniques (Fig 4.5).

Modeled feldspars in the Campground flow include anorthoclase (14 ± 2 vol %), oligoclase (10 ± 3 vol %) and bytownite (7 ± 3 vol %) with a weighted average composition of $An_{30}Ab_{56}Or_{14}$. Microprobe data indicates that the campground sample contains andesine feldspar ($An_{34-40}Ab_{54-58}Or_{6-8}$). The model-derived composition is more potassic than the microprobe data indicates. The microprobe data identifies andesine and the model derived composition indicates a composition on the boundary between andesine and oligoclase.

The modeled fit to the Devil's Orchard spectrum includes anorthoclase (33 ± 6 vol %) and labradorite (12 ± 4 vol %) with a weighted average composition of $An_{26}Ab_{53}Or_{21}$. Microprobe data indicates that the Devil's Orchard sample contains feldspar near the compositional boundary between andesine and oligoclase ($An_{26-32}Ab_{59-61}Or_{9-13}$). This derived composition is, again, substantially higher in K due to the inclusion of abundant anorthoclase. The microprobe data indicates a mix of andesine and oligoclase while the model derived composition indicates a highly ternary oligoclase.

The modeled fit of the Serrate trachyte include anorthoclase (34 ± 3 vol %) and oligoclase (5 ± 2 vol %) and the weighted average feldspar composition is $An_{16}Ab_{59}Or_{25}$. The Serrate flow contains feldspar minerals with an anorthoclase composition ($An_{14-22}Ab_{56-60}Or_{18-28}$) which matches the modeled composition within error.

The Highway trachyte flow feldspars is modeled as anorthoclase (52 ± 4 vol %) with a composition of $An_{15}Ab_{57}Or_{28}$. Microprobe feldspar compositions show a range of $An_{13-21}Ab_{54-60}Or_{20-32}$ matching the modeled composition within error.

Olivine. The only samples that contain olivine abundant enough (>5%) to determine their composition are the ferrobasalts and olivine tholeiite. From microprobe data, the fo# of olivine in Wapi is fo69 ± 3. Modeled fits to the Wapi spectrum use

olivine fo54 (6 ± 1 vol %), olivine fo25 (5 ± 1 vol %), and forsterite (4 ± 1 vol %) with a weighted average of fo58 (Fig 4.6). This is outside of the 1σ error of measured fo# with the microprobe and is more Fe-rich.

The microprobe determined range in olivine composition for Broken Top is fo51 ± 1. The spectral model for Broken Top includes olivine fo35 (4 ± 2 vol %) and olivine fo68 (2 ± 1 vol %) with a modeled value of fo46 (Fig 4.6). This value is closer but still outside, to the Fe-rich side, of the range determined by microprobe.

Olivine in the North Crater flow is fo49 ± 1. Modeled fits of North Crater include olivine fo35 (6 ± 2 vol %) and fo 68 (2 ± 1 vol %) for a weighted average of fo41. Again, this value is close but more Fe-rich than the microprobe determined fo#.

Blue Dragon olivine is fo49 ± 2. The modeled fit to the spectrum includes olivine fo35 (11 ± 1 vol %) and forsterite (2 ± 1 vol %) with a weighted average composition of fo 45. This value is slightly more Fe-rich than the probe determined values but falls outside of the 1σ error.

TIR weighted absorption center. The position of the Si-O reststrahlen feature near ~700-1400 cm^{-1} has been observed to shift with a variation in sample SiO_2 content (Launer, 1952; Lyon, 1965; Vincent and Thomson, 1972; Smith et al., 2003; Walter and Salisbury, 1989; Wyatt et al., 2001; Rogers and Nekvasil, 2015; Amador and Bandfield, 2016; Salvatore et al., 2018). A sample containing abundant silica, with a higher degree of silica polymerization, is expected to produce absorptions at higher wavenumber compared to a sample with lower silica. To test this with a suite of evolved glassy volcanic rocks, the weighted absorption center (WAC) was determined for each full resolution spectrum and plotted against bulk sample SiO_2 (Fig 4.7). COTM thermal emission spectra are shown in Fig. 4.8 with the calculated position of the WAC marked with red lines. WAC and bulk SiO_2 show a positive linear correlation with a coefficient of determination (R^2) of 0.89 (Fig 4.7a). The most primitive sample,
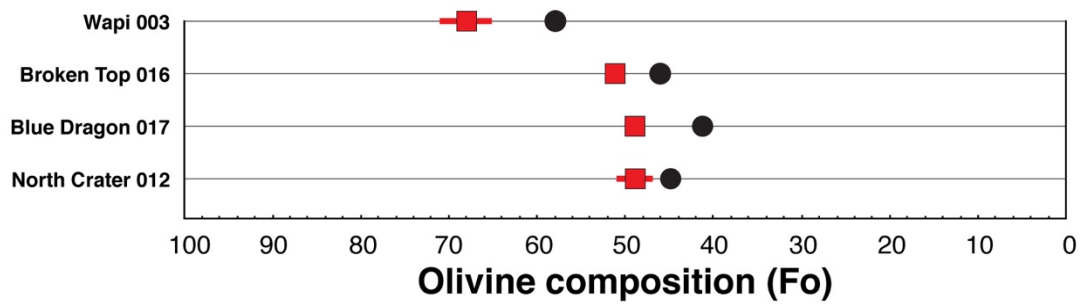
Figure 4.6. Thermal emission spectroscopy derived olivine compositions. Red boxes indicate the EPMA determined compositions and the red bars indicate the 1σ distribution within the sample. Black dots indicate the derived compositions. These are the only 4 samples with olivine modeled above the detection limit.
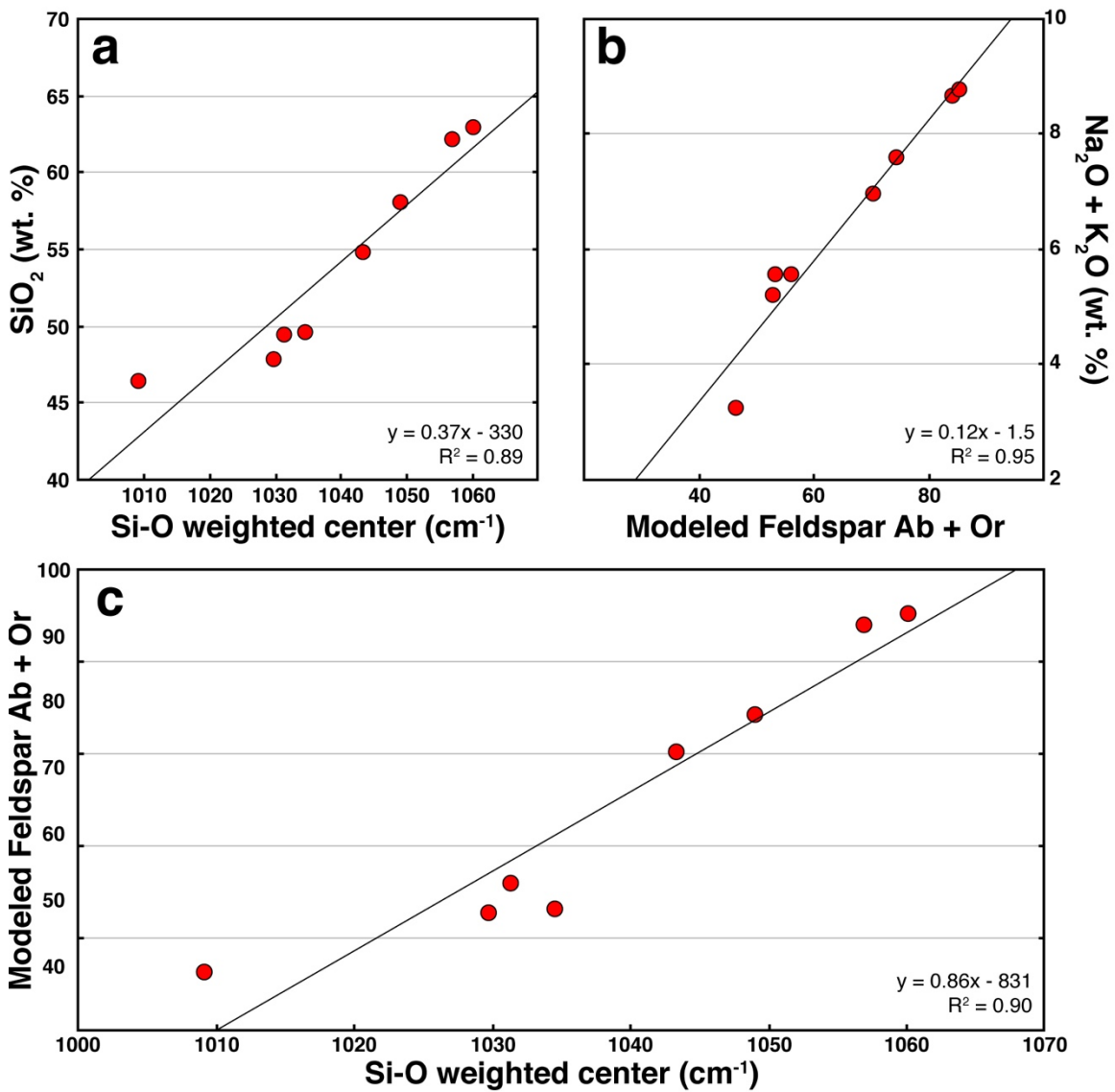
Figure 4.7. a) Bulk rock SiO_2 plotted vs. the weighted absorption center. b) Bulk rock total alkalis ($Na_2O + K_2O$) plotted against the TIR modeled Ab + Or components of the feldspar minerals. c) WAC plotted vs. TIR modeled Ab + Or to compare against the TAS plot shown in Figure 4.1a.
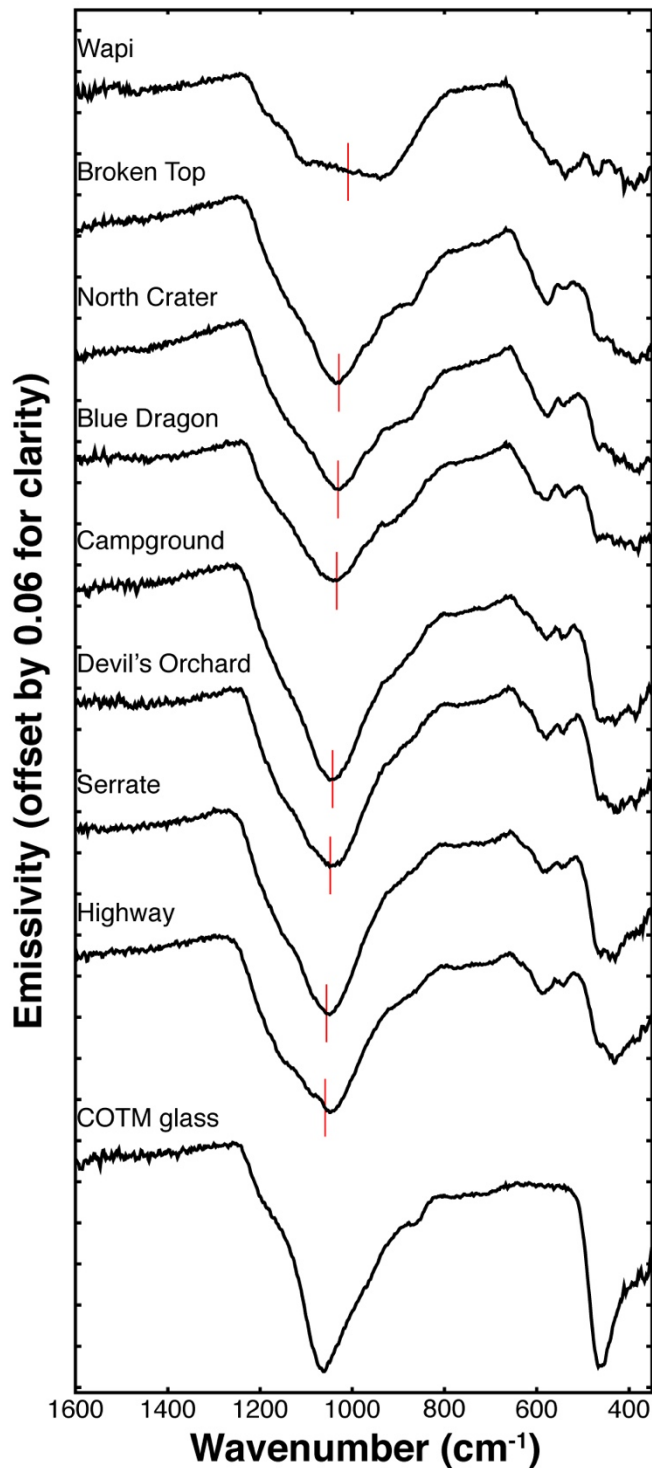
Figure 4.8. Thermal emission spectra examined in the study. Spectra are presented with the most primitive sample on the top and increasing degree of evolution downward. Red line indicates the WAC position. Bottom spectrum is the spectrum of COTM ferrobasaltic glass for comparison to the glassy COTM volcanic rocks.
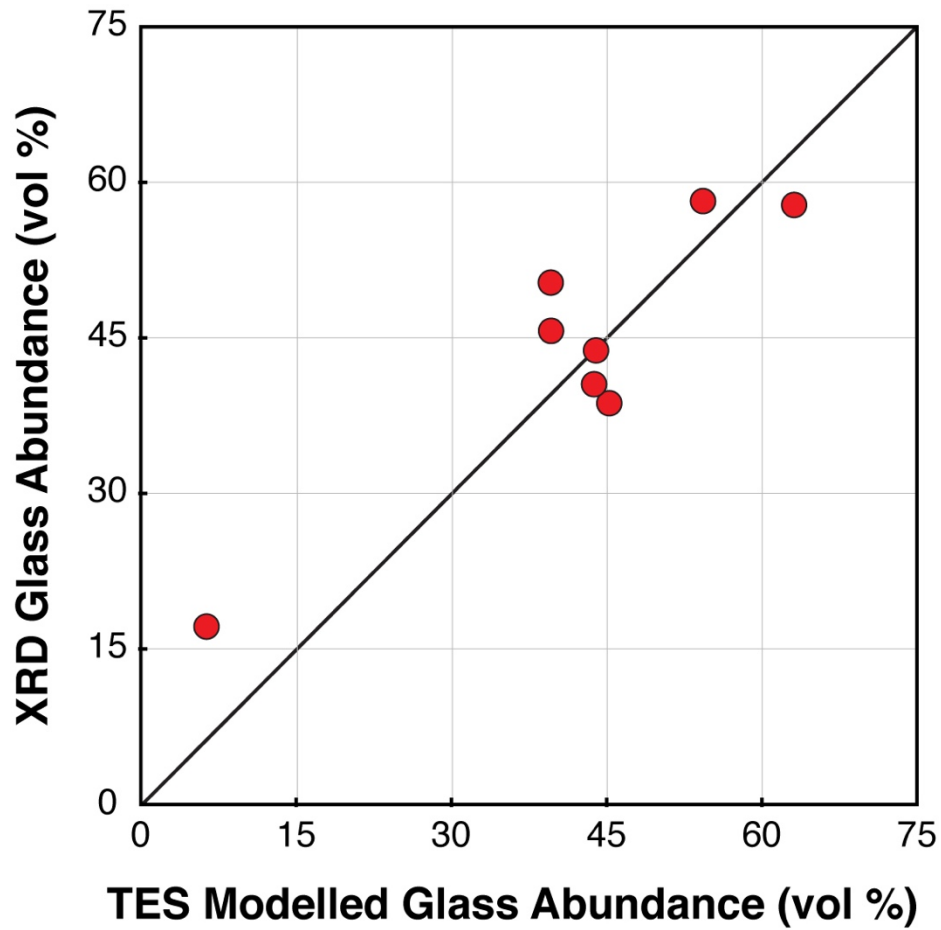
Figure 4.9. Comparison of derived glass abundances from empirically calibrated XRD background ratios and thermal emission spectroscopy spectral modeling.

olivine tholeiite, exhibits the lowest minimum position consistent with its low silica content (46.43 wt.%) and each subsequent sample shows an increase in WAC with increasing bulk SiO_2 consistent with the expected behavior.

XRD crystallinity. Glass abundances determined using the XRD background ratio technique (Wall et al., 2014) are in general agreement with the abundances determined using thermal emission spectroscopy (Fig 4.9). The average difference between the determined abundances is 5.8% and the maximum difference is $\geq 10\%$ on two occasions. The largest discrepancy is found in the Wapi olivine tholeiite where the thermal infrared modeled glass abundance is 6 vol % and the XRD determined abundance is 17 vol %. The second occasion is with the modeled glass abundance for Devil's Orchard where the spectral model gives an abundance of 40 vol % versus 50 vol % for values determined through XRD.

Discussion

The VNIR reflectance spectra of COTM ferrobasalts. The volcanics of Craters of the Moon show a classic tholeiitic differentiation trend where fractionation of olivine + plagioclase $\pm$ augite leads to early enrichment in iron producing the COTM ferrobasalts (Putirka et al., 2009). Enrichment of Ti is sympathetic with Fe reaching a peak of ~ 3.5 wt.% before rapidly diminishing with increasing evolution. Experiments conducted on similar ferrobasaltic compositions from the Galapagos indicate that coupled Fe-Ti enrichment and depletion trends are the result of ilmenite ($FeTiO_3$) saturation and fractionation (Juster et al., 1989). BSE imaging and EDS mapping of the COTM ferrobasalts reveals two populations of Fe-Ti oxides; microphenocryst clusters of titanomagnetite (10-50 µm) and small (1-10 µm) acicular ilmenite mantling feldspar microphenocrysts (Fig 4.10). The mantling ilmenite likely grew as quench crystals when the ferrobasaltic magma was erupted near ilmenite saturation and

80
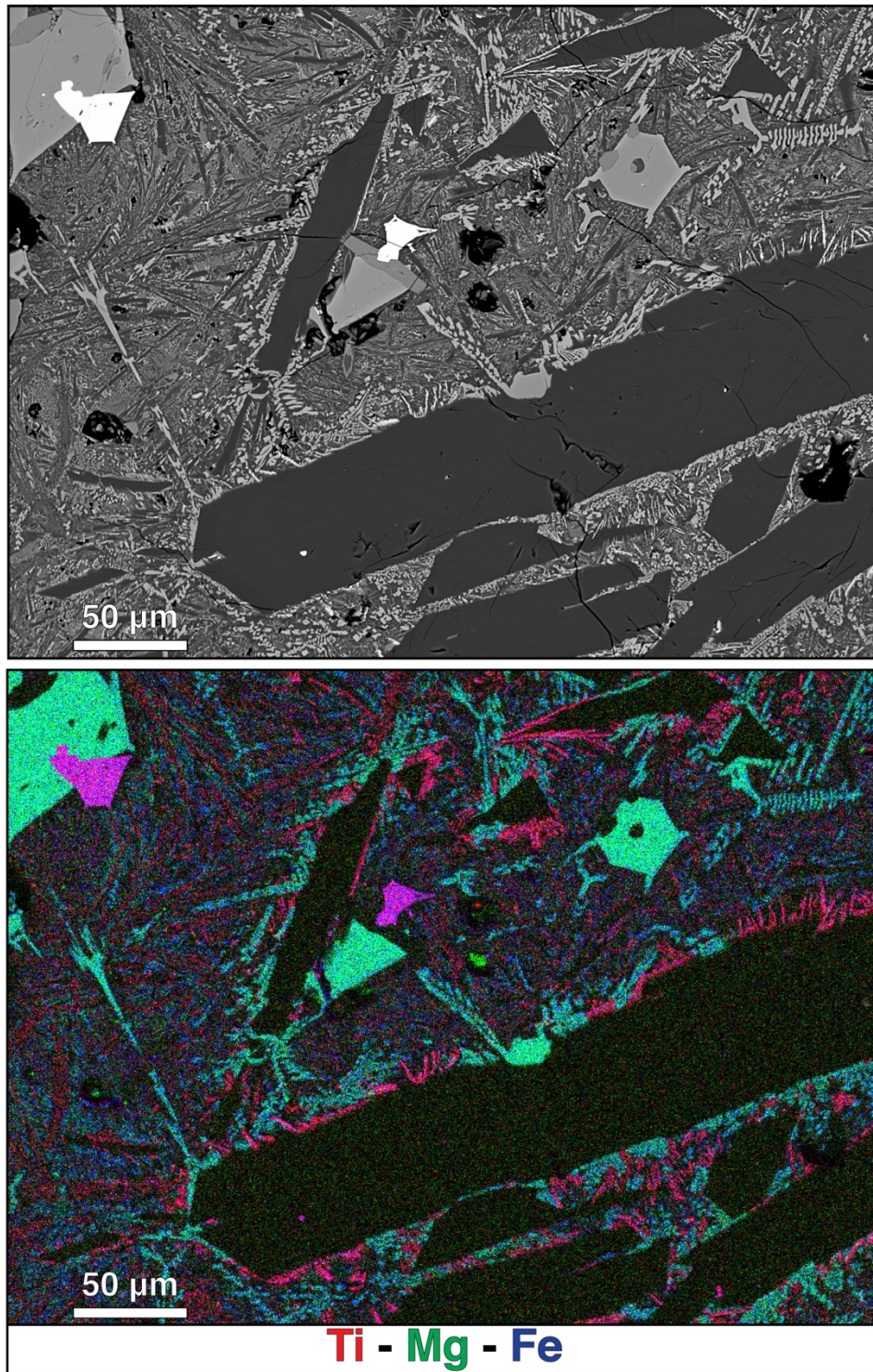
Figure 4.10. Top: BSE image showing the groundmass of the Broken Top ferrobasalt. White corresponds to Titanomagnetite, light grey is olivine, medium grey is apatite and dark grey is feldspar. Notice the abundant skeletal olivine crystals. Bottom: EDS false color chemical map showing Ti in Red, Mg in Green, and Fe in Blue. Purple colors are titanomagnetite, neon green is olivine, black is feldspar and red is the acicular mantling ilmenite.

81

cooled rapidly. The glass abundances determined through XRD, and TIR spectroscopy range from ~38-45 vol% consistent with a rapid cooling.

The VNIR spectra of the COTM ferrobasalts are characterized by a prominent absorption near 600 nm, a reflectance peak near 940 nm and a smooth red-sloped spectrum at wavelengths >1000 nm. The feature near 600 nm is commonly attributed to a Fe^{2+}-Ti^{4+} charge transfer absorption owing to the presence of ilmenite. Moreover, the MGM analysis only produces satisfactory fits to the spectrum when a broad (~1200 nm FWHM) absorption centered near 1600 nm is included, consistent with the presence of ilmenite. It is apparent from these analyses that a minor amount of ilmenite, present in the petrographic texture observed in COTM ferrobasalts, is dominating the spectral reflectance properties across the VNIR. The spectra of these ferrobasalts bear some resemblance to lunar impact melt breccias and pyroclastic glasses that also possess finely distributed ilmenite set in a transparent silicate groundmass (Adams and McCord, 1970; Arndt and Engelhardt, 1987; Tompkins and Pieters, 2010; Isaacson et al., 2011). This suggests that these rocks provide a good terrestrial analog to lunar materials and may provide insight into the processes that shape the spectra of lunar materials.

Crystallinity. The determination of the abundance of glass in a volcanic rock can be an important indicator of eruptive style and the conditions of emplacement (Wall et al., 2014). Furthermore, the ability to accurately constrain the abundance of glass using thermal emission spectroscopy is important for the remote determination of complete modal mineralogies. The general agreement between both techniques employed in this study is promising, though some large discrepancies are notable (Fig 4.9). The Wapi olivine tholeiite showed an 11 vol % difference between the two techniques which is substantial considering that the crystallinity is expected to be low from petrographic observations. Wapi exhibits textural variability across section and it

is possible that sample to sample variability is responsible for the large difference observed. However, the remaining samples are aphanitic and do not show significant variability in crystal distribution in thin section and it is unlikely that sample variability is responsible for the difference in glass abundance observed for Devil's Orchard (11 vol %). An attempt was made to provide an additional assessment of glass content through image processing of BSE images but the finely crystalline nature of the groundmass led to irreproducible results. The investigation of additional samples covering a broad range crystallinity is needed to further characterize the accuracy of the two methods.

Reproducibility of major phase composition. Mineral compositions derived from the thermal emission spectra of these natural samples provide an accurate estimation when compared to compositions derived using a high-fidelity analytical instrument (Figs 4.5 and 4.6). In most instances the derived compositions of feldspar minerals were too potassic leading to an estimate outside of the 1σ distribution observed through EPMA. In each case the model includes anorthoclase in the fit as opposed to a feldspar composition more closely related to the plagioclase in the sample. Feldspars, like other major mineral groups, exhibit systematic variations in their spectral features with varying composition that allows for the determination of their composition using this technique (Nash and Salisbury, 1991; Ruff, 1998). If anorthoclase is used frequently to fit the features of plagioclase feldspars this suggests that a particular spectral feature present in anorthoclase and the COTM feldspars is not represented by the existing library suite of plagioclase feldspars. The potassic nature of the COTM silica-saturated alkalic trend provides additional evidence that this is the case. The feldspars observed across the SRP, and the chemically similar Laramie anorthosite complex, are more potassic than suites of rocks from different silica-saturated trends (Nekvasil, 2000). This is true for even the least evolved compositions.

83

In light of this, further investigation of the SRP rocks using *in situ* micro-spectroscopy is warranted to ascertain the nature of this discrepancy. Despite the potential differences between library and COTM feldspar chemistry, this analysis reproduced the compositional trend observed in feldspar composition and was able to accurately determine the proper feldspar classification.

Olivine compositions derived from the four rocks with abundant olivine were similarly close but systematically more Fe-rich than the EPMA data indicate. The spectral library provides high quality olivine spectra covering an extensive compositional range (fo#'s 0, 10, 18, 25, 35, 39, 54, 60, 65, and forsterite) and a lack of representation is not expected to be the cause of the discrepancy. It is possible that the EPMA data are not representative of the compositional population of olivine within the samples owing to either zoning or the ubiquitous micron-sized olivine quench crystals. In both cases it would be expected that these products exhibit a more Fe-rich composition which could explain the systematically Fe-rich derived composition using thermal emission spectroscopy.

Total alkalis vs. Silica. An initial enrichment in alkalis (Na_2O and K_2O) due to fractionation of olivine and plagioclase ($\pm$ augite) drives this suite from the subalkalic field of Irvine and Baragar, (1971; Fig. 4.1) into the alkalic field (Putirka et al., 2009). With the onset of Fe-Ti oxide crystallization, silica (SiO_2) becomes strongly enriched concomitant with continued enrichment in alkalis. This major element trend is a common feature of intra-plate igneous suites. The steady increase in Na and K with coupled depletion of Ca produces a strong, continuous trend in feldspar composition transitioning from more calcic bytownite to the Na and K-rich ternary feldspar anorthoclase (Fig 4.2, 4.5). Changes in feldspar composition are expressed in their TIR spectrum and linear least squares modelling of the COTM TIR spectra accurately tracks the compositional variability observed through EPMA (Fig 4.5). The sum of the

feldspar Ab and Or components determined through spectral unmixing is well correlated with the sum of bulk Na_2O and K_2O determined through XRF with a R^2 value of 0.95 (Fig 4.7b).

The infrared spectrum of silicate minerals is dominated by vibrational absorptions related to molecular Si-O with a particularly strong and diagnostic region between 1400 - 700 cm^{-1} (Launer, 1952; Lyon, 1965). The wavenumber position (frequency) of Si-O reststrahlen absorptions is sensitive to changes in bulk SiO_2 Launer, 1952; Lyon, 1965; Vincent and Thomson, 1972; Smith et al., 2003; Walter and Salisbury, 1989; Wyatt et al., 2001; Rogers and Nekvasil, 2015; Amador and Bandfield, 2016; Salvatore et al., 2018). In the SRP suite this property is demonstrated by the well correlated trend of WAC vs. SiO_2 (Fig 4.7a).

In the absence of a bulk chemical composition determination, thermal infrared spectral observations of the composition of feldspar minerals and the position of the Si-O reststrahlen feature in volcanic rocks can be informative about their classification and degree of evolution, serving as a proxy for the Total Alkalis vs. Silica (TAS) diagram (Fig 4.1 & 4.7c). A comparison of the TAS diagram to the Ab+Or vs. WAC shows a general similarity in plotted position for all samples excluding the olivine tholeiite, which appears to be an outlier. The WAC for the olivine tholeiite is significantly lower than the ferrobasalts (1009.1 vs. 1029.7 cm^{-1}) even though their bulk SiO_2 is similar (Wapi, 46.43 wt. %; Broken Top, 47.85 wt. %). The most notable difference between the olivine tholeiite and the other samples in the suite is their crystallinity (Fig 4.9). The presence of abundant glass plays a significant role in the shape and position of the main Si-O absorption band (Fig 4.8). A spectrum of COTM ferrobasaltic glass, collected from the southern flank of the North Crater cinder cone, is shown in Figure 4.8 and highlights the similarities between the COTM rocks and volcanic glass. The WAC position for the COTM glass is 1049 cm^{-1} and, from Figure

85

4.7, it appears that the presence of abundant glass in the COTM rocks introduces a WAC bias to higher positons. Notwithstanding, the trends observed in modeled Ab + Or and WAC position show an increase in both values with increasing degree of evolution. These observations indicate that the thermal infrared spectra of volcanic rocks can be used to gauge their degree of compositional evolution.

Conclusions

Combined VNIR and TIR observations of the diverse suite of igneous rocks in the Snake River Plain can be used to identify major element evolutionary trends typical of magmatic evolution and intra-plate basaltic volcanism. Feldspar is generally the most abundant major phase in volcanic rocks and its composition reflects the evolutionary trends that define numerous magmatic suites. The determination of feldspar composition using TIR spectroscopy is enabled due to its high abundance. TIR spectroscopy determinations of feldspar chemistry on Mars could provide a means for investigating the petrogenesis of a suite volcanic rocks. In addition, the position WAC across the main Si-O absorption band is sensitive to SiO_2 abundance. When coupled with observations of feldspar chemistry, these two parameters could be used to infer the composition and classification of a volcanic rock in the absence of a bulk chemistry determination.

Enrichment of Fe is a common occurrence during the early stages of differentiation within tholeiitic suites. This leads to the formation of ferrobasalts like those observed in COTM. This Fe-enrichment and steady Mg-depletion leads to a noticeable change in the composition of olivine. Similar to the trend observed in feldspar, this compositional variation is an indicator of magmatic evolution that TIR spectroscopy is sensitive to.

In ferrobasaltic rocks, titanium can experience an enrichment simultaneous to that of Fe. When a melt is erupted with a sufficiently high amount of both Fe and Ti,

ilmenite will saturate forming quench crystals. In the COTM ferrobasalts, this lead to the rapid deposition of a micron-scale mantle of acicular ilmenite on the exterior of plagioclase phenocrysts. Consequently, VNIR observations of COTM ferrobasalts are dominated by features attributable to ilmenite, even though it is a volumetrically minor phase. Similar petrographic textures and spectral features are observed in lunar impact melt breccia and pyroclastic glass deposits. These similarities suggest that the COTM ferrobasalts are a unique terrestrial analog to lunar glassy materials and their further investigation may provide insight about the nature of lunar materials. Additionally, identification of a similar 600 nm Fe^{2+}-Ti^{4+} charge transfer absorption on Mars would provide information about the presence of ilmenite saturated basalts. Searching for these spectral trends on the surface of Mars, and other planetary bodies, can yield valuable insight to magmatic processes occurring within and on the surface of the planet.

Table 2

Major and trace element whole rock XRF analyses.

	Wapi	Broken Top	North Crater	Blue Dragon	Camp-ground	Devil's Orchard	Serrate	Highway
	WA003	COTM016	COTM012	COTM017	COTM014	COTM015	COTM009	COTM013
Unnormalized Major Elements (Weight %):								
SiO_2	46.43	47.85	49.45	49.61	54.82	58.07	62.17	62.95
TiO_2	2.814	3.188	2.772	2.866	1.658	1.181	0.678	0.594
Al_2O_3	14.95	12.64	12.95	13.02	13.78	13.83	14.23	14.04
FeO*	13.41	16.40	16.12	15.70	13.86	12.38	9.02	8.53
MnO	0.202	0.281	0.280	0.283	0.251	0.238	0.196	0.189
MgO	7.29	3.61	3.08	3.17	1.59	0.87	0.30	0.20
CaO	10.22	7.40	6.78	6.94	4.94	4.17	3.11	2.99
Na_2O	2.57	3.36	3.48	3.50	3.98	4.11	4.19	4.10
K_2O	0.68	1.85	2.09	2.07	2.99	3.49	4.48	4.68
P_2O_5	0.766	2.359	1.953	2.035	0.994	0.532	0.187	0.155
Sum	99.34	98.93	98.95	99.19	98.86	98.87	98.55	98.45
LOI %	0.00	0.00	0.00	0.00	0.00	0.00	0.00	0.39
Unnormalized Trace Elements (ppm):								
Ni	103	11	9	6	6	5	5	6
Cr	193	0	0	0	0	0	1	1
Sc	30	26	27	28	25	26	21	17
V	292	144	99	111	12	4	8	2
Ba	426	1337	1509	1476	1983	2353	3880	3668
Rb	14	38	44	42	67	78	94	100
Sr	312	288	286	288	258	225	191	147
Zr	267	890	1014	999	1490	2501	1754	1634
Y	40	104	109	110	119	122	125	131
Nb	24.6	85.3	93.7	93.7	117.6	128.2	136.3	142.1
Ga	19	23	25	25	28	26	29	29
Cu	46	91	30	26	16	16	12	9
Zn	128	229	236	237	244	242	222	227
Pb	4	20	16	18	25	29	34	36
La	26	102	117	115	139	147	153	159
Ce	62	223	238	239	284	287	304	313
Th	1	4	6	5	9	10	11	13
Nd	38	122	125	124	134	135	134	143
U	2	2	5	1	3	4	3	3
Total (ppm)	2026	3741	3990	3946	4960	6339	7118	6780
Total (wt. %)	0.20	0.37	0.40	0.39	0.50	0.63	0.71	0.68

Table 3

MGM absorption band parameters for fits to COTM VNIR reflectance spectra.

	Wapi			Broken Top			North Crater			Blue Dragon		
	Center (nm)	Width (nm)	Strength (%)	Center (nm)	Width (nm)	Strength (%)	Center (nm)	Width (nm)	Strength (%)	Center (nm)	Width (nm)	Strength (%)
Band 1	201	299	-0.69	196	231	-1.33	192	233	-1.27	192	197	-1.16
Band 2	501	231	-0.21									
Band 3§	678	144	-0.04	546	345	-0.32	550	340	-0.25	559	323	-0.10
Band 4	924	152	-0.01	886	150	0.00	889	152	0.00	881	160	-0.01
Band 5	1031	185	-0.03	1091	216	-0.02	1079	217	-0.02	1053	229	-0.03
Band 6	1178	312	-0.01									
Band 7	1370	299	-0.02	1325	336	-0.04	1329	330	-0.04	1319	329	-0.04
Band 8§	1653	1204	-0.15	1673	1378	-0.16	1597	1411	-0.15	1470	1625	-0.12
Band 9	2315	583	-0.03									
RMS error	0.117%			0.239%			0.205%			0.210%		
Continuum	C_{-1}	C_0	C_1	C_{-1}	C_0	C_1	C_{-1}	C_0	C_1	C_{-1}	C_0	C_1
	-8.20E-02	-1.26E+00	-1.15E-01	-1.05E-01	-1.68E+00	2.08E-01	-9.88E-02	-1.70E+00	1.65E-01	-1.48E-01	-1.39E+00	4.77E-02

§ These bands are interpreted to originate from finely dispersed ilmenite. C_{-1} is a linear in energy slope term, C_0 is an offset and C_1 is a linear in wavelength term (Hiroi et al., 2000; Noble et al., 2006).

Table 4

MGM absorption band parameters for fits to COTM VNIR reflectance spectra.

	Campground			Devil's Orchard			Serrate			Highway		
	Center (nm)	Width (nm)	Strength (%)	Center (nm)	Width (nm)	Strength (%)	Center (nm)	Width (nm)	Strength (%)	Center (nm)	Width (nm)	Strength (%)
Band 1	196	231	-1.39	175	253	-1.51	174	244	-1.70	190	259	-1.12
Band 2	460	272	-0.14	435	274	-0.09	422	266	-0.10	464	230	-0.08
Band 3	905	118	-0.01	906	123	-0.01	930	116	-0.01			
Band 4	1010	150	-0.03	1015	147	-0.03	1016	134	-0.03			
Band 5	1023	146	-0.03	1033	145	-0.02	1026	132	-0.03	1021	152	-0.05
Band 6	1169	356	-0.03	1177	339	-0.02	1105	349	-0.03	1169	538	-0.05
Band 7	1320	508	-0.04	1325	510	-0.03	1327	509	-0.03			
Band 8	2031	651	-0.02	1966	685	-0.03	2056	681	-0.02	2320	659	0.00
RMS error	0.141%			0.162%			0.175%			0.262%		
Continuum	C_{-1}	C_0	C_1	C_{-1}	C_0	C_1	C_{-1}	C_0	C_1	C_{-1}	C_0	C_1
	-7.91E-02	-1.40E+00	1.40E-01	1.25E-02	-1.42E+00	-1.57E-04	-8.13E-02	-9.57E-01	3.49E-02	-1.06E-01	-1.06E+00	4.69E-02

C_{-1} is a linear in energy slope term, C_0 is an offset and C_1 is a linear in wavelength term (Hiroi et al., 2000; Noble et al., 2006).

CHAPTER 5

Revisting the Alkaline Volcanic Rocks of Gusev Crater with Mini-TES

Introduction

In 2004 the Mars Exploration Rover, Spirit, landed on Mars and began its geologic investigation of Gusev crater. Spirit was equipped with an instrument suite tailored to characterize the texture, chemistry, and mineralogy of the rocks, regolith and dust encountered along its traverse (Squyres et al., 2004). Textural information is gained from a Microscopic Imager (MI) designed to act as a geologist's hand lens (~30 μm/pixel) on the end of Spirit's robotic arm (Herkenhoff et al., 2003). Also mounted on the arm were the Alpha Particle X-ray Spectrometer (APXS) and Mössbauer spectrometer, providing observations of bulk chemistry and the oxidation state of iron, respectively (Klingelhöfer et al., 2003; Rieder et al., 2003). Mineralogical information was obtained from the miniature Thermal Emission Spectrometer (Mini-TES), Panoramic Camera (PanCam) multispectral imager, and the Mössbauer spectrometer (Christensen et al., 2003; Bell et al., 2003). On sol 420 regional dust storms led to the deposition of a thin layer of dust on the Mini-TES pointing and fold mirrors (located in the Pancam Mast Assembly) hindering the derivation of quantitative modal mineralogies using Mini-TES observations collected after this aeolian event (Ruff et al., 2006; Smith et al., 2006). A rigorously tested correction for the spectral contribution of this thin coating of mirror dust was not produced and applied to surface observations until years later (Ruff et al., 2011). Mirror-dust-corrected Mini-TES observations are now publicly available through the geoscience node of the planetary data system (PDS). Reanalysis of these data provide useful constraints on mineral compositions and proportions providing a more complete mineralogical and geochemical picture, as originally intended (Christensen et al. 2003).

93

During its ascent of Husband Hill, Spirit encountered several distinct classes of volcanic rock based upon their Mini-TES spectra (Ruff et al., 2006), now referred to as the Irvine, Backstay, and Wishstone classes. Upon full characterization by Spirit's suite of contact instruments, they were determined to be alkaline volcanic rocks (McSween et al., 2006). These rocks represent the first observations of alkalic volcanic rocks on Mars, pointing to more geochemically diverse modes of Martian volcanism than previously thought. The Wishstone-class was the subject of a previous report (Ruff and Hamilton, 2017); the Irvine and Backstay-class rocks are the focus of the current investigation. Irvine-class rocks were first encountered as an alignment of dark float, reminiscent of a dike, and second, as vesicular lava outcropping in the Inner Basin of the Columbia Hills. Based on the MI, Mössbauer and APXS investigations, the Irvine-class is an aphanitic, minimally altered, alkalic basalt. All Backstay-class rocks were observed as float, encountered near the crest of Cumberland Ridge and on the upper slopes of Husband Hill. Chemically, Backstay is enriched in K and Na, and thus classified as a trachybasalt (McSween et al., 2008). The alkalic nature of both classes suggest they could be formed by fractionation of a melt compositionally similar to the Adirondack class plains basalts (McSween et al., 2006).

Initially, mineralogies of the Irvine and Backstay-class rocks were determined through a CIPW normative calculation modified to reflect the results of the Mössbauer spectrometer (Ruff et al., 2006; McSween et al., 2006; McSween et al., 2008). Based upon this calculated norm, infrared spectra were synthetically generated for each rock in order to visually compare with the dust-contaminated spectrum (McSween et al., 2006, 2008). When compared to the Mini-TES spectra, the synthetically generated spectra were a poor match, likely due to the spectral contribution of mirror dust and the limited ability of normative calculations to predict volcanic mineralogies. The

primary objective of this study is to build upon these previous investigations by determining mineralogy directly from mirror-dust corrected Mini-TES observations.

Recent investigations concerning the oxidation state of the Martian mantle have brought renewed attention to the volcanic rocks of Gusev Crater (Schmidt et al., 2013; Tuff et al., 2013). Measured values of Fe^{3+}/Fe_{total} from the Spirit Mössbauer spectrometer indicate a primary oxygen fugacity (fO_2) of 1.5 log units above the fayalite-magnetite+quartz buffer (FMQ) for Irvine and ΔFMQ -0.7 for Backstay (Schmidt et al., 2013). Both of these values are similar to or more oxidized than the most oxidized basaltic shergottites whose fO_2 ranges from approximately ΔFMQ -4 to 0 (Smith and Hervig, 1979; Herd et al., 2001, 2002; Goodrich et al. 2003; Wadhwa, 2008). Taking note of the apparently oxidized volcanic rocks in Gusev crater and their ancient age, Tuff et al. (2013) proposed that volcanism on early Mars was derived from a more oxidized upper mantle with a time-transgressive shift toward volcanism derived from a deeper more reduced mantle source. This model correctly accounts for the observed chemical differences in Ni, S and Mn/Fe between the shergottite-nakhalite-chassignite (SNC) meteorites and the Gusev crater rocks. However, further analysis of Mössbauer data determined that, in all cases, contribution from secondary phases and dust results in an overestimate of the primary fO_2 for volcanic rocks and a careful reanalysis of these data using a variety of methods yielded updated estimates of the primary fO_2 values for the Irvine (ΔFMQ -0.2 to 0.7) and Backstay (ΔFMQ -3.3 to -2.0) classes. These recalculated values for fO_2 are more consistent with the Shergottites, though, Irvine still occupies the higher fO_2 range. The discrepancies between the estimated fO_2 of the ancient Gusev crater rocks have important implications for the early evolution of the Martian crust and mantle and further constraints on the primary fO_2 of these rocks are warranted. This discrepancy is investigated here using Mini-TES observations and thermodynamic modelling tools.

In terrestrial lavas fO$_2$ can vary over 7 orders of magnitude expressing a greater degree of variation than any other petrogenetic parameter (Sack et al., 1981; Carmichael and Ghiorso, 1990). Changes in fO$_2$ significantly impact the chemistry of silicate melts where, with increasing oxidation, a greater fraction of total Fe is represented as ferric Fe$_2$O$_3$ thus decreasing the ferrous FeO/MgO of the melt. This variability influences the stability and composition of crystallizing ferromagnesian silicates which can result in significantly different mineral assemblages formed from the same bulk composition. As a secondary objective, this investigation will utilize the MELTS thermodynamic modelling tool to investigate the impact of varying fO$_2$ on the phase equilibria in melts of Irvine and Backstay composition (Ghiorso and Sack, 1995). From these calculations we will generate thermal emission spectra to investigate spectral variability in these bulk compositions over a broad range of fO$_2$.

Methods

Mini-TES instrument and data. The Mini-TES is a Fourier Transform Infrared spectrometer that collects data over the spectral range of 339.5 - 1997.06 cm^{-1} (5-29 μm) with a spectral sampling interval of ~10 cm^{-1} (Christensen et al., 2003). A 20 mrad field of view results in a ~20 cm spot size from a distance of 10 m. The spectra used in this study are the result of long duration observations, where Mini-TES would collect between 100-200 individual observations of a target at a fixed point. The observed spectra were then averaged together to improve signal-to-noise. All spectra examined in this study were collected after the sol 420 aeolian event that deposited dust on the Mini-TES fore optics. To account for this a mirror-dust-correction was applied to each observation following the methods of Ruff et al., (2011). Mini-TES observed nine Backstay-class rocks (Backstay, Nilgiri, Taj Mahal, Black Cat, Missle, Bartlett, Molly, Bastille, and Dauphine) and five Irvine-class rocks (Irvine, Compagnoni, Unsoeld, Whillans, and Adze) on Husband Hill. For this study we focus

on the initial, well-characterized occurrence of the Irvine-class on Husband Hill. Each set of spectra were visually inspected and those with the lowest contribution from surface dust were selected to represent each class. For Irvine the best spectrum was Whillans, acquired on sol 599 (p3143). As mentioned above, the Irvine-class was first encountered as a linear alignment of dark float rock. Irvine was the first spectrum collected on sol 590 while approaching this alignment. Once identified as a target of interest, Spirit moved closer to begin a detailed investigation, at which point, additional high-quality Mini-TES observations were collected from multiple targets along the alignment, including Whillans. The close proximity to Irvine and similarity in spectral features gives us confidence that the Whillans spectrum is a high-quality representative of the class. The Backstay spectrum is the highest quality spectrum of the class likely because Backstay is a ~25 cm boulder with a well exposed surface ideal for the Mini-TES FOV.

Linear least squares fitting and refining the spectral library. A modified, non-negative, linear least squares fitting algorithm with a library of spectral endmembers is employed to determine the mineralogy of Backstay and Whillans (Rogers and Ahronson, 2008). Spectra were fit between 1500 - 380 cm^{-1} with the region from 780 - 560 cm^{-1} excluded due to the strong absorption of atmospheric CO_2. The library used in this study is identical to the library used to model the composition of the Adirondack class plains basalts with one additional pigeonite endmember (Table 1; Hamilton and Ruff, 2012). The additional pigeonite spectrum was collected from mineral separates of an interior chip of lherzolitic shergottite Yamato-984028 (Dyar et al., 2011). Due to a grain size of ~125 μm the spectral contrast of the absorption bands was lower than that for most minerals in the endmember library, which are 750-1000 μm in size. To compensate for this, the spectrum was scaled to match the contrast of the other pigeonite mineral in the library. When observing rocks with

97

Table 1

Mini-TES Adirondack Spectral library

Feldspar	Pyroxene	Olivine	Oxides	Low-Si Glass	High-Si phases	Sulfates
Albite (WAR-0612)	Augite (HS-119.4b)	Forsterite (BUR-3720A)	Magnetite (MTS5)	Quenched Basalt	Alkali Glass	Coquimbite (S46)
Oligoclase (WAR-0234)	Augite (BUR-620)	Forsterite (AZ-01)	Chromite (z122)	RVM Mars Glass	SiO2 Glass	Ferricopiapite (S35)
Oligoclase (BUR-3680)	Augite (NMNH-9780)	Fo65 (KI 3115)		Basalt Rind Spot B HWMK124D	Ca-Montmorillonite STx-1 (Solid)	Rozenite (JB626)
Labradorite (WAR-4524)	Augite (DSM-AUG01)	Fo53 (KI 3372)		Basalt Matte Uneven Surface HWMKV340A	Illite Imt-2 (Granular)	Szomolnokite (104276)
Labradorite (BUR-3080A)	Augite (NMNH-80819)	Fo39 (KI 4143)		Basalt Glassy Flat Black Surface HWMKV340A	Fe-smectite SWa-1 (Solid)	Pickeringite (S49)
Labradorite (WAR-RGAND01)	Diopside (HS-15.4B)	Fo18 (KI 3354)			Crystalline heulandite	Jarosite (S51)
Bytownite (WAR-1384)	Diopside (DSM-DIO01)	Fayalite (WAR-RGFAY01)			Crystalline stilbite	Natrojarosite (S48)
Shocked Bytownite 22.6 GPa	Hedenbergite, Mn (DSM-HED01)				Analcime tuff	Gypsum (S8)
	Hedenbergite, Mn (NMNH-R11524)					Anhydrite (S16)
	Hedenbergite (NMNH-16168)					Celestite (S3)
	Pigeonite (Wo10 En36 Fs54)					Kieserite (C5492-1)
	Enstatite (NMNH-166555)					Glauberite (S37)
	Bronzite (NMNH-166555)					
	Bronzite (NMNH-C2368)					
	Orthopyroxenite (ALH84001)					

Source data: This library is identical to Hamilton and Ruff (2012). Spectra from Christensen et al. (2000), Wyatt et al. (2001), Johnson et al. (2002), Lane et al. (2002), Ruff (2004), Ruff et al. (2006 and references therein), Lane (2007), and Hamilton (2010).

98

irregularly faceted surfaces, Mini-TES is often sampling surfaces with multiple distinct temperatures and this can introduce a spectral slope during the conversion from radiance to emissivity. This slope was approximated by dividing a 250 K Planck radiance curve by a 247 K radiance curve. This behavior was identified during pre-integration Mini-TES testing and the addition of a slope component to the library has been shown to improve the results of spectral fitting (Christensen et al., 2003; Ruff et al., 2006). Optically thin surface dust is added to the library to model any thin surface coatings of dust potentially unaccounted for during the mirror-dust-correction. An additional environmental component that is prevalent on the surface of Mars is optically thick deposits of dust. Mini-TES observed multiple deposits of surface dust early in the mission (before the mirror dust deposition) and an average spectrum of observations on sols 52 (p3621, p3726) and 78 (p3653, 3654) is used to represent dust within the FOV of Mini-TES. To characterize the environmental conributions to the spectrum, endmembers for spectral slope (temperature), optically thin surface dust and Gusev thick surface dust were included in the library.

A previous Mini-TES investigation of volcanic rocks in Gusev crater noted unexpectedly high abundances of sulfate when modeling the Mini-TES spectra of multiple Adirondack-class plains basalts (Hamilton and Ruff, 2012). The abundance of sulfate modelled was not in agreement with the APXS-derived chemistry of the Adirondack class rocks examined in this study, suggesting the Mini-TES analysis was overestimating its abundance. It was proposed that the presence of optically thin dust leads to an increase in modeled sulfate and olivine with a concomitant decrease in modeled feldspar. To examine this behavior during the analysis of Backstay and Whillans both the full library and the library with sulfates excluded will be employed and reported.

MELTS modelling. Phase equilibria were calculated using the MELTS thermodynamic modelling software and the APXS-derived compositions for Irvine and Backstay (Ming et al., 2008). Both Backstay and Irvine display subconchoidally fractured surfaces similar to terrestrial glassy volcanic rocks (Fig. 5.1 and 5.2) and no discernable phenocrysts are present with the MI. In contrast, the Wishstone and Adirondack classes have observable phenocrysts. Assuming that Backstay and Irvine represent melt compositions, calculations were performed at a pressure of 1 bar under equilibrium crystallization conditions to simulate a simple case of a melt cooling after emplacement on the surface. Each composition was modeled across the fO_2 range of ΔFMQ -6 to +3 under dry (0.0 wt. % H_2O) conditions to investigate the impact of fO_2 on the modeled phase assemblages. Model calculations were also made using 2.0 wt. % H_2O but had no effect on the phase equilibria for calculations at low pressure (1 bar). Minor abundances of SO_3 and Cl were removed from these compositions and the remaining oxides were normalized to 100% following the logic of McSween et al., (2008). Initially all Fe was represented as FeO but was later recalculated to the appropriate values for FeO and Fe_2O_3 based on the selected oxygen reference buffer (FMQ -6 to +2). The melt was held at this oxygen buffer throughout crystallization.

Deriving spectra from MELTS phase equilibria. Each MELTS calculation produces a series of output files that contain physical and chemical information describing the system and the individual phase(s) crystallizing at each model step. The outputs were processed to provide complete modal mineral abundances (vol %) and major phase chemistry from melt fractions of 100% (all melt) to 0% (completely crystalline) at 5% increments. At each step the major crystallizing phases are chemically binned and assigned to an infrared spectrum that most closely matches their composition and the melt fraction is treated as glass. High-quality infrared emission spectra of compositionally relevant mineral endmembers were used to

100

generate each spectrum based upon the modeled MELTS phase equilibria (or mineralogy) (Table 2). MELTS models were performed for two bulk compositions (Irvine and Backstay), over 10 oxidations states (FMQ -6 to +3) at 21 crystallization steps (0-100% melt), ultimately resulting in 420 MELTS-derived spectra. In order to effectively analyze this large dataset each spectrum was resampled to Mini-TES spectral resolution and compared to the Mini-TES spectrum representing its bulk composition using a linear least squares algorithm that includes a blackbody to adjust for differences in spectral contrast. Quality of fit was determined by root mean squares (RMS) error analysis. RMS is reported and plotted as a function of fO_2 and crystallinity. Each MELTS-derived spectrum was fit to the Mini-TES spectrum three times: first with the spectrum alone, second, with the spectrum and a thermal slope normalized to unity at the Christiansen frequency, and lastly, with the spectrum, thermal slope and an average Gusev surface dust spectrum.

Results

   Mini-TES-Derived Mineralogy of Irvine-class. Similar to the investigation of Adirondack-class basalts (Hamilton and Ruff, 2012), models of Whillans using a library populated with sulfate minerals results in an unexpectedly high abundance of sulfate (~21 vol%) and an improvement in the RMS error (0.32 % vs. 0.44 %) compared to a library with sulfates excluded. The APXS measured abundance of SO_3 in Irvine (2.37 wt.%) is too low to account for this high abundance of modeled sulfate. It is possible that Whillans, the Irvine-class target used for this model, contains much more SO_3 than Irvine but we consider this unlikely. Instead we suggest that the model is overestimating sulfate due to inadequacies in the spectral library. Modeled fits of Whillans using both libraries, sulfate-included and sulfate excluded, reproduce most of the spectral features observed, with the exception of two sharp absorptions between 1000-1040 cm^{-1}. These features are attributable to the sodic feldspar, albite. The
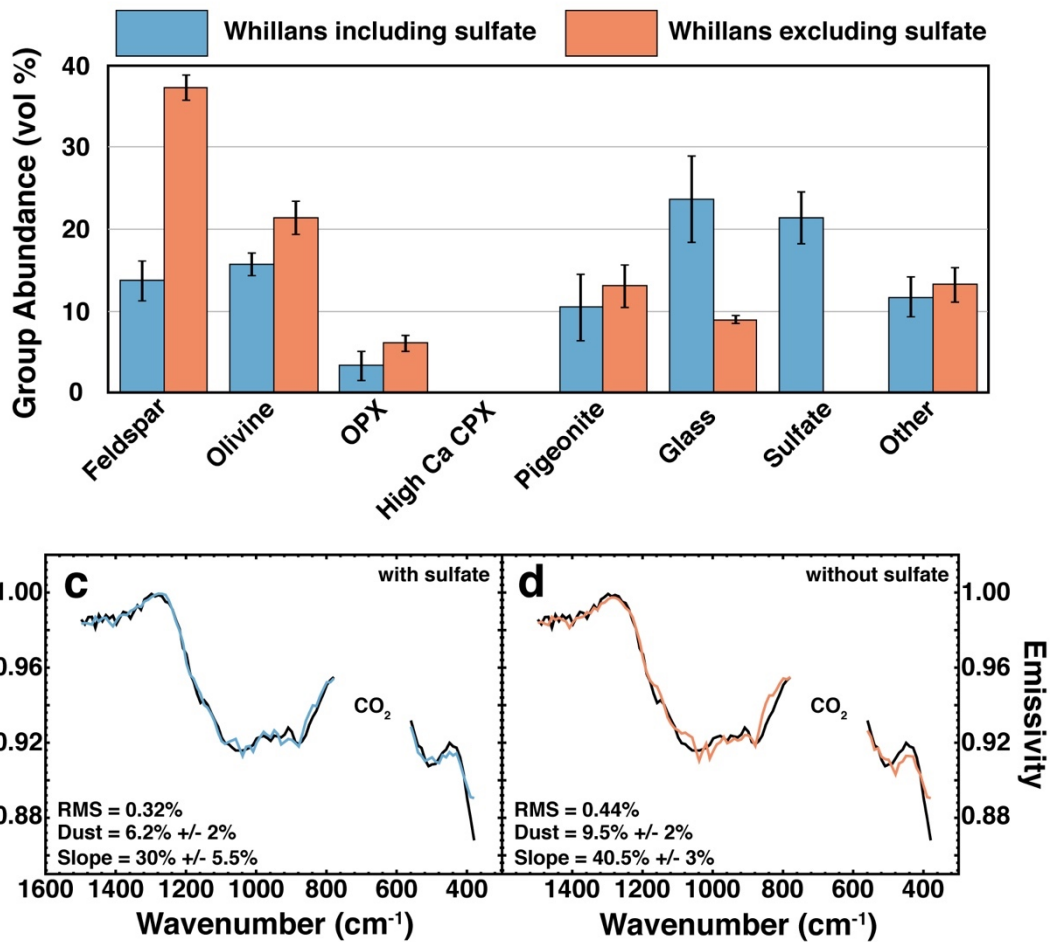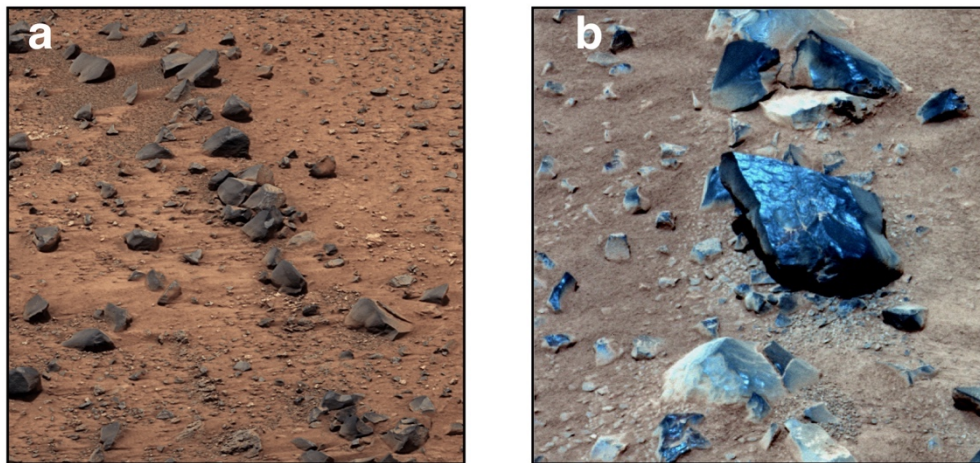
Figure 5.1. **a**) Pancam image of aligned Irvine rocks. **b**) Pancam image of Whillans. **c**) Spectrum of Whillans modeled with sulfate. Fit shown in blue. **d**) Spectrum of Whillans modeled without sulfate. Fit shown in red. The modeled mineral abundances of Whillans with and without sulfate minerals are shown in the middle table. Colors are correlated with the fit colors in c and d. Image credit: Savranksy and Bell, 2004; Bell et al., 2006. JPL/NASA

Irvine composition contains elevated Na_2O (2.68 wt. %) in addition to CaO (6.03 wt. %) and it is likely that an intermediate plagioclase feldspar is a significant component of the Irvine mineral assemblage. The spectral library contains eight representative plagioclase feldspar spectra covering the compositional range of bytownite, labradorite, oligoclase and albite. Additional feldspar minerals (andesine and anorthoclase) were added to the library to determine if additional feldspar compositions improve the modeled solution and no improvement was observed. It is likely that the albite misfit is due to the spectral library lacking a feldspar that wholly characterizes the features that the albite spectrum is attempting to fit. This could also be contributing to the over-estimation of sulfate, which has a strong absorption overlapping a prominent feldspar feature between 1200-1100 cm^{-1}.

For completeness, Figure 5.1 details the modeled mineralogy of Whillans using both libraries, but the discussion will focus on the mineralogy derived from the sulfate-free library. The modeled environmental components consist of Gusev dust (6 vol %) and a thermal slope (30 vol %). Figure 5.1b shows the Pancam image of Whillans collected in coordination with the Mini-TES observation. Small pools of surface dust are visible in troughs on the subconchoidally fractured surface, consistent with the minor modeled abundance of dust. The exterior of Whillans is comprised of multiple facets with variable exposure to sunlight likely leading to surfaces with different temperatures, consistent with the thermal slope observed in its spectrum. Mineralogically, the dominant modeled phase is plagioclase feldspar (37 vol %) consisting of labradorite (24.5 vol %) and lesser albite (12.5 vol %). Olivine is the most abundant ferromagnesian mineral (21 vol %) followed by the low-Ca clinopyroxene, pigeonite, (13 vol %), and orthopyroxene (6 vol %). Glass is modeled at 9 vol %. In addition to primary volcanic phases two secondary phases, zeolite and carbonate were modeled in low abundances and are grouped as 'other.'
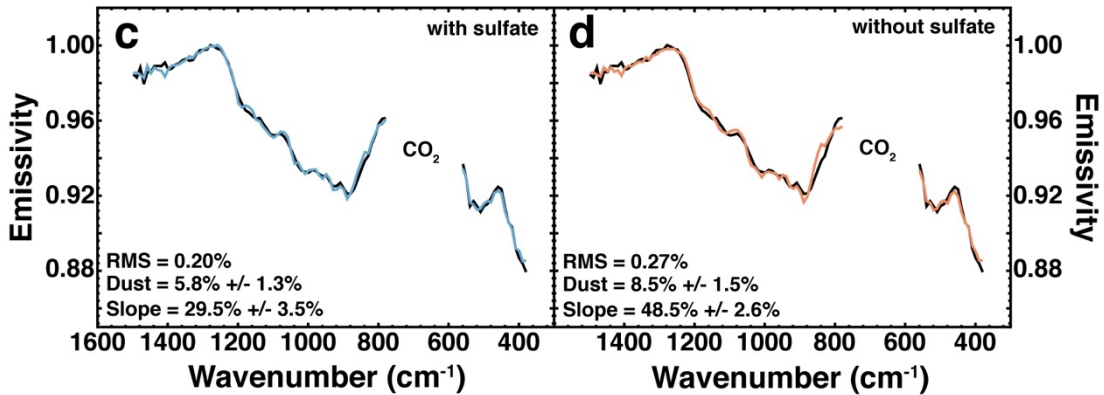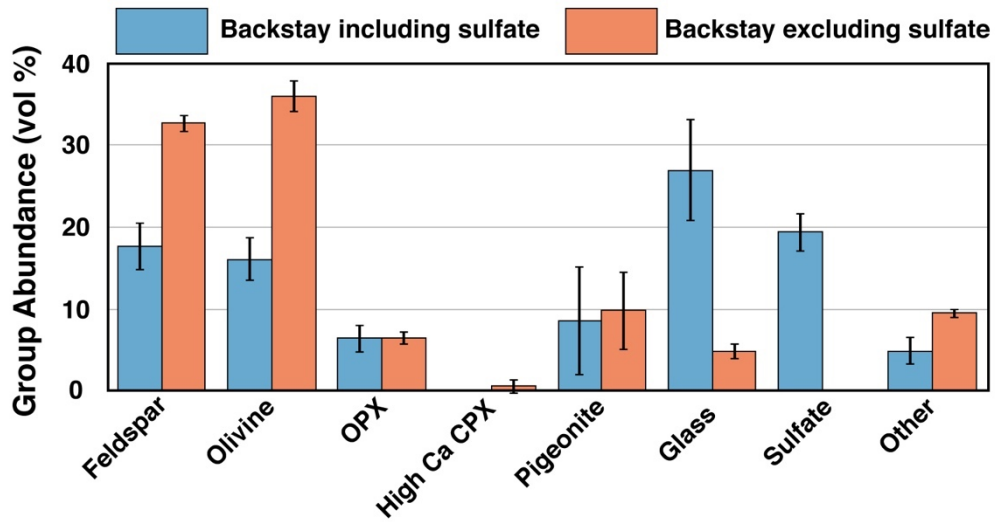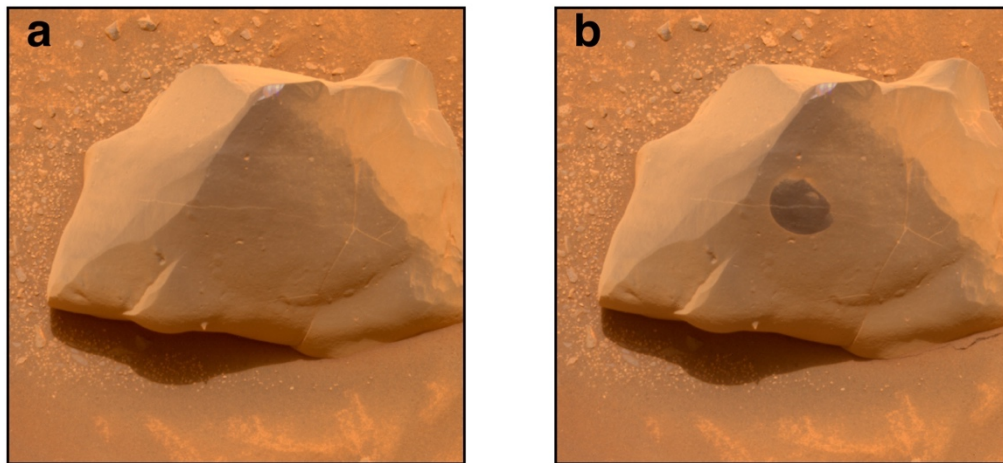
Figure 5.2. **a**) Pancam image Backstay **b**) Pancam image of Backstay after RAT brushing. **c**) Spectrum of Backstay modeled with sulfate. Model fit shown in blue. **d**) Spectrum of Backstay modeled without sulfate. Model fit shown in red. The modeled mineral abundances of Backstay with and without sulfate minerals are shown in the middle table. Colors are correlated with the fit colors in c and d. Image credit: Savransky and Bell, 2004; Bell et al., 2006. JPL/NASA

Mini-TES-Derived Mineralogy of Backstay. The spectrum of Backstay is well fit by the model using both libraries and every major spectral feature is reproduced. As previously observed, the modeled abundance of sulfate (19 vol%) is high compared to the APXS-measured SO_3 (1.52 wt. %) and the RMS error is improved (0.20% vs. 0.27%) using a library populated with sulfates. These models produce superior visual fits to the observed Backstay features than the model for Whillans and do not exhibit the sharp, mis-matched features between 1000-1040 cm^{-1}. As with Whillans, we will focus our discussion on the modeled mineralogy without sulfate.

The surface of Backstay has a coating of dust that is evident in Pancam images taken before and after Backstay was brushed with the rock abrasion tool's (RAT) brush (Fig. 5.2a & 5.2b). The modeled mineralogy includes average Gusev surface dust at 8.5 vol % that is in accordance with the observed dust deposit. Physically, Backstay shows a subconchoidally fractured surface with numerous facets. These facets and the dust coating are capable of producing the observed thermal slope (48.5 %) in the modeled mineralogy. Plagioclase feldspar is the dominant phase (33 vol %) represented by oligoclase (25.5 vol %) and labradorite (6 vol %) with minor albite (1 vol %). Similar to Whillans, the ferromagnesian minerals modeled in Backstay are olivine (36 vol %), pigeonite (9.8 vol %), and orthopyroxene (6.5 vol %). Minor high Ca pyroxene is modeled at <1 vol % and no Fe-Ti-Cr oxides are modeled. Carbonate is reported in the group 'other' and is modeled at 9.5 vol%.

MELTS phase equilibria. Figure 5.3 details the MELTS modeled abundance (vol %) of ferromagnesian and feldspar minerals occurring in Irvine and Backstay with increasing crystallinity (lower melt %) and varying fO_2. The modeled phase equilibria of the Irvine bulk composition show substantial variation with discrete stability fields for olivine, orthopyroxene and pigeonite. At ΔFMQ -6 to -5 the phase volume is dominated by orthopyroxene and pigeonite with lesser augite and olivine. Fe occurs

as Fe^0 metal in abundances <2.5 vol % and the ferromagnesian minerals exhibit high Mg# = (Mg/(Mg + Fe)) as Fe is preferentially sequestered in metal (Fig. 5.4).

From ΔFMQ -4 to 0 olivine is the dominant ferromagnesian mineral appearing throughout the crystallization sequence with a modest increase in Mg# with increasing fO_2 (Fig. 5.4). High Ca clinopyroxene appears late in the crystallization sequence at low abundance and orthopyroxene is absent throughout. Pigeonite begins crystallizing midway through the sequence and increases in abundance at the expense of olivine, potentially indicating the presence of an olivine $\rightarrow$ pigeonite reaction boundary (Grove and Juster, 1989; Juster et al., 1989). Fe^0 metal is not stable and magnetite is present with its abundance increasing with increasing fO_2.

Between ΔFMQ +1 and +3 pigeonite, orthopyroxene and high-Ca clinopyroxene are the dominant phases with olivine minor or absent. Over this range, the Mg# of the ferromagnesian minerals increases substantially with increasing fO_2 (Fig. 5.4). The stability of pigeonite is sensitive to fO2, at ΔFMQ >+1 it becomes unstable and is replaced by orthopyroxene and high-Ca pyroxene. Experimental studies demonstrate that pigeonite stability is sensitive to melt Mg#, where the minimum stability temperature is increased with increasing Mg# in the melt (Ishii, 1975; Lindsley, 1983). Below the minimum stability temperature of pigeonite, coexisting pyroxenes, augite and orthopyroxene, are stable, matching the observed MELTS mineral abundances. Under increasingly oxidizing conditions the Mg# of the melt is increased as more Fe is allocated to Fe_2O_3 driving the minimum stability temperature of pigeonite to higher temperature and forcing it out of stability.

For the Backstay composition, modeled mineral abundances are similar to Irvine but lack the dramatic variations in ferromagnesian mineral abundance. At fO_2 < ΔFMQ -5 orthopyroxene is the dominant ferromagnesian mineral with minor high-Ca

106

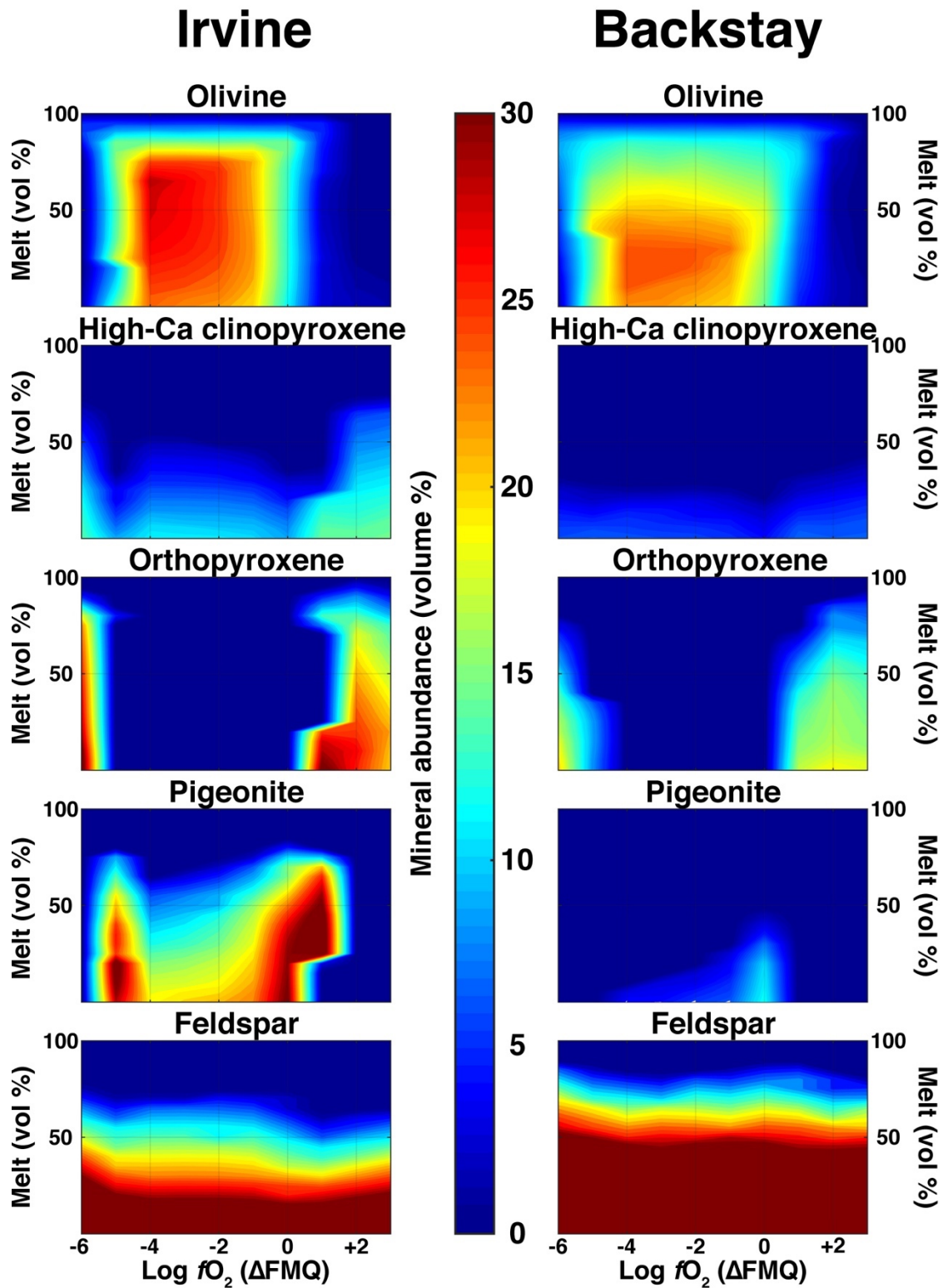*Figure 5.3.* MELTS derived modal mineral abundances plotted against fO₂ and melt fraction. Decreasing melt fraction indicates increasing crystalinity. All panels are scaled from 0-30 vol % and the color bar in the middle applies to all.
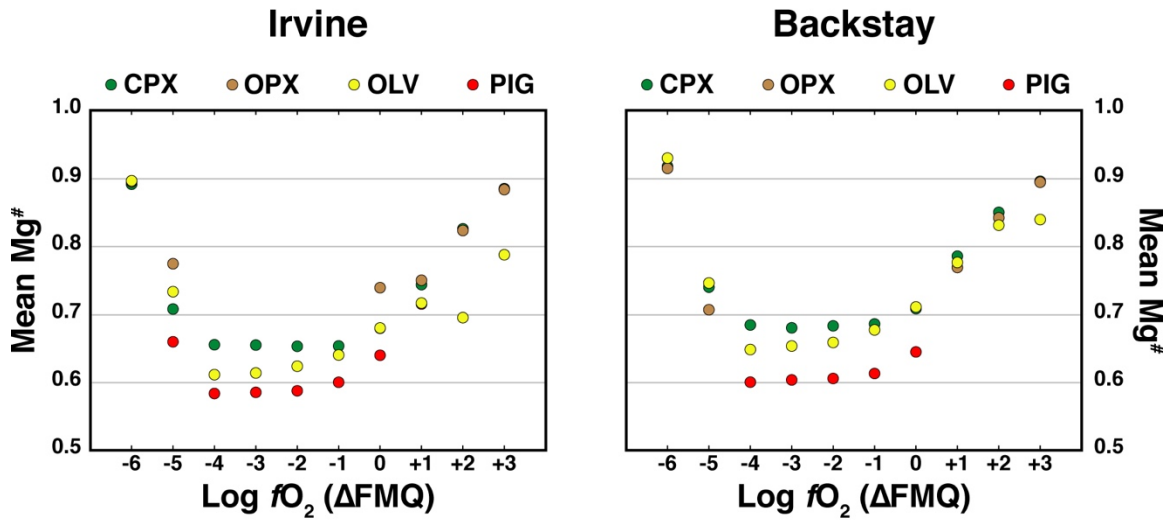
Figure 5.4. Ferromagnesian mineral Mg$^{\#}$ (Mg/(Mg+Fe)) averaged for each crystallization calculation. Fe^{0} metal appears at FMQ-5.

pyroxene and olivine present. Similar to Irvine, all ferromagnesian minerals exhibit high Mg#'s under reduced conditions due to the presence of Fe^0 metal (Fig. 5.4).

From ΔFMQ -4 to ΔFMQ 0 olivine predominates over late crystallizing pigeonite with minor high-Ca pyroxene and no orthopyroxene present. The Mg# of the ferromagnesian minerals is intermediate with a slight increase with increasing fO_2 (Fig. 5.4). Pigeonite is far less abundant in Backstay than in Irvine but shows a similar increase in abundance with diminishing olivine, likely indicating a similar olivine → pigeonite reaction boundary.

At fO_2 greater than ΔFMQ 0, orthopyroxene is the only ferromagnesian phase present, and the Mg# of the opx increases with increasing fO_2 (Fig. 5.4). The distinct pigeonite stability field observed in Irvine is not as evident in Backstay and pigeonite is not stable above ΔFMQ 0.

For both Irvine and Backstay, feldspar displays little variation in mode across the thermodynamically modeled conditions. The onset of feldspar crystallization begins earlier for Backstay and results in a mean abundance of 62 vol %. In contrast, Irvine begins crystallizing feldspar later and results in an abundance of 41 vol %.

MELTS synthetic spectra. RMS error values for fits of MELTS derived spectra to the Mini-TES observations are represented in Figure 5.5. The axes are identical to Figure 5.3 to allow for direct comparison to the modal mineral abundances that generated the spectrum. The MELTS-derived spectra of Irvine have minimal residual errors corresponding to an fO_2 between ΔFMQ -3 and -2, with a crystallinity of ~65%. The addition of a thermal slope expands the region of best fit to a bimodal distribution, where the distribution expands to cover FMQ -3 through 0 at ~65% crystallinity and a new mode lies at lower fO_2 (FMQ -5) and 75% crystallinity. Moreover, the addition of a slope results in lower residuals across the parameter space indicating that slope is a significant component of the observed Mini-TES spectrum. Average Gusev surface dust
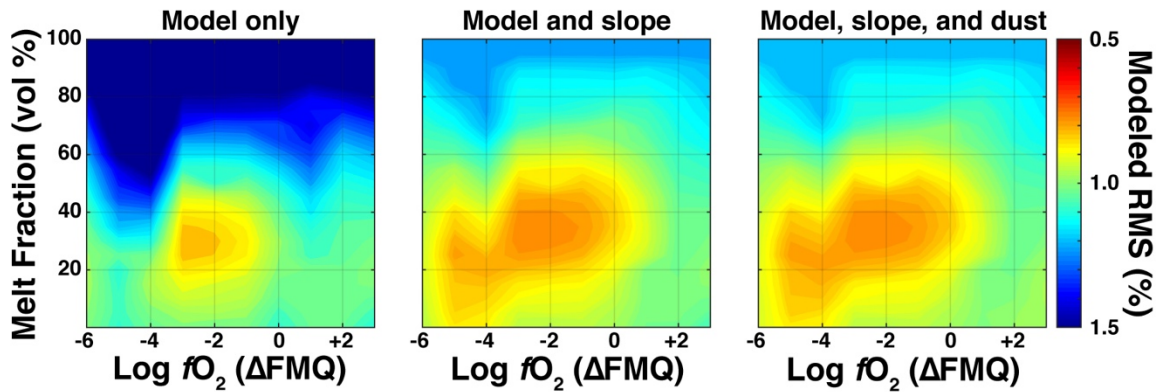
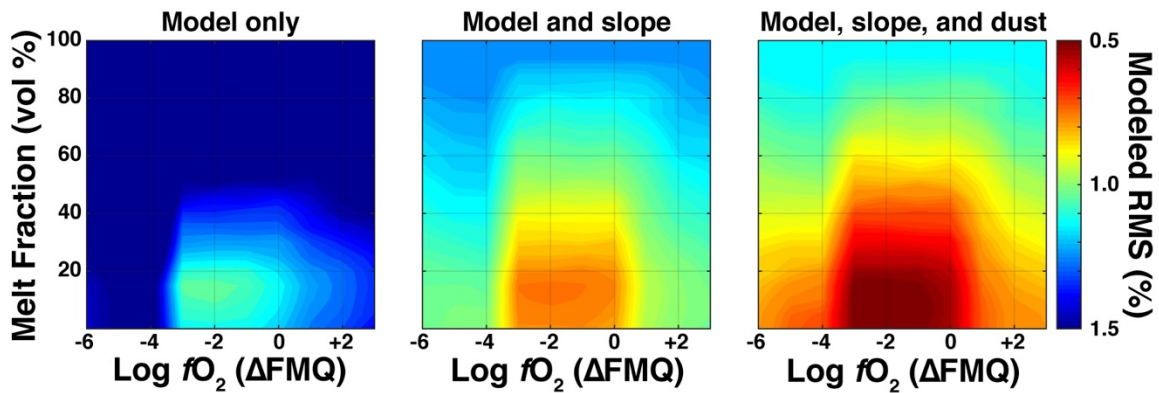*Figure 5.5.* RMS error of the fit for a MELTS-derived spectrum and Mini-TES observation. Left column shows results for the MELTS-derived spectrum by itself. Middle column shows results for MELTS-derived spectrum and a thermal slope. Right column shows MELTS-derived spectrum, slope and average spectrum of thick Gusev crater dust. X and Y axes are identical to figure 5.3 to allow for direct comparison.

does not significantly reduce the RMS over the MELTS-derived spectrum and thermal slope alone indicating that dust is not as significant as thermal slope, in agreement with the spectral unmixing results.

The Irvine MELTS-derived spectra from the region of best fit display remarkable similarity to the Mini-TES derived spectrum (Fig. 5.6). On the high wavenumber side of the Si-O absorption the rounded feature (950-1100 cm^{-1}) present in Irvine is not sufficiently recreated by the MELTS-derived spectra. This region coincides with a critical absorption of plagioclase feldspar and may indicate that the spectral library does not properly represent the feldspar present in Irvine, consistent with the spectral unmixing results. The three small but diagnostic features between 850-950 cm^{-1} are reproduced in each spectrum with the feature near 870 cm^{-1} strengthening with increasing fO_2, correlated with increasingly abundant pigeonite. In the low wavenumber region (550-380 cm^{-1}) the MELTS-derived spectra exhibit absorptions near 500 and 400 cm^{-1} similar to those in Irvine, though the synthetic spectra have a well-defined trough at 400 cm^{-1}, whereas the Irvine spectrum shows a continuous drop in emissivity through the end of the spectral range covered (380 cm^{-1}). Visually, the best fit to the Mini-TES spectrum is generated from the MELTS calculation at ΔFMQ 0 with a crystallinity of 65%.

MELTS-derived spectra from the Backstay composition have a region of best fit corresponding to -3 to 0 ΔFMQ and ~90% crystallinity. The addition of slope and dust improves the RMS error across the parameter space, indicating that both components contribute significantly to the Mini-TES spectrum. The region of best fit does not expand with the inclusion of slope and dust and the RMS values are improved overall, when compared to the fits for the Irvine composition.

The Backstay Mini-TES observation and MELTS-derived spectra show a number of similar features. The spectral region from 1250 to 980 cm^{-1} in the Backstay Mini-
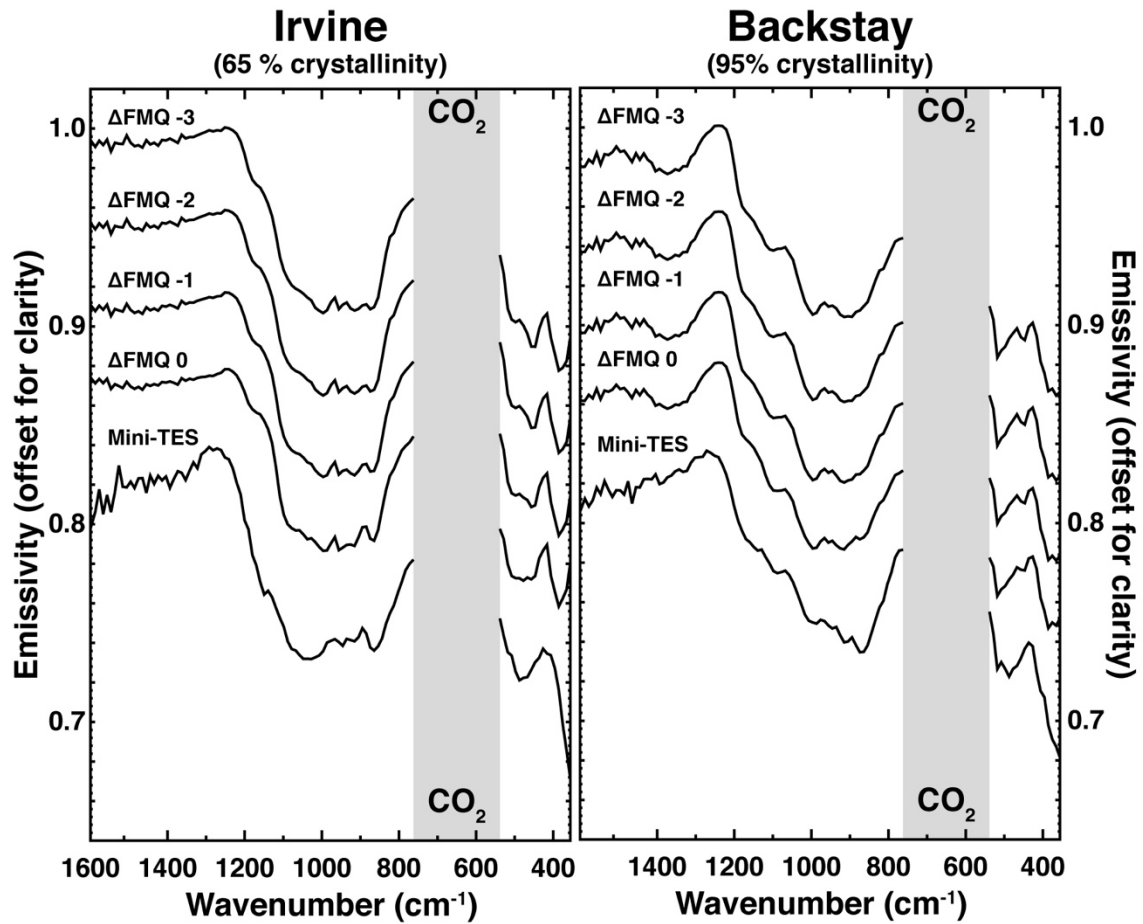
Figure 5.6. MELTS-derived spectra across the regions of best fit from figure 5.5. Grey bar indicates the region excluded due to strong absorption from atmospheric CO_2.

TES spectrum is strongly influenced by feldspar. Every MELTS-derived spectrum shown in Figure 5.6 recreates this feldspar feature, indicating that the MELTS algorithm and spectral library are representing the feldspar composition and abundance accurately. From 850-950 cm^{-1} only one spectrum (ΔFMQ 0) reproduces the positions of the observed Backstay spectral features. However, the strength of the absorption at 870 cm^{-1} is not reproduced by any MELTS-derived spectrum. This discrepancy could indicate that Backstay contains more pigeonite than the model predicts or that pigeonite is not well represented in the library. Poor representation of pigeonite in spectral libraries is a perennial deficiency that has been noted in numerous studies (Hamilton et al., 2000; Ruff et al., 2006; McSween et al., 2008; Rogers and Ahronson, 2008; Dyar et al., 2011). Across the low wavenumber region (550-380 cm^{-1}), the small, sharp absorption at 540 cm^{-1}, corresponding to feldspar, is present in each derived spectrum. The MELTS-derived spectra do not exhibit the second low wavenumber absorption near 510 cm^{-1} further indicating that a low Ca pyroxene (orthopyroxene or pigeonite) is not being adequately accounted for in either the MELTS algorithm or the spectral library used to generate the spectra.

Discussion

Reconciling Mini-TES, Mössbauer, and MELTS mineralogies. The MER Mössbauer spectrometer is capable of determining the relative distribution and oxidation state of Fe amongst the Fe-bearing phases present in a sample (Morris et al., 2006, 2008). However, Mössbauer data do not directly yield quantitative information about the modal proportions of Fe-bearing phases. Prior knowledge of the composition and density of the minerals within a sample is required to quantitatively determine their modal proportions (Dyar and Schaefer, 2004). As such, the mineral values reported for the Mössbauer spectrometer (Morris et al. 2006, 2008) represent fractions of Fe atoms within a crystallographic site, as opposed to weight or volume

percentages, and are not directly comparable to the Mini-TES derived mineralogy. While subtle variations in measured Mössbauer parameters indicate that there is a diversity of pyroxene compositions in Gusev crater, discrimination between specific compositions is not currently possible and all pyroxene is reported as a group (Morris et al., 2008). With these caveats in mind, the Mössbauer spectrometer is able to provide complementary qualitative constraints on the mineralogy derived from Mini-TES.

For the Irvine-class representative Whillans, the Mini-TES mineralogy shows approximately equal mineral proportions of olivine (21.4 ± 2.2 vol%) to pyroxene (19.2 ± 3.7 vol%) with no Fe-Ti-Cr oxide modeled. The favored pyroxene mineral in Mini-TES spectral unmixing solutions is pigeonite, whose presence is indicated by the prominent absorption at 870 cm^{-1} (Hamilton et al., 2000). Mössbauer data from Irvine-class rocks (Irvine, Esperanza, and Bu Zhou) indicate that Fe is distributed into pyroxene (41 ± 7 %), magnetite (45 ± 9 %), and minor olivine (6 ± 3 %; Morris et al., 2008). Taken together these data suggest that mafic minerals in Irvine-class rocks consist of pigeonite, olivine and magnetite. MELTS calculations for the Irvine bulk composition indicate that olivine dominates the early crystallizing assemblage from ΔFMQ -5 to 0 with pyroxene equaling and eventually exceeding its abundance late in the sequence. As fO_2 increases from ΔFMQ -5 to 0, the abundance of olivine decreases with increasing fO_2 with pigeonite exhibiting an apparent enrichment at the expense of olivine. Experimental investigations of ferro-basaltic system have shown that an olivine $\rightarrow$ pigeonite reaction boundary can exist within these systems under certain petrogenetic conditions (Grove and Juster, 1989; Juster et al., 1989; Toplis and Carrol, 1995). With increasing oxidation, spinel minerals (e.g. magnetite and titanomagnetite) become increasingly stable and form at the expense of olivine through the following general reaction (Toplis and Carrol, 1995);

114

$$3Fe_2SiO_4^{Ol} + O_2 \leftrightarrow 2Fe_3O_4^{Mt} + 3SiO_2^{Liq} \tag{1}$$
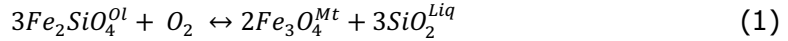
Silication of the melt occurs as this reaction proceeds to the right, where the increased activity of silica promotes pigeonite stability through:

$$Fe_2SiO_4^{Ol} + SiO_2^{Liq} \leftrightarrow 2FeSiO_3^{Pig} \tag{2}$$
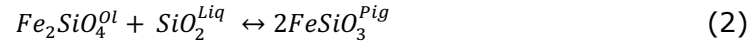
Equation 2 shows that when the activity of silica is increased, olivine resorption contributes to the Fe-Mg component of pigeonite. The interplay of these two reactions are the basis of the olivine → pigeonite reaction boundary and can explain the behavior of olivine and pigeonite in the MELTS calculations (Fig 5.3). The best visual fit for the MELTS-derived spectra lies on the edge of this boundary (ΔFMQ 0, 65 % crystallinity). Under increasingly oxidizing conditions the Mg# of the melt rises and pigeonite becomes unstable yielding two stable pyroxenes (orthopyroxene and augite) above ~ FMQ +1 to +2. Collectively the results from the Mini-TES, Mössbauer spectrometer, and MELTS calculations are consistent with the Irvine-class rocks crystallizing along the olivine → pigeonite reaction boundary, at an fO_2 above FMQ -2 but no greater than FMQ+2, with a best fit spectrum at FMQ. This range is in agreement with the updated range of primary fO_2 -0.2 to 0.8 for the Irvine class (Schmidt et al., 2013).

For Backstay, Mössbauer data show Fe distributed evenly between olivine (35 ± 2 %) and pyroxene (37 ± 2 %) and minor magnetite (11 ± 2 %) and ilmenite (3 ± 2 %). Mini-TES spectral mixture analysis of Backstay shows olivine (35.9 ± 2.0 vol %) dominant over pyroxene (16.9 ± 6.5 vol %) with pigeonite as the favored pyroxene mineral. These results are similar to the Irvine-class but indicate that pyroxene plays a much smaller role in the formation of Backstay-class rocks. The relative lack of pyroxene modeled in the Backstay composition emphasizes this relationship and further suggests a mineral assemblage consisting primarily of olivine. Compared to Irvine, the bulk composition of Backstay does not favor the formation of pigeonite. However, a similar but less dramatic olivine → pigeonite reaction boundary is apparent

in the MELTS modeled mineral abundances, occurring late in the crystallization sequence between FMQ -4 and 0 with pigeonite disappearing from the crystallizing assemblage above FMQ (Fig. 5.3). The region of best fit for the MELTS-derived spectra overlaps the olivine → pigeonite reaction boundary with the best visual fit occurring at FMQ with a crystallinity of ~90% (Figs. 5.5 and 5.6). These results indicate that Backstay also crystallized along an olivine → pigeonite reaction boundary with an fO_2 greater than FMQ -4 but no greater than FMQ. The range of fO_2 indicated by Mini-TES and MELTS is also in agreement with the updated primary fO_2 range for Backstay of ΔFMQ -3.3 to -2.0, though the best visual fit is 2 log units above the updated upper range (Schmidt et al., 2013).

Conclusions:

Mirror-dust corrected Mini-TES spectra allow for the derivation of modal mineralogies of the Irvine and Backstay-class rocks. Discrepancies between solutions using a library populated with sulfates versus a library without indicate that at least one component present in the Mini-TES spectra is not well represented in the spectral library. This deficiency is most apparent in the modeled spectrum of Whillans and preliminary investigation indicates that feldspar is a possible suspect. Notwithstanding, Mini-TES mineralogies derived without sulfates provide results that are in good agreement with the results of the Mössbauer spectrometer and MELTS thermodynamic model. Whillans, of class Irvine, reveals a mineralogy consisting of abundant feldspar, subequal olivine and pyroxene with minor glass. The Backstay trachybasalt exhibits a feldspar dominated mineralogy with abundant olivine and minor pyroxene. The importance of the low -Ca clinopyroxene, pigeonite, to the spectral fits of both rocks is substantiated by its importance to their calculated phase equilibria. MELTS calculations of Irvine and Backstay bulk compositions reveal that the stability of ferromagnesian minerals exhibit considerable variation across a range of fO_2. This

116

variability can be detected in the spectral signatures of the mineral assemblages crystallized at varying $f\mathrm{O}_2$. Synthetic spectra derived from MELTS calculations provide reasonable fits to the Mini-TES spectrum and allow additional constraints to be placed on the primary $f\mathrm{O}_2$ of Irvine and Backstay based on modal mineralogy. Collectively, these results show that primary $f\mathrm{O}_2$ values of Irvine and Backstay are consistent with their updated estimates and are not as highly oxidized as recent studies assume. This investigation highlights the ability of thermal emission spectroscopy to derive whole rock mineral abundance and enable interpretation of petrogenetic histories. Moreover, the use of complementary suites of instruments such as the Athena science payload, enhances the capability of each individual instrument and provides a more complete geologic picture.

CHAPTER 6

Conclusions and Future Work

The work presented in this manuscript contributes to the interpretation of the petrology of planetary surfaces using remote sensing techniques. In the course of examining this topic, I have contributed to the understanding of secondary processes that modify carbonaceous meteorite parent bodies, developed spectral parameters capable of detecting thermally metamorphosed regolith on carbonaceous asteroids, characterized geochemical trends observed in the minerals of terrestrial volcanic rocks, stumbled upon an exceptionally interesting lunar spectral analog, and employed a thermodynamic modelling tool to reconcile the mineralogy of a unique set of Martian volcanic rocks.

Collectively chapters 2 and 3 represent a comprehensive study of the mineralogical and spectral characteristics of one of the freshest carbonaceous meteorites on Earth. Rapid collection and curation allowed for the identification of extraterrestrial water-sensitive minerals that would otherwise have been removed through terrestrial weathering. Reconciling the presence of these minerals, CaS and $Ca(OH)_2$, with other petrographic observations led to the proposal of a unique formation mechanism. Heating on the asteroid parent body decomposed primitive organic materials and calcite yielding C, H and S-rich gases that interacted with CaO under reducing conditions to form the observed $Ca(OH)_2$ grains with CaS rims. Additional observations of the olivine-rich matrix provide supporting evidence that these materials saw a significant thermal event following their initial hydration. Observing that pyrolysis of primitive organics and dehydration of serpentine has occurred on CM chondrite parent bodies, a new science goal of identifying these materials on asteroid surfaces was set. An extensive spectral investigation of the Sutter's Mill meteorite was initiated with the intent of assisting the OSIRIS-REx mission

119

in the selection a pristine sampling site, by avoiding materials like Sutter's Mill. The result is a unique parameter, sinuosity, that is sensitive to absence of spectral feature observed in heated CM materials. Collectively, the results of these studies will be applied to data collected by the spacecraft in order to better understand the properties of the asteroid Bennu. While the work performed as part of this investigation of Sutter's Mill is sizeable, there are multiple future avenues of research. Characterizing the thermal emission spectra of Sutter's Mill materials will provide a truly complete spectral dataset that can be applied to the MapCam, OVIRIS, *and* OTES instruments. Additionally, an in-depth investigation of the role of oxygen fugacity on the stability of serpentine during heating is needed to better understand the spectral features of carbonaceous meteorites and asteroids. One of these investigations will be a scientific focus of my post-doctoral research here at ASU while I support the OSIRIS-REx Thermal Emission Spectrometer investigation.

In chapter 4, I explore a broad range of mineralogical, chemical and spectral observations of genetically related volcanic rocks. The aim of this investigation is to correlate spectral observations of volcanic rocks to the various stages of magmatic evolution. The Snake River Plain was selected for this investigation because the morphological style of volcanism expressed there has been observed on Mars and its intra-plate tectonic environment is more analogous to that expected on Mars; melts must ascend through a thick crust before they can be emplaced on the surface. Variations in the ascent path of this melt result in a diversity of volcanic rock types each of which has a unique story to tell written in the composition of its constituent minerals. Using thermal emission spectroscopy, I am able to determine the composition of the feldspar and olivine minerals present in each sample reasonably well and the observed trends in composition are parallel to those determined through electron microprobe analysis. These observed trends coupled with observations of the

position of Si-O vibrational absorption bands, which are sensitive to SiO_2 content, can yield information similar to common petrological discrimination diagrams (e.g. total alkalis vs. silica and alkali-iron-magnesium). Determinations of mineral chemistry and relative abundance using visible near infrared spectroscopy are complicated by the presence of strongly absorbing opaque minerals. However, this observation is indicative of a common magmatic trend where tholeiitic-style differentiation produces an enrichment in Fe resulting in ferrobasaltic rocks, like those observed at Craters of the Moon. Enrichment in Fe is paralleled by an enrichment in Ti and, if a ferrobasaltic melt is erupted with elevated Fe and Ti contents, ilmenite can saturate and deposit mantles of micron sized acicular crystals on the pre-existing phenocrysts. This behavior is observed in the COTM ferrobasalts and this petrographic texture causes ilmenite to dominate the reflectance spectrum of these rocks. Spectrally, they bear a striking resemblance to glassy pyroclastic deposits and melt breccias on the Moon and this investigation introduces these ferrobasalts as lunar analog materials. All told, the extensive investigations conducted in this chapter provide the groundwork for a career of intriguing spectral investigations. The ability of thermal emission spectroscopy to accurately determine the composition of feldspar minerals is impressive, though I think that it can be improved. A persistent question I have had during this research is whether or not the feldspars in the spectral library are representative of the feldspars in volcanic rocks. An in depth micro-spectroscopy investigation of the feldspars in COTM thin sections will go a long way in helping to answer this question.

In chapter 5, I revisit the Mini-TES spectra of two chemically distinct volcanic rocks from Gusev Crater, Mars. Initial derivations of mineralogy using Mini-TES were complicated by the deposition of dust on the instrument foreoptics. A robust correction for the spectral contribution of this thin layer of dust has been developed and applied to the MER Spirit Mini-TES data allowing for the reanalysis of this dataset. This is an

important contribution to the scientific investigation of Gusev crater because it allows researchers to revisit significant discoveries and make interpretations using the full Athena science payload, as originally intended. Using the mirror-dust-corrected Mini-TES spectra, I place constraints on the mineralogy of the Irvine and Backstay class rocks using linear least squares analyses. Irvine is a feldspathic rock with abundant pigeonite and minor olivine whereas Backstay is dominated by feldspar, olivine and lesser pigeonite. In addition to spectral analysis using traditional methods, I integrate thermal emission spectroscopy techniques and thermodynamic models resulting in the generation of hundreds of spectra that are each compositionally constrained to the bulk chemical observations made by the MER rover. This technique was employed to explore the stability of ferromagnesian minerals over a wide range of fO_2 to help place constraints on the formation conditions of these volcanic rocks. Though these calculations are likely oversimplified, this exercise has produced exciting and intriguing results. This technique can be applied to additional science questions including modelling the crystallization of the Adirondack class basalts of Gusev crater and the volcanic rocks of the Snake River Plain.

In my future work I will continue to build upon the skills that I have developed while conducting the studies within this volume. These individual investigations have refined my skillset and, though they appear to be a collection of unrelated topics, the experience gained from each provides both unique insight and transferrable knowledge. This has allowed me to approach scientific problems using a mixture of traditional and creative methods which has enhanced my ability to enjoy my job. While this can result in creative ways to fail, those too are informative.

REFERENCES

Adams, J. B., & McCord, T. B. (1970). Remote sensing of lunar surface mineralogy: Implications from visible and near-infrared reflectivity of Apollo 11 samples. Geochimica et Cosmochimica Acta Supplement, 1, 1937.

Agnihotri, R., Chauk, S.S., Mahuli, S.K., and Fan, L.S. (1999) Mechanism of CaO reaction with H_2S: Diffusion through CaS product layer. Chemical Engineering Science, 54, 3443-3453.

Aines, R. D., & Rossman, G. R. (1984). Water in minerals? A peak in the infrared. *Journal of Geophysical Research: Solid Earth*, *89*(B6), 4059-4071.

Akai, J. (1990) Mineralogical evidence of heating events in Antarctic carbonaceous chondrites, Y-86720 and Y-82162. Antarctic Meteorite Research, 3, 55.

Akai, J. (1992) TTT diagram of serpentine and saponite, and estimation of metamorphic heating degree of Antarctic carbonaceous chondrites. Antarctic Meteorite Research, 5, 120.

Anders, E. and Grevesse, N. (1989) Abundances of the elements: Meteoritic and solar. Geochimica et Cosmochimica Acta, 53, 197-214.

Arndt, J., & Engelhardt, W. V. (1987). Formation of Apollo 17 orange and black glass beads. Journal of Geophysical Research: Solid Earth, 92(B4).

Barber, D. J. (1981). Matrix phyllosilicates and associated minerals in C2M carbonaceous chondrites. *Geochimica et Cosmochimica Acta*, *45*(6), 945-970.

Bas, M. L., Maitre, R. L., Streckeisen, A., Zanettin, B., & IUGS Subcommission on the Systematics of Igneous Rocks. (1986). A chemical classification of volcanic rocks based on the total alkali-silica diagram. Journal of petrology, 27(3), 745-750.

Bell III, J. F., Izenberg, N. I., Lucey, P. G., Clark, B. E., Peterson, C., Gaffey, M. J., ... & Warren, J. (2002). Near-IR reflectance spectroscopy of 433 Eros from the NIS instrument on the NEAR mission: I. Low phase angle observations. *Icarus*, *155*(1), 119-144.

Bell, J. F., Joseph, J., Sohl-Dickstein, J. N., Arneson, H. M., Johnson, M. J., Lemmon, M. T., & Savransky, D. (2006). In-flight calibration and performance of the Mars Exploration Rover Panoramic Camera (Pancam) instruments. *Journal of Geophysical Research: Planets*, *111*(E2).

Bell, J. F., Squyres, S. W., Herkenhoff, K. E., Maki, J. N., Arneson, H. M., Brown, D., ... & Hayes, A. G. (2003). Mars exploration rover Athena panoramic camera (Pancam) investigation. *Journal of Geophysical Research: Planets*, *108*(E12).

Binzel, R. P., DeMeo, F. E., Burt, B. J., Cloutis, E. A., Rozitis, B., Burbine, T. H., ... & Howell, E. S. (2015). Spectral slope variations for OSIRIS-REx target Asteroid

(101955) Bennu: Possible evidence for a fine-grained regolith equatorial ridge. *Icarus*, *256*, 22-29.

Blazey, K. W. (1977). Optical absorption of MgO: Fe. *Journal of Physics and Chemistry of Solids*, *38*(6), 671-675.

Bonal, L., Quirico, E., Bourot-Denise, M., and Montagnac, G. (2006) Determination of the petrologic type of CV3 chondrites by Raman spectroscopy of included organic matter. Geochimica et Cosmochimica Acta, 70, 1849-1863.

Bouvier, A., & Wadhwa, M. (2010). The age of the Solar System redefined by the oldest Pb–Pb age of a meteoritic inclusion. *Nature geoscience*, *3*(9), 637.

Brearley, A., & Jones, A. (1998). Planetary Materials, chap. 3, MSA.

Brindley, G. W. & Zussman, J. (1957). A structural study of the thermal transformation of serpentine to forsterite *The American Mineralogist*, *42*, 461.

Brindley, G. W., & Hayami, R. (1963). Kinetics and mechanisms of dehydration and recrystallization of serpentine–I. *Clays and Clay minerals*, *12*, 35-47.

Brindley, G.W. and Hayami, R. (1965) Mechanism of formation of forsterite and enstatite from serpentine. Mineralogy Magazine, 35, 189-195

Browning, L.B., McSween, H.Y., and Zolensky, M.E. (1996) Correlated alteration effects in CM carbonaceous chondrites. Geochimica et Cosmochimica Acta, 60, 2621-2633.

Burgess, R., Wright, I.P., and Pillinger, C.T. (1991) Determination of sulphur‑bearing components in C1 and C2 carbonaceous chondrites by stepped combustion. Meteoritics, 26, 55-64.

Burns, R. G. (1993). *Mineralogical applications of crystal field theory* (Vol. 5). Cambridge University Press.

Calvin, W. M., & King, T. V. (1997). Spectral characteristics of iron-bearing phyllosilicates: Comparison to Orgueil (CI1), Murchison and Murray (CM2). *Meteoritics & Planetary Science*, *32*(5), 693-701.

Carmichael, I. S., & Ghiorso, M. S. (1990). The effect of oxygen fugacity on the redox state of natural liquids and their crystallizing phases. *Reviews in Mineralogy and Geochemistry*, *24*(1), 191-212.

Christensen, P. R., Bandfield, J. L., Hamilton, V. E., Howard, D. A., Lane, M. D., Piatek, J. L., ... & Stefanov, W. L. (2000). A thermal emission spectral library of rock-forming minerals. Journal of Geophysical Research: Planets, 105(E4), 9735-9739.

Christensen, P. R., Jakosky, B. M., Kieffer, H. H., Malin, M. C., McSween, H. Y., Nealson, K., ... & Ravine, M. (2004). The thermal emission imaging system (THEMIS) for the Mars 2001 Odyssey mission. Space Science Reviews, 110(1-2), 85-130.

Christensen, P. R., McSween Jr, H. Y., Bandfield, J. L., Ruff, S. W., Rogers, A. D., Hamilton, V. E., ... & Malin, M. C. (2005). Evidence for magmatic evolution and diversity on Mars from infrared observations. Nature, 436(7050), 504.

Christensen, P. R., Mehall, G. L., Silverman, S. H., Anwar, S., Cannon, G., Gorelick, N., ... & Fortuna, T. (2003). Miniature thermal emission spectrometer for the Mars exploration rovers. *Journal of Geophysical Research: Planets*, *108*(E12).

Clark, B. E., Binzel, R. P., Howell, E. S., Cloutis, E. A., Ockert-Bell, M., Christensen, P., ... & Soderberg, A. (2011). Asteroid (101955) 1999 RQ36: Spectroscopy from 0.4 to 2.4 μm and meteorite analogs. *Icarus*, *216*(2), 462-475.

Clark, B. E., Helfenstein, P., Bell III, J. F., Peterson, C., Veverka, J., Izenberg, N. I., ... & McFadden, L. (2002). NEAR infrared spectrometer photometry of Asteroid 433 Eros. *Icarus*, *155*(1), 189-204.

Clark, R. N. (1983). Spectral properties of mixtures of montmorillonite and dark carbon grains: Implications for remote sensing minerals containing chemically and physically adsorbed water. *Journal of Geophysical Research: Solid Earth*, *88*(B12), 10635-10644.

Clark, R. N., Curchin, J. M., Hoefen, T. M., & Swayze, G. A. (2009). Reflectance spectroscopy of organic compounds: 1. Alkanes. *Journal of Geophysical Research: Planets*, *114*(E3).

Clark, R. N., King, T. V., Klejwa, M., Swayze, G. A., & Vergo, N. (1990). High spectral resolution reflectance spectroscopy of minerals. *Journal of Geophysical Research: Solid Earth*, *95*(B8), 12653-12680.

Cloutis, E. A., Gaffey, M. J., & Moslow, T. F. (1994). Spectral reflectance properties of carbon-bearing materials. *Icarus*, *107*(2), 276-287.

Cloutis, E. A., Gaffey, M. J., Smith, D. G., & Lambert, R. S. J. (1990). Reflectance spectra of mafic silicate-opaque assemblages with applications to meteorite spectra. *Icarus*, *84*(2), 315-333.

Cloutis, E. A., Hiroi, T., Gaffey, M. J., Alexander, C. O. D., & Mann, P. (2011). Spectral reflectance properties of carbonaceous chondrites: 1. CI chondrites. *Icarus*, *212*(1), 180-209.

Cloutis, E. A., Hudon, P., Hiroi, T., & Gaffey, M. J. (2012). Spectral reflectance properties of carbonaceous chondrites 4: Aqueously altered and thermally metamorphosed meteorites. *Icarus*, *220*(2), 586-617.

Cloutis, E. A., Hudon, P., Hiroi, T., Gaffey, M. J., & Mann, P. (2011). Spectral reflectance properties of carbonaceous chondrites: 2. CM chondrites. *Icarus*, *216*(1), 309-346.

Cloutis, E. A., McCormack, K. A., Bell III, J. F., Hendrix, A. R., Bailey, D. T., Craig, M. A., ... & Riner, M. A. (2008). Ultraviolet spectral reflectance properties of common planetary minerals. *Icarus*, *197*(1), 321-347.

Court, R.W. and Sephton, M.A. (2014) New estimates of the production of volatile gases from ablating carbonaceous micrometeoroids at Earth and Mars during an E-belt-type Late Heavy Bombardment. Geochimica et Cosmochimica Acta, 145, 175-205.

Court, R.W. and Tan, J. (2016) Insights into secondary reactions occurring during atmospheric ablation of micrometeoroids. Meteoritics and Planetary Science, 51, 1163-1183.

de Leuw, S., Rubin, A.E., and Wasson, J.T. (2010) Carbonates in CM chondrites: Complex formational histories and comparison to carbonates in CI chondrites. Meteoritics and Planetary Science, 45, 513-530.

Dubina, E., Korat, L., Black, L., Strupi-Šuput, J., and Plank, J. (2013) Influence of water vapour and carbon dioxide on free lime during storage at 80 C, studied by Raman spectroscopy. Spectrochimica Acta Part A: Molecular and Biomolecular Spectroscopy, 111, 299-303.

Dubina, E., Wadsö, L., and Plank, J. (2011) A sorption balance study of water vapour sorption on anhydrous cement minerals and cement constituents. Cement and Concrete Research, 41, 1196-1204.

Dyar, M. D., & Schaefer, M. W. (2004). Mössbauer spectroscopy on the surface of Mars: constraints and expectations. *Earth and Planetary Science Letters*, *218*(3-4), 243-259.

Dyar, M. D., Glotch, T. D., Lane, M. D., Wopenka, B., Tucker, J. M., Seaman, S. J., ... & Pieters, C. (2011). Spectroscopy of Yamato 984028. *Polar Science*, *4*(4), 530-549.

Ebel, D.S. and Hill, M. (2012) Computed Tomography (CT) of five samples of the Sutter's Mill CM2 chondrite. (Online). Available: http://digitallibrary.amnh.org/handle/2246/6408 (accessed July 7, 2016). American Museum of Natural History, New York, New York.

Elvis, M. (2013) Prospecting asteroid resources. In Asteroids: Prospective energy and material resources. P. 81-129 Springer Berlin Heidelberg.

Feely, K. C., & Christensen, P. R. (1999). Quantitative compositional analysis using thermal emission spectroscopy: Application to igneous and metamorphic rocks. Journal of Geophysical Research: Planets, 104(E10), 24195-24210.

French, B. M. (1964). Graphitization of organic material in a progressively metamorphosed Precambrian iron formation. *Science*, *146*(3646), 917-918.

Fries, M., Le Corre, L., Hankey, M., Fries, J., Matson, R., Schaefer, J., and Reddy, V. (2014) Detection and rapid recovery of the Sutter's Mill meteorite fall as a model for future recoveries worldwide. Meteoritics and Planetary Science, 49, 1989-1996.

Fuchs, L. H., Olsen, E., & Jensen, K. J. (1973). Mineralogy, mineral-chemistry, and composition of the Murchison (C2) meteorite.

Fujiya, W., Sugiura, N., Marrocchi, Y., Takahata, N., Hoppe, P., Shirai, K., Sano, Y., and Hiyagon, H. (2015) Comprehensive study of carbon and oxygen isotopic compositions, trace element abundances, and cathodoluminescence intensities of calcite in the Murchison CM chondrite. Geochimica et Cosmochimica Acta 161, 101-117.

Galan, I., Glasser, F.P., and Andrade, C. (2013) Calcium carbonate decomposition. Journal of Thermal Analysis and Calorimetry, 111, 1197-1202.

Garvie, L.A.J. (2013) Mineralogy of the Sutter's Mill Carbonaceous Chondrite. 44th Lunar and Planetary Science Conference, Abstract #2148.

Ghiorso, M. S., & Sack, R. O. (1995). Chemical mass transfer in magmatic processes IV. A revised and internally consistent thermodynamic model for the interpolation and extrapolation of liquid-solid equilibria in magmatic systems at elevated temperatures and pressures. *Contributions to Mineralogy and Petrology*, *119*(2-3), 197-212.

Gibson Jr, E. K., & Johnson, S. M. (1972). Thermogravimetric-quadrupole mass-spectrometric analysis of geochemical samples. *Thermochimica Acta*, *4*(1), 49-56.

Gibson, E.K. Jr. (1974a) Inorganic gas release studies and thermal analysis investigations on carbonaceous chondrites. Meteoritics, 9, 343-344.

Gibson, E.K., Moore, G.W., and Johnson, S.M. (1974b) Summary of analytical data from gas release investigations, volatilization experiments, elemental abundance measurements on lunar samples, meteorites, minerals, volcanic ashes and basalts. NASA L.B. Johnson Space Center, Houston, Tex.

Goodrich, C. A., Herd, C. D., & Taylor, L. A. (2003). Spinels and oxygen fugacity in olivine-phyric and lherzolitic shergottites. *Meteoritics & Planetary Science*, *38*(12), 1773-1792.

Greeley, R. (1982). The Snake River Plain, Idaho: representative of a new category of volcanism. Journal of Geophysical Research: Solid Earth, 87(B4), 2705-2712.

Greeley, R., & King, J. S. (1977). Volcanism of the Eastern Snake River Plain, Idaho: A comparative planetary geology-guidebook. http://www. sti. nasa. gov/RECONselect. html.

Grossman, L., Beckett, J.R., Fedkin, A.V., Simon, S.B. and Ciesla, F.J. (2008) Redox conditions in the solar nebula: Observational, experimental, and theoretical constraints. Reviews in Mineralogy and Geochemistry, 68, 93-140.

Grove, T. L., & Juster, T. C. (1989). Experimental investigations of low-Ca pyroxene stability and olivine-pyroxene-liquid equilibria at 1-atm in natural basaltic and andesitic liquids. *Contributions to Mineralogy and Petrology*, *103*(3), 287-305.

Gualtieri, A. F., Giacobbe, C., & Viti, C. (2012). The dehydroxylation of serpentine group minerals. *American Mineralogist*, *97*(4), 666-680.

Haberle, C. W., & Garvie, L. A. (2017). Extraterrestrial formation of oldhamite and portlandite through thermal metamorphism of calcite in the Sutter's Mill carbonaceous chondrite. *American Mineralogist*, *102*(12), 2415-2421.

Haberle, C.W., Garvie, L.A.J, Domanick, K., and Christensen, P.R. (2014) Mineralogical complexity of altered kamacite in Sutter's Mill (SM3, pre-rain): insights into asteroidal dehydration. 45th Lunar and Planetary Science Conference, Abstract #2818

Hamilton, V. E. (2010). Thermal infrared (vibrational) spectroscopy of Mg–Fe olivines: A review and applications to determining the composition of planetary surfaces. Chemie der Erde-Geochemistry, 70(1), 7-33.

Hamilton, V. E., & Ruff, S. W. (2012). Distribution and characteristics of Adirondack-class basalt as observed by Mini-TES in Gusev crater, Mars and its possible volcanic source. Icarus, 218(2), 917-949.

Hamilton, V. E., & Ruff, S. W. (2012). Distribution and characteristics of Adirondack-class basalt as observed by Mini-TES in Gusev crater, Mars and its possible volcanic source. *Icarus*, *218*(2), 917-949.

Hansen, P., Dam-Johansen, K., and Østergaard, K. (1993) High-temperature reaction between sulphur dioxide and limestone—V. The effect of periodically changing oxidizing and reducing conditions. Chemical Engineering Science, 48, 1325-1341.

Hauber, E., Bleacher, J., Gwinner, K., Williams, D., & Greeley, R. (2009). The topography and morphology of low shields and associated landforms of plains volcanism in the Tharsis region of Mars. Journal of Volcanology and Geothermal Research, 185(1-2), 69-95.

Henderson, A. O. (2015). Low-Shield Volcanism: A Comparison of Volcanoes on Syria Planum, Mars and Snake River Plain, Idaho.

Herd, C. D., Borg, L. E., Jones, J. H., & Papike, J. J. (2002). Oxygen fugacity and geochemical variations in the martian basalts: Implications for martian basalt petrogenesis and the oxidation state of the upper mantle of Mars. *Geochimica et Cosmochimica Acta*, *66*(11), 2025-2036.

Herd, C. D., Papike, J. J., & Brearley, A. J. (2001). Oxygen fugacity of martian basalts from electron microprobe oxygen and TEM-EELS analyses of Fe-Ti oxides. *American Mineralogist*, *86*(9), 1015-1024.

Herkenhoff, K. E., Squyres, S. W., Arvidson, R., Bass, D. S., Bell, J. F., Bertelsen, P., ... & Johnson, J. R. (2004). Textures of the soils and rocks at Gusev Crater from Spirit's Microscopic Imager. *Science*, *305*(5685), 824-826.

Hiroi, T., Pieters, C. M., & Noble, S. K. (2000). Improved scheme of modified Gaussian deconvolution for reflectance spectra of lunar soils.

Hiroi, T., Pieters, C. M., Zolensky, M. E., & Lipschutz, M. E. (1994). Possible thermal metamorphism on the C, G, B, and F asteroids detected from their reflectance

spectra in comparison with carbonaceous chondrites. *Antarctic Meteorite Research*, *7*, 230.

Hiroi, T., Zolensky, M. E., Pieters, C. M., & Lipschutz, M. E. (1996). Thermal metamorphism of the C, G, B, and F asteroids seen from the 0.7 μm, 3 μm, and UV absorption strengths in comparison with carbonaceous chondrites. *Meteoritics & Planetary Science*, *31*(3), 321-327.

Howard, K. T., Benedix, G. K., Bland, P. A., & Cressey, G. (2009). Modal mineralogy of CM2 chondrites by X-ray diffraction (PSD-XRD). Part 1: Total phyllosilicate abundance and the degree of aqueous alteration. *Geochimica et Cosmochimica Acta*, *73*(15), 4576-4589.

Howard, K. T., Benedix, G. K., Bland, P. A., & Cressey, G. (2011). Modal mineralogy of CM chondrites by X-ray diffraction (PSD-XRD): Part 2. Degree, nature and settings of aqueous alteration. *Geochimica et Cosmochimica Acta*, *75*(10), 2735-2751.

Hughes, S. S., Smith, R. P., Hackett, W. R., & Anderson, S. R. (1999). Mafic volcanism and environmental geology of the eastern Snake River Plain, Idaho. Guidebook to the geology of eastern Idaho: Idaho Museum of Natural History, 143-168.

Ikeda, Y. (1992). An overview of the research consortium," Antarctic carbonaceous chondrites with CI affinities, Yamato-86720, Yamato-82162, and Belgica-7904". *Antarctic Meteorite Research*, *5*, 49.

Irvine, T. N. J., & Baragar, W. R. A. F. (1971). A guide to the chemical classification of the common volcanic rocks. Canadian journal of earth sciences, 8(5), 523-548.

Isaacson, P. J., Sarbadhikari, A. B., Pieters, C. M., Klima, R. L., Hiroi, T., Liu, Y., & Taylor, L. A. (2011). The lunar rock and mineral characterization consortium: Deconstruction and integrated mineralogical, petrologic, and spectroscopic analyses of mare basalts. Meteoritics & Planetary Science, 46(2), 228-251.

Ishii, T. (1975). The relations between temperature and composition of pigeonite in some lavas and their application to geothermometry. *Mineralogical Journal*, *8*(1), 48-57.

Ivanova, M.A., Lorenz, C.A., Nazarov, M.A., Brandstaetter, F., Franchi, I.A., Moroz, L.V., Clayton, R.N., and Bychkov, A.Y. (2010) Dhofar 225 and Dhofar 735: Relationship to CM2 chondrites and metamorphosed carbonaceous chondrites, Belgica-7904 and Yamato-86720. Meteoritics and Planetary Science, 45, 1108-1123.

Jenniskens, P., Fries, M. D., Yin, Q. Z., Zolensky, M., Krot, A. N., Sandford, S. A., ... & Nagashima, K. (2012). Radar-enabled recovery of the Sutter's Mill meteorite, a carbonaceous chondrite regolith breccia. *Science*, *338*(6114), 1583-1587.

Johnson, C.A. and Prinz, M. (1993) Carbonate compositions in CM and CI chondrites and implications for aqueous alteration. Geochimica et Cosmochimica Acta, 57, 2843-2852.

Johnson, D., Hooper, P., & Conrey, R. (1999). XRF Method XRF Analysis of Rocks and Minerals for Major and Trace Elements on a Single Low Dilution Li-Tetraborate Fused Bead. Advances in X-ray Analysis, 41, 843-867.

Johnson, T. V., & Fanale, F. P. (1973). Optical properties of carbonaceous chondrites and their relationship to asteroids. *Journal of Geophysical Research*, *78*(35), 8507-8518.

Juster, T. C., Grove, T. L., & Perfit, M. R. (1989). Experimental constraints on the generation of FeTi basalts, andesites, and rhyodacites at the Galapagos Spreading Center, 85 W and 95 W. Journal of Geophysical Research: Solid Earth, 94(B7), 9251-9274.

King, T. V., & Clark, R. N. (1989). Spectral characteristics of chlorites and Mg-serpentines using high-resolution reflectance spectroscopy. *Journal of Geophysical Research: Solid Earth*, *94*(B10), 13997-14008.

Klima, R. L., Dyar, M. D., & Pieters, C. M. (2011). Near-infrared spectra of clinopyroxenes: Effects of calcium content and crystal structure. Meteoritics & Planetary Science, 46(3), 379-395.

Klingelhoefer, G., Morris, R. V., Bernhardt, B., Rodionov, D., De Souza, P. A., Squyres, S. W., ... & Schröder, C. (2003). Athena MIMOS II Mössbauer spectrometer investigation. *Journal of Geophysical Research: Planets*, *108*(E12).

Krinov, E. L. (1969). The Meteoritical Bulletin, No. 48. *Meteoritics*

Kudłacz, K. and Rodriguez-Navarro, C. (2014) The mechanism of vapor phase hydration of calcium oxide: implications for CO_2 capture. Environmental Science and Technology, 48, 12411-12418.

Kuntz, M. A., Champion, D. E., Spiker, E. C., Lefebvre, R. H., & McBroome, L. A. (1982). The Great Rift and the evolution of the Craters of the Moon lava field, Idaho. Cenozoic Geology of Idaho: Idaho Bureau of Mines and Geology Bulletin, 26, 423-437.

Kuntz, M. A., Covington, H. R., & Schorr, L. J. (1992). An overview of basaltic volcanism of the eastern Snake River Plain, Idaho. Regional Geology of Eastern Idaho and Western Wyoming: Geological Society of America Memoir, 179, 227-267.

Lantz, C., Binzel, R. P., & DeMeo, F. E. (2018). Space weathering trends on carbonaceous asteroids: A possible explanation for Bennu's blue slope?. *Icarus*, *302*, 10-17.

Larimer, J.W. and Bartholomay, M. (1979) The role of carbon and oxygen in cosmic gases: Some applications to the chemistry and mineralogy of enstatite chondrites. Geochimica et Cosmochimica Acta, 43, 1455-1466.

Lauretta, D. S., Balram-Knutson, S. S., Beshore, E., Boynton, W. V., d'Aubigny, C. D., DellaGiustina, D. N., ... & Bennett, C. A. (2017). OSIRIS-REx: sample return from asteroid (101955) Bennu. *Space Science Reviews*, *212*(1-2), 925-984.

Le Maitre, R. W., Streckeisen, A., Zanettin, B., Le Bas, M. J., Bonin, B., & Bateman, P. (Eds.). (2005). Igneous rocks: a classification and glossary of terms: recommendations of the International Union of Geological Sciences Subcommission on the Systematics of Igneous Rocks. Cambridge University Press.

Lee, M.R., Lindgren, P., and Sofe, M.R. (2014) Aragonite, breunnerite, calcite and dolomite in the CM carbonaceous chondrites: High fidelity recorders of progressive parent body aqueous alteration. Geochimica et Cosmochimica Acta, 144, 126-156.

Leeman, W. P., Vitaliano, C. J., & Prinz, M. (1976). Evolved lavas from the snake river plain: craters of the moon national monument, Idaho. Contributions to Mineralogy and Petrology, 56(1), 35-60.

Lewis, J.S., McKay, D.S., and Clark, B.C. (1993) Using resources from near-Earth space. In Lewis J., Matthews M.S., Guerrieri M.L., Eds. Resources of Near-Earth Space, p.3-14, The University of Arizona Press, Tucson&London

Lindsley, D. H. (1983). Pyroxene thermometry. *American Mineralogist*, *68*(5-6), 477-493.

Loeffler, B. M., Burns, R. G., Johnson, K. H., Tossell, J. A., & Vaughan, D. J. (1974). Charge transfer in lunar materials-Interpretation of ultraviolet-visible spectral properties of the moon. In *Lunar and Planetary Science Conference Proceedings* (Vol. 5, pp. 3007-3016).

Lyon, R. J. P. (1965). Analysis of rocks by spectral infrared emission (8 to 25 microns). Economic Geology, 60(4), 715-736.

Materić, V., Ingham, B., and Holt, R. (2015) In situ synchrotron XRD investigation of the dehydration and high temperature carbonation of $Ca(OH)_2$. CrystEngComm, 17, 7306-7315.

Matza, S. D., & Lipschutz, M. E. (1977). Thermal metamorphism of primitive meteorites. VI-Eleven trace elements in Murchison C2 chondrite heated at 400-1000° C. In *Lunar and Planetary Science Conference Proceedings* (Vol. 8, pp. 161-176).

McCurry, M., Hayden, K. P., Morse, L. H., & Mertzman, S. (2008). Genesis of post-hotspot, A-type rhyolite of the Eastern Snake River Plain volcanic field by extreme fractional crystallization of olivine tholeiite. Bulletin of Volcanology, 70(3), 361-383.

McSween Jr, H. Y. (1979). Alteration in CM carbonaceous chondrites inferred from modal and chemical variations in matrix. *Geochimica et Cosmochimica Acta*, *43*(11), 1761-1770.

McSween, H. Y., Ruff, S. W., Morris, R. V., Bell, J. F., Herkenhoff, K., Gellert, R., ... & Christensen, P. R. (2006). Alkaline volcanic rocks from the Columbia Hills, Gusev crater, Mars. *Journal of Geophysical Research: Planets*, *111*(E9).

McSween, H. Y., Ruff, S. W., Morris, R. V., Gellert, R., Klingelhoefer, G., Christensen, P. R., ... & Rogers, A. D. (2008). Mineralogy of volcanic rocks in Gusev crater, Mars: Reconciling Mössbauer, Alpha Particle X-Ray Spectrometer, and Miniature Thermal Emission Spectrometer spectra. *Journal of Geophysical Research: Planets*, *113*(E6).

McSween, H.Y. (1979) Alteration in CM carbonaceous chondrites inferred from modal and chemical variations in matrix. Geochimica et Cosmochimica Acta, 43, 1761-1770.

Milliken, R. E., & Mustard, J. F. (2007). Estimating the water content of hydrated minerals using reflectance spectroscopy: I. Effects of darkening agents and low-albedo materials. *Icarus*, *189*(2), 550-573.

Ming, D. W., Gellert, R., Morris, R. V., Arvidson, R. E., Brueckner, J., Clark, B. C., ... & Klingelhoefer, G. (2008). Geochemical properties of rocks and soils in Gusev crater, Mars: Results of the Alpha Particle X-ray Spectrometer from Cumberland Ridge to Home Plate. *Journal of Geophysical Research: Planets*, *113*(E12).

Moroz, L., Schade, U., & Wäsch, R. (2000). Reflectance spectra of olivine–orthopyroxene-bearing assemblages at decreased temperatures: Implications for remote sensing of asteroids. *Icarus*, *147*(1), 79-93.

Morris, R. V., Klingelhoefer, G., Schröder, C., Fleischer, I., Ming, D. W., Yen, A. S., ... & Clark, B. C. (2008). Iron mineralogy and aqueous alteration from Husband Hill through Home Plate at Gusev crater, Mars: Results from the Mössbauer instrument on the Spirit Mars Exploration Rover. *Journal of Geophysical Research: Planets*, *113*(E12).

Morris, R. V., Klingelhoefer, G., Schröder, C., Rodionov, D. S., Yen, A., Ming, D. W., ... & Bernhardt, B. (2006). Mössbauer mineralogy of rock, soil, and dust at Gusev crater, Mars: Spirit's journey through weakly altered olivine basalt on the plains and pervasively altered basalt in the Columbia Hills. *Journal of Geophysical Research: Planets*, *111*(E2).

Morris, R. V., Rampe, E. B., Graff, T. G., Archer Jr, P. D., Le, L., Ming, D. W., & Sutter, B. (2015). Transmission X-ray diffraction (XRD) patterns relevant to the MSL CheMin amorphous component: Sulfates and silicates.

Morris, R. V., Vaniman, D. T., Blake, D. F., Gellert, R., Chipera, S. J., Rampe, E. B., ... & Yen, A. S. (2016). Silicic volcanism on Mars evidenced by tridymite in high-SiO2 sedimentary rock at Gale crater. Proceedings of the National Academy of Sciences, 113(26), 7071-7076.

Mustard, J. F., & Sunshine, J. M. (1995). Seeing through the dust: Martian crustal heterogeneity and links to the SNC meteorites. Science, 267(5204), 1623-1626.

Nakamura, T. (2005). Post-hydration thermal metamorphism of carbonaceous chondrites. *Journal of Mineralogical and Petrological Sciences*, *100*(6), 260-272.

Nekvasil, H., Dondolini, A., Horn, J., Filiberto, J., Long, H., & Lindsley, D. H. (2004). The origin and evolution of silica-saturated alkalic suites: an experimental study. Journal of Petrology, 45(4), 693-721.

Nekvasil, H., McCUBBIN, F. M., Harrington, A., Elardo, S., & Lindsley, D. H. (2009). Linking the Chassigny meteorite and the Martian surface rock Backstay: Insights into igneous crustal differentiation processes on Mars. *Meteoritics & Planetary Science*, *44*(6), 853-869.

Nekvasil, H., Simon, A., & Lindsley, D. H. (2000). Crystal fractionation and the evolution of intra-plate hy-normative igneous suites: insights from their feldspars. Journal of Petrology, 41(12), 1743-1757.

Noble, S. K., Pieters, C. M., Hiroi, T., & Taylor, L. A. (2006). Using the modified Gaussian model to extract quantitative data from lunar soils. Journal of Geophysical Research: Planets, 111(E11).

Nozaki, W., Nakamura, T. and Noguchi, T. (2006) Bulk mineralogical changes of hydrous micrometeorites during heating in the upper atmosphere at temperatures below 1000 C. Meteoritics and Planetary Science, 41, 1095-1114.

Oh, J.S., and Wheelock, T.D. (1990) Reductive decomposition of calcium sulfate with carbon monoxide: reaction mechanism. Industrial and Engineering Chemistry Research, 29, 544-550.

Okada, A., Keil, K., and Taylor, G.J. (1981) Unusual weathering products of oldhamite parentage in the Norton County enstatite achondrite. Meteoritics, 16, 141-152.

Piani, L., Marrocchi, Y., Libourel, G., and Tissandier, L. (2016) Magmatic sulfides in the porphyritic chondrules of EH enstatite chondrites. Geochimica et Cosmochimica Acta, 195, 84-99.

Pierce, K. L., Morgan, L. A., & Link, P. K. (1992). The track of the Yellowstone hot spot: Volcanism, faulting, and uplift. Regional geology of eastern Idaho and western Wyoming: Geological Society of America Memoir, 179(322), 1-53.

Pizzarello, S., & Garvie, L. A. (2014). Sutter's Mill dicarboxylic acids as possible tracers of parent-body alteration processes. *Meteoritics & Planetary Science*, *49*(11), 2087-2094.

Putirka, K. D., Kuntz, M. A., Unruh, D. M., & Vaid, N. (2009). Magma evolution and ascent at the craters of the moon and neighboring volcanic fields, Southern

Idaho, USA: implications for the evolution of polygenetic and monogenetic volcanic fields. Journal of Petrology, 50(9), 1639-1665.

Quirico, E., Montagnac, G., Rouzaud, J.N., Bonal, L., Bourot-Denise, M., Duber, S., and Reynard, B. (2009) Precursor and metamorphic condition effects on Raman spectra of poorly ordered carbonaceous matter in chondrites and coals. Earth and Planetary Science Letters, 287, 185-193.

Rabade, S., Barba, N., Garvie, L.A.J., and Thangavelautham, J. (2016) The case for solar thermal steam propulsion system for interplanetary travel: Enabling simplified ISRU utilizing NEOs and small bodies. 67th International Astronautical Congress, Abstract Code: IAC-16,D4,5,7,x34659

Ramsey, M. S., & Christensen, P. R. (1998). Mineral abundance determination: Quantitative deconvolution of thermal emission spectra. Journal of Geophysical Research: Solid Earth, 103(B1), 577-596.

Ray, D., & Shukla, A. D. (2017). The Mukundpura meteorite, a new fall of CM chondrite. *Planetary and Space Science*.

Reuter, D. C., Simon, A. A., Hair, J., Lunsford, A., Manthripragada, S., Bly, V., ... & Dolch, Z. (2018). The OSIRIS-REx visible and infrared spectrometer (OVIRS): spectral maps of the asteroid Bennu. *Space Science Reviews*, *214*(2), 54.

Rieder, R., Gellert, R., Brückner, J., Klingelhöfer, G., Dreibus, G., Yen, A., & Squyres, S. W. (2003). The new Athena alpha particle X-ray spectrometer for the Mars Exploration Rovers. *Journal of Geophysical Research: Planets*, *108*(E12).

Rizk, B., d'Aubigny, C. D., Golish, D., Fellows, C., Merrill, C., Smith, P., ... & DellaGiustina, D. N. (2018). OCAMS: the OSIRIS-REx camera suite. *Space Science Reviews*, *214*(1), 26.

Rodriguez-Navarro, C., Ruiz-Agudo, E., Luque, A., Rodriguez-Navarro, A.B., and Ortega-Huertas, M. (2009) Thermal decomposition of calcite: Mechanisms of formation and textural evolution of CaO nanocrystals. American Mineralogist, 94, 578-593.

Rogers, A. D., & Aharonson, O. (2008). Mineralogical composition of sands in Meridiani Planum determined from Mars Exploration Rover data and comparison to orbital measurements. Journal of Geophysical Research: Planets, 113(E6).

Rogers, A. D., & Nekvasil, H. (2015). Feldspathic rocks on Mars: Compositional constraints from infrared spectroscopy and possible formation mechanisms. Geophysical Research Letters, 42(8), 2619-2626.

Rowe, M. C., Ellis, B. S., & Lindeberg, A. (2012). Quantifying crystallization and devitrification of rhyolites by means of X-ray diffraction and electron microprobe analysis. *American Mineralogist*, *97*(10), 1685-1699.

Rubin, A. E., Trigo-Rodríguez, J. M., Huber, H., & Wasson, J. T. (2007). Progressive aqueous alteration of CM carbonaceous chondrites. *Geochimica et Cosmochimica Acta*, *71*(9), 2361-2382.

Rubin, A.E. (1997) Mineralogy of meteorite groups. Meteoritics and Planetary Science, 32, 231-247

Rubin, A.E., Trigo-Rodríguez, J.M., Huber, H., and Wasson, J.T. (2007) Progressive aqueous alteration of CM carbonaceous chondrites. Geochimica et Cosmochimica Acta, 71, 2361-2382

Ruff, S. W., & Hamilton, V. E. (2017). Wishstone to Watchtower: Amorphous alteration of plagioclase-rich rocks in Gusev crater, Mars. *American Mineralogist*, *102*(2), 235-251.

Ruff, S. W., Christensen, P. R., Barbera, P. W., & Anderson, D. L. (1997). Quantitative thermal emission spectroscopy of minerals: A laboratory technique for measurement and calibration. Journal of Geophysical Research: Solid Earth, 102(B7), 14899-14913.

Ruff, S. W., Christensen, P. R., Blaney, D. L., Farrand, W. H., Johnson, J. R., Michalski, J. R., ... & Squyres, S. W. (2006). The rocks of Gusev Crater as viewed by the Mini-TES instrument. *Journal of Geophysical Research: Planets*, *111*(E12).

Ruff, S. W., Farmer, J. D., Calvin, W. M., Herkenhoff, K. E., Johnson, J. R., Morris, R. V., ... & Squyres, S. W. (2011). Characteristics, distribution, origin, and significance of opaline silica observed by the Spirit rover in Gusev crater, Mars. *Journal of Geophysical Research: Planets*, *116*(E7).

Ruff, S.W., 1998. Quantitative Thermal Infrared Emission Spectroscopy Applied to Granitoid Petrology. Ph.D. Thesis, Arizona State University, 234 p.

Sack, R. O., Carmichael, I. S. E., Rivers, M. L., & Ghiorso, M. S. (1981). Ferric-ferrous equilibria in natural silicate liquids at 1 bar. *Contributions to Mineralogy and petrology*, *75*(4), 369-376.

Salisbury, J. W. (1987). Mid-infrared (2.1-25μm) spectra of minerals. *USGS Open File Report*, 87-263.

Santos, A. R., Agee, C. B., McCubbin, F. M., Shearer, C. K., Burger, P. V., Tartese, R., & Anand, M. (2015). Petrology of igneous clasts in Northwest Africa 7034: Implications for the petrologic diversity of the Martian crust. Geochimica et Cosmochimica Acta, 157, 56-85.

Sautter, V., Toplis, M. J., Wiens, R. C., Cousin, A., Fabre, C., Gasnault, O., ... & Bridges, J. C. (2015). In situ evidence for continental crust on early Mars. Nature Geoscience, 8(8), 605.

Savransky, D., & Bell, J. F. (2004, December). True color and chromaticity of the Martian surface and sky from Mars Exploration Rover Pancam observations. In *AGU Fall Meeting Abstracts*.

Schmid, T. and Dariz, P. (2015) Shedding light onto the spectra of lime: Raman and luminescence bands of CaO, Ca(OH)$_2$ and CaCO$_2$. Journal of Raman Spectroscopy, 46, 141-146.

Schmidt, M. E., Schrader, C. M., & McCoy, T. J. (2013). The primary fO2 of basalts examined by the Spirit rover in Gusev Crater, Mars: Evidence for multiple redox states in the Martian interior. *Earth and Planetary Science Letters*, *384*, 198-208.

Ševčík, R., Mácová, P., Sotiriadis, K., Pérez-Estébanez, M., Viani, A., and Šašek, P. (2016) Micro-Raman spectroscopy investigation of the carbonation reaction in a lime paste produced with a traditional technology. Journal of Raman Spectroscopy, 47, 1452-1457.

Smith, J. V., & Hervig, R. L. (1979). Shergotty meteorite: Mineralogy, petrography and minor elements. *Meteoritics & Planetary Science*, *14*(1), 121-142.

Smith, M. D., Wolff, M. J., Spanovich, N., Ghosh, A., Banfield, D., Christensen, P. R., ... & Squyres, S. W. (2006). One Martian year of atmospheric observations using MER Mini-TES. *Journal of Geophysical Research: Planets*, *111*(E12).

Smith, R. B., & Braile, L. W. (1994). The yellowstone hotspot. Journal of Volcanology and Geothermal Research, 61(3-4), 121-187.

Squyres, S. W., Arvidson, R. E., Bell, J. F., Brückner, J., Cabrol, N. A., Calvin, W., ... & Des Marais, D. J. (2004). The Spirit rover's Athena science investigation at Gusev crater, Mars. *science*, *305*(5685), 794-799.

Stanmore, B.R. and Gilot, P. (2005) Review—calcination and carbonation of limestone during thermal cycling for CO 2 sequestration. Fuel Processing Technology, 86, 1707-1743

Stout, M. Z., & Nicholls, J. (1977). Mineralogy and petrology of Quaternary lavas from the Snake River Plain, Idaho. Canadian Journal of Earth Sciences, 14(9), 2140-2156.

Stout, M. Z., Nicholls, J., & Kuntz, M. A. (1994). Petrological and mineralogical variations in 2500–2000 yr BP lava flows, Craters of the Moon lava field, Idaho. Journal of Petrology, 35(6), 1681-1715.

Sunshine, J. M., & Pieters, C. M. (1993). Estimating modal abundances from the spectra of natural and laboratory pyroxene mixtures using the modified Gaussian model. Journal of Geophysical Research: Planets, 98(E5), 9075-9087.

Sunshine, J. M., & Pieters, C. M. (1998). Determining the composition of olivine from reflectance spectroscopy. *Journal of Geophysical Research: Planets*, *103*(E6), 13675-13688.

Sunshine, J. M., Pieters, C. M., & Pratt, S. F. (1990). Deconvolution of mineral absorption bands: An improved approach. Journal of Geophysical Research: Solid Earth, 95(B5), 6955-6966.

Takir, D., Emery, J. P., Mcsween, H. Y., Hibbitts, C. A., Clark, R. N., Pearson, N., & Wang, A. (2013). Nature and degree of aqueous alteration in CM and CI carbonaceous chondrites. *Meteoritics & Planetary Science*, *48*(9), 1618-1637.

Tatsumoto, M., Knight, R. J., & Allegre, C. J. (1973). Time differences in the formation of meteorites as determined from the ratio of lead-207 to lead-206. *Science*, *180*(4092), 1279-1283.

Tomeoka, K. (1990) Mineralogy and petrology of Belgica-7904: A new kind of carbonaceous chondrite from Antarctica. Antarctic Meteorite Research, 3, 40.

Tomeoka, K., & Buseck, P. R. (1985). Indicators of aqueous alteration in CM carbonaceous chondrites: Microtextures of a layered mineral containing Fe, S, O and Ni. *Geochimica et Cosmochimica Acta*, *49*(10), 2149-2163.

Tomeoka, K., Kojima, H., & Yanai, K. (1989). Yamato-86720: A CM carbonaceous chondrite having experienced extensive aqueous alteration and thermal metamorphism.

Tomeoka, K., Kojima, H., and Yanai, K. (1989a) Yamato-86720: A CM carbonaceous chondrite having experienced extensive aqueous alteration and thermal metamorphism. In Proceedings of the NIPR Symposium on Antarctic Meteorites, 2, 55-74.

Tomeoka, K., Kojima, H., and Yanai, K. (1989b) Yamato-82162: A new kind of CI carbonaceous chondrite found in Antarctica. In Proceedings of the NIPR Symposium on Antarctic Meteorites, 2, 36-54.

Tompkins, S., & Pieters, C. M. (2010). Spectral characteristics of lunar impact melts and inferred mineralogy. Meteoritics & Planetary Science, 45(7), 1152-1169.

Tonui, E., Zolensky, M., Hiroi, T., Nakamura, T., Lipschutz, M. E., Wang, M. S., & Okudaira, K. (2014). Petrographic, chemical and spectroscopic evidence for thermal metamorphism in carbonaceous chondrites I: CI and CM chondrites. *Geochimica et Cosmochimica Acta*, *126*, 284-306.

Tonui, E., Zolensky, M., Lipschutz, M., Wang, M., and Nakamura, T. (2003) Yamato 86029: Aqueously altered and thermally metamorphosed CI-like chondrite with unusual textures. Meteoritics and Planetary Science, 38, 269-292

Tuff, J., Wade, J., & Wood, B. J. (2013). Volcanism on Mars controlled by early oxidation of the upper mantle. *Nature*, *498*(7454), 342.

Usui, T., McSween, H. Y., & Clark, B. C. (2008). Petrogenesis of high-phosphorous Wishstone Class rocks in Gusev Crater, Mars. Journal of Geophysical Research: Planets, 113(E12).

Vilas, F., & Gaffey, M. J. (1989). Phyllosilicate absorption features in main-belt and outer-belt asteroid reflectance spectra. *Science*, *246*(4931), 790-792.

Wadhwa, M. (2008). Redox conditions on small bodies, the Moon and Mars. *Reviews in Mineralogy and Geochemistry*, *68*(1), 493-510.

Wall, K. T., Rowe, M. C., Ellis, B. S., Schmidt, M. E., & Eccles, J. D. (2014). Determining volcanic eruption styles on Earth and Mars from crystallinity measurements. *Nature communications*, *5*, 5090.

Wang, C., Jia, L., Tan, Y., and Anthony, E.J. (2010) The effect of water on the sulphation of limestone. Fuel, 89, 2628-2632.

Wang, Y. and Thomson, W.J. (1995) The effects of steam and carbon dioxide on calcite decomposition using dynamic X-ray diffraction. Chemical Engineering Science, 50, 1373-1382.

Weisberg, M. K., McCoy, T. J., & Krot, A. N. (2006). Systematics and evaluation of meteorite classification.

Whitaker, M. L., Nekvasil, H., Lindsley, D. H., & Difrancesco, N. J. (2006). The role of pressure in producing compositional diversity in intraplate basaltic magmas. Journal of Petrology, 48(2), 365-393.

Wilson, B. M. (2007). Igneous petrogenesis a global tectonic approach. Springer Science & Business Media.

Yamakawa, A. and Yin, Q.Z. (2014) Chromium isotopic systematics of the Sutter's Mill carbonaceous chondrite: implications for isotopic heterogeneities of the early Solar System. Meteoritics and Planetary Science, 49, 2118-2127.

Yoder, H. S., & Sahama, T. G. (1957). Olivine X-ray determinative curve. *Am. Mineralogist*, *42*, 475-491.

Ziegler, K. and Garvie, L.A.J. (2013) Bulk oxygen-isotope compositions of different lithologies in Sutter's Mill. 76th Annual Meteoritical Society Meeting, Abstract #5225.

Zolensky, M. and Ivanov, A. (2003) The Kaidun microbreccia meteorite: A harvest from the inner and outer asteroid belt. Chemie der Erde-Geochemistry, 63, 185-246.

Zolensky, M., Barrett, R., & Browning, L. (1993). Mineralogy and composition of matrix and chondrule rims in carbonaceous chondrites. *Geochimica et Cosmochimica Acta*, *57*(13), 3123-3148.

Zolensky, M., Herrin, J., Mikouchi, T., Ohsumi, K., Friedrich, J., Steele, A., Rumble, D., Fries, M., Sandford, S., Milam, S. and Hagiya, K. (2010) Mineralogy and petrography of the Almahata Sitta ureilite. Meteoritics and Planetary Science, 45, 1618-1637.

Zolensky, M., Mikouchi, T., Fries, M., Bodnar, R., Jenniskens, P., Yin, Q.Z., Hagiya, K., Ohsumi, K., Komatsu, M., Colbert, M., and Hanna, R. (2014) Mineralogy and petrography of C asteroid regolith: The Sutter's Mill CM meteorite. Meteoritics and Planetary Science, 49, 1997-2016.

APPENDIX A

AUTHOR PERMISSION FOR USE OF PUBLISHED MATERIAL

Laurence A. J. Garvie has granted permission for the use of co-authored materials in this dissertation.